Cavitation of Ultrasonically Excited Droplets

Hong Hao (Aaron) Ng

Supervisor: Prof. N. Nikiforakis

Cavendish Laboratory
University of Cambridge

This dissertation is submitted for the degree of
MPhil in Scientific Computing

Wolfson College

August 2022

Declaration

This dissertation is substantially my own work and conforms to the University of Cambridge's guidelines on plagiarism. Where reference has been made to other research this is acknowledged in the text and bibliography. This dissertation contains fewer than 15,000 words including tables, figure legends, and appendices, but excluding bibliography (TeXcount is used as the counting tool).

Hong Hao (Aaron) Ng
August 2022

Acknowledgements

I would like to express my greatest gratitude to my research supervisors, Professor Nikolaos Nikiforakis and Dr Stephen Millmore for their helpful guidance throughout the project. I also wish to thank Dr Philip Blakely for his valuable technical support on this project. Last but not least, I also thank the members of the Laboratory for Scientific Computing and my fellow MPhil cohort for their continuous encouragement.

Abstract

The current aircraft de-icing mechanisms are energy intensive and ultrasonic transducers are being explored as a new tool to prevent ice formation in the first place. Experiments conducted by Palacios et al. ([45], [46]) and Boeing have proven that ultrasonic vibrations can prevent ice formation on substrate at a fraction of energy needed in current electro-thermal de-icing system. Cavitation has emerged as the most feasible explanation for the phenomena observed in these experiments. Working alongside with Boeing, the Laboratory of Scientific Computing has been developing simulation models for the cavitation behaviour as theoretical approach is not feasible. This work develops a second order, hyperbolic diffuse interface Eulerian scheme for simulating the cavitation of a high speed liquid droplet impacting a wall with ultrasonic transducers installed underneath. The novelty of this work surrounds high speed droplet impact and the subsequent cavitation behaviour induced by ultrasonic excitation. The multiphysics of this work is the modelling of phase change behaviour due to pressure change in liquid. The cavitation behaviour can either be introduced as source terms accounting for mass transfer or encoded within the equation of state describing the material undergoing phase change.

Table of contents

List of figures xiii

List of tables xvii

Nomenclature xix

1 Introduction 1

2 Literature Review 5
- 2.1 Multi-material Diffuse Interface Model 5
- 2.2 Cavitation Model 6
  - 2.2.1 Two Phase Model 6
  - 2.2.2 Phase Change Model 8
- 2.3 Ultrasonic De-icing 9
- 2.4 Review Summary 10

3 Governing Equations 11
- 3.1 Fluid Equations of Motion 11
  - 3.1.1 Conservation Law for the Euler Equations 12
  - 3.1.2 1-D Ideal Euler 12
  - 3.1.3 2-D Ideal Euler 13
  - 3.1.4 2-D Cylindrical Euler 13
- 3.2 Equation of State 14
  - 3.2.1 Ideal Gas EOS 14
  - 3.2.2 Stiffened Gas EOS 15
  - 3.2.3 Speed of Sound 15
- 3.3 Multi-material Diffuse Interface Model 16
  - 3.3.1 Mixture Rules 16
  - 3.3.2 Seven Equations Model (Baer and Nunziato [3]) 17

3.3.3 Six Equations Model (Kapila et al. [27]) 18
3.3.4 Five Equations Model (Kapila et al. [27]) 19
3.4 Cavitation Model 20
3.4.1 Two Phase Model (Saurel et al. [56]) 20
3.4.2 Phase Change Model (Wilkinson et al. [63]) 23
3.5 Ultrasonic Excitation Boundary Condition 28

4 Numerical Method 31
4.1 Finite Volume Method 31
4.1.1 Conservative Update Formula 32
4.1.2 Godunov's Method 33
4.1.3 Approximate Riemann Solver 34
4.1.4 Primitive Variable MUSCL Hancock Scheme 36
4.1.5 Multidimensional Simulation 39
4.1.6 Operator Splitting 40
4.2 Two Phase Model (Saurel et al. [56]) 41
4.2.1 HLLC Riemann Solver 41
4.2.2 Godunov Update 42
4.2.3 Second Order Extension 43
4.3 Phase Change Model (Wilkinson et al. [63]) 44
4.3.1 HLLC Riemann solver 44
4.3.2 Godunov Update 44
4.3.3 Second Order Extension 44

5 Validation Tests 47
5.1 Single-Material Test 48
5.1.1 1-D Sod Test 48
5.1.2 2-D Cylindrical Explosion Test 52
5.2 Multi-material Test 54
5.2.1 Water-air Advection Test 54
5.2.2 Helium Bubble Collapse Test 55
5.3 Multiphase (Cavitation) Test 57
5.3.1 Two Rarefaction Induced Cavitation Test 57
5.3.2 Cavitation Model Comparison 59
5.3.3 Richtmyer-Meshkov Instability (RMI) Test 63
5.3.4 Liquid Droplet Impacting a Wall Test 66
5.3.5 Ultrasonic Excitation Induced Cavitation Test 71

6 Conclusion **77**

References **79**

Appendix A Pressure Relaxation Entropy Proof **85**

Appendix B Pseudocode for Phase Change Model **89**

List of figures

1.1 Experiment performed by Palacios et.al [45] shown that ultrasonic vibration (28 – 32 kHz) prevented ice formation on top of the actuator locations at a fraction of the power required with electro-thermal systems. 4

3.1 Plots showing the coexistence line separating the liquid and vapour phase of water [63] 24

4.1 Finite volume discretisation. The x-axis is discretised into cells x_i and the y-axis is split into steps t^n [38] 32

4.2 HLLC approximate Riemann solver. Solution in the star regions consist of two constant states separated from each other by the intermediate wave speed [60] 36

4.3 Data reconstruction. The piecewise linear extrapolation stage in MUSCL-Hancock for any primitive variable W [38]. 37

5.1 *Toro's test 1* at t = 0.25s 49

5.2 *Toro's test 2* at t = 0.15s 49

5.3 *Toro's test 3* at t = 0.012s 50

5.4 *Toro's test 4* at t = 0.035s 50

5.5 *Toro's test 5* at t = 0.035s 51

5.6 *Cylindrical explosion test* at t = 0.25s 52

5.7 *Cylindrical explosion test* 1-D slices from the midpoint in y-direction at t = 0.25s 53

5.8 *1D advection.* Plots showing advection of a volume fraction discontinuity in uniform pressure and velocity flow at time $t = 2.79ms$. 54

5.9 Initial configuration of the helium bubble collapse test. 55

5.10 *Helium bubble collapse.* The images show the mixture density plots on top and mock schlieren of the density at the bottom. The images are taken at time $t = 0.0s, 0.03s, 0.07s, 0.10s, 0.14s, 0.21s$. 56

5.11 *1D cavitation.* Plots showing expansion tube with cavitation pocket appearance at time $t = 1.85ms$. 57
5.12 *1D cavitation.* Plots showing expansion tube with cavitation pocket appearance using phase change model [left] and two phase model [right] at time $t = 0.5ms$. 60
5.13 *1D cavitation.* Extraction taken from pressure plot for phase change model 61
5.14 *1D cavitation.* Top: Plots showing density and pressure results taken from Saurel et al. [56] with 100 m/s initial velocity. Bottom: Plots showing density and pressure results taken from Wilkinson et al. [63] papers with 10 m/s initial velocity. 62
5.15 Initial configuration of the Richtmyer-Meshkov instability test. Both liquid and gas are moving to the left at $-200m/s$. 63
5.16 *Water-gas Richtmyer-Meshkov instability.* Mixture density plots are shown at time t=0ms, 1.7ms, 3.1ms, 4.8ms, 6.7ms, 8.6ms. 64
5.17 Density plot taken from Saurel et al. [56] paper at $t = 8.6ms$. 65
5.18 Initial configuration of the liquid droplet impacting a wall test. 66
5.19 *Liquid droplet impacting a wall.* The images show the pressure plots superimposed with density contours on the left and mock schlieren of the density on the right. The images are taken at time $t = 15.0\mu s, 16.3\mu s, 16.7\mu s$. . . . 67
5.20 *Liquid droplet impacting a wall.* The images show the pressure plots superimposed with density contours on the left and mock schlieren of the density on the right. The images are taken at time $t = 17.0\mu s, 17.5\mu s, 17.8\mu s$. . . . 68
5.21 *Liquid droplet impacting a wall.* Left: Pressure plot as $t = 14.4\mu s$ taken from Niu [43] paper. Right: Pressure plot as $t = 17.8\mu s$ produced using Saurel et al.'s model. 69
5.22 *Liquid droplet impacting a wall.* The images show the 2-D revolutions of pressure plots of the droplet with initial velocity $200m/s$ impacting a wall. The images are taken at time $t = 0.29\mu s, 0.31\mu s, 0.32\mu s, 0.34\mu s, 0.35\mu s, 0.37\mu s$. 70
5.23 *Liquid droplet impacting a wall with ultrasonic transducer underneath.* The images show the 2-D revolutions density plots. On the left, the plots are showing a droplet with initial velocity $200m/s$ impacting a wall while on the right, plots of the same droplet impacting a wall with an ultrasonic transducer installed underneath $(f = 5MHz, A = 5\mu m)$ are shown.The images are taken at time $t = 0.40\mu s, 0.55\mu s, 0.73\mu s$. 72

5.24 *Liquid droplet impacting a wall with ultrasonic transducer underneath.* The images show the density plots superimposed with liquid volume fraction contours. On the left, the plots are showing a droplet with initial velocity $200m/s$ impacting a wall. On the right, plots of the same droplet impacting a wall with an ultrasonic transducer installed underneath $(f = 6MHz, A = 5\mu m)$ are shown. The images are taken at time $t = 0.43\mu s, 0.70\mu s, 0.76\mu s, 0.90\mu s, 1.0\mu s, 1.19\mu s$. 73

5.25 *Liquid droplet impacting a wall with ultrasonic transducer underneath.* The images show the density plots superimposed with liquid volume fraction contours. On the left, first order accurate plots are showing the droplet with initial velocity $100m/s$ impacting a wall with an ultrasonic transducer installed underneath $(f = 6MHz, A = 5\mu m)$. On the right, second order accurate plots are shown. The images are taken at time $t = 0.81\mu s, 0.98\mu s, 1.06\mu s, 1.14\mu s, 1.32\mu s, 1.82\mu s$. 74

List of tables

3.1 Global variables of the fluid mixture 17

5.1 Initial data for Toro's test. 48
5.2 Table of reference states from IAPWS [61] and the resulting parameters for the equation of state for water 59

Nomenclature

Acronyms

AMR Adaptive Mesh Refinement

BC Boundary Condition

CFD Computational Fluid Dynamics

CFL Courant–Friedrichs–Lewy

CPU Central Processing Unit

DIM Diffuse Interface Method

EOS Equation of state

FV Finite Volume

GPU Graphics Processing Unit

HLLC Harten-Lax-van Leer-Contact

IVP Initial Value Problem

MUSCL Monotone Upstream-centred Schemes for Conservation Law

PDE Partial Differential Equation

SIM Sharp Interface Method

STP Standard Temperature & Pressure

THINC Tangent of Hyperbola for INterface Capturing

TVD Total Variation Diminishing

WENO Weighted Essentially Non-Oscillatory

Dimensionless Numbers

M	Mach Number, $\frac{u}{c}$
Re	Reynolds Number, $\frac{\rho u L}{\mu}$
We	Weber Number, $\frac{\rho u L}{\sigma}$

Letters

F	Vector of flux functions in x-direction
G	Vector of flux functions in y-direction
Q	Source terms
U	Vector of conservative variables
W	Vector of primitive variables
A	Amplitude
c	Speed of sound
C_{cfl}	CFL number
c_p	Heat capacity at constant pressure
c_v	Heat capacity at constant volume
D	Dimension of the system
E	Energy
e	Specific internal energy
e_0	Reference energy
f	Frequency
g	Gibbs free energy
I	Identity matrix
N	Number of cells
p	Pressure
p_∞	Reference pressure

r	Radius of a circle
S	Wave speed
s	Entropy
T	Temperature
t	time
U	Conservative variable
u	Velocity
v	Specific volume
W	Primitive variable
Y	Material mass fraction
Z	Acoustic impedance

Superscripts

*	Intermediate state
n	Referred quantity at time step n

Subscripts

i	Spatial discretisation correspond to a position in x
j	Spatial discretisation correspond to a position in y
k	Referred material sharing in a single cell
L	Referred material's position to the left of a Riemann problem
R	Referred material's position to the right of a Riemann problem

Symbols

α	Volume fraction
Δt	Physical time step
Δx	Space discretisation
γ	Gas constant

λ	Liquid vapour mass fraction
μ	Dynamic viscosity
ρ	Density
σ	Surface tension

Chapter 1

Introduction

Cavitation is the process of liquid undergoing phase change into vapour state when pressure within the liquid drops below the saturated pressure [20]. The understanding of cavitation behaviour is important in many engineering designs, as these phenomena can lead to long term wear of equipment from water hammering effect or due to the shock waves generated when cavities collapse. Experiment is definitely the most natural way of studying cavitation behaviour but has several shortcomings including limited information acquisition and poor operability. Cavitation exhibits a non-linear behaviour as the changes in output is not proportional to the input changes and a purely theoretical approach is not feasible. Hence, numerical simulation is needed for understanding cavitation. The modelling of cavitation can be difficult as it often involves complicated thermodynamic and hydrodynamic processes such as phase transition between liquid and vapour, dynamic creation of interfaces, vapour structure collapsing and its associated formation of shock wave [49].

The project has its roots in the far wider problem of aircraft icing. Aircraft icing is primarily formed from the supercooled water droplets that exist in the cloud at temperature below freezing point. When the droplets impact the plane body, their latent heat of fusion are dissipated to the body, which then lead to icing. Ice accretion on the plane wing can lead to disastrous events as it modifies the plane's aerodynamics, increases weight and vibration, and introduces ballistic concerns as ice being shed off. In order to tackle this issue, two approaches can be taken; de-icing (removal of ice already formed on plane wing) and anti-icing (prevent ice formation in the first place). In current days, one of the common de-icing approaches involves melting the ice using electro-thermal energy during in-flight condition. This solution is energy intensive and has an adverse impact on the fuel consumption. To put this in numbers, the amount of power needed to de-ice helicopter blades can be up to 3% of the total energy consumption [46]. Palacios et al. proposed a cheaper de-icing solution

by introducing ultrasonic excitation using transducers installed at the bottom of plane wing ([45], [46]). The working principle is to introduce transverse shear stress which is sufficiently higher than the adhesion strength of accreted freezer ice. Inspired by their work, ultrasonic transducers initially proposed for de-icing mechanism are being explored as a mean for anti-icing.

Boeing Research & Technology has been actively researching on other anti-icing technologies which require lesser energy. One of the proposed technologies is to apply super-hydrophobic surface finishing on plane wing to limit the area of thermal contact between water droplet and surface, reducing the heat loss from droplet to surface and maintaining its liquid state. However, this method requires nano-structuring and can lead to high maintenance cost due to the requirement for constant re-application. The second approach is to prevent the build up of ice through ultrasonic modulation of the surface using a transducer. Experimental results have shown that even under freezing condition, a layer of liquid water is maintained on the substrate. The interest on understanding the physics governing this anti-icing phenomena formed the motivation for the project with Boeing. Three possible mechanisms of preventing ice formation have been studied during the project, bouncing due to surface tension, break up due to vibration and cavitation induced lift-off. As the impact speeds are in the range of $100-200m/s$ [54], high Weber number of 5×10^5 indicates the effect of surface tension can be ignored. Secondly, although vibration induced break up is technically feasible as proven by Palacios et al. [46], this mechanism is invalid in explaining the Boeing's experiment as the timescale is much shorter in Boeing's case. Hence, cavitation induced lift-off emerged as the most feasible explanation for the phenomena, and this dissertation is an extension of the cavitation modelling performed with Boeing.

Cavitation modelling is a multiphysics problem as the system consists of an interface and, in certain approach, requires more than one material model for the mathematical or computational representation of its physics. The main challenge in performing oscillation free multi-material, multiphysics simulation is to achieve thermodynamic consistency at the interface between two materials [39]. Two main methods have been developed for this purpose:

- **Sharp Interface Method (SIM)** involves an additional technique to constantly identify the location of the interface and model each material with its own set of equations. The interface divides the computational domain into regions of individual materials.

- **Diffuse Interface method (DIM)** involves definition of mixture quantities for each cell and model the multiphysics problem using a single system of equations. The method creates a diffuse interface that covers several computational cells.

For SIM, the level set equation ([11], [40], [44], [58]) is commonly used to locate the material interface, and use this to split the computational domain into separate regions. At the interface, boundary conditions then need to be provided to ensure materials can interact correctly. The Ghost Fluid Method (GFM) developed by Fedkiw et al. [17] and its variations ([24], [32], [34], [62], [65]) are widely used for providing the dynamic boundary conditions due to their simplicity and versatility. For modelling phase change, an additional technique is required to determine the changes in material properties on top of the level set interface tracking, and this is difficult to be done consistently. Additionally, the fact that the problem to be modelled here will have a liquid-vapour interface existing over several cells add extra layers of complexity to this method.

The second method DIM is not a class of numerical technique but a formulation of the underlying system of equations which is thermodynamically consistent. In this method, an interface tracking method is not used, hence the exact location of an interface is never known. The key assumption of DIM is that more than one material can exist in a predefined volume at any time. The system of equations includes a volume fraction equation to track the mixture components over time. As the volume fraction equation is evolved over time, the interface between materials are subjected to numerical smearing. Among different DIM approaches, the class of models stemming from the original Baer and Nunziato model ([1], [3], [27], [41], [51]) stand out in terms of their capabilities in describing complex wave patterns and thermodynamics of cavitation. One of the important properties of these models is the consideration of compressibility for both liquid and vapour phases, which is essential to capture wave propagation phenomena and acoustic perturbations correctly during phase transition. In addition, as these models can retain the Gibbs free energy and temperature non-equilibrium effects, inclusion of source terms for modelling heat and mass transfer process allows the metastable states and evaporation fronts to be captured [49].

Generally, models accounting for the phase change (cavitation) physics can be divided into 3 categories:

- **Two phase model** ([49], [50], [56], [67], [68]) captures the liquid and vapour state as separate fluid using SIM or DIM. This model includes the effects of cavitation through addition of the mass transfer source terms. Furthermore, terms accounting for heat transfer and compaction are sometimes added.

- **Phase change model** ([4], [9], [14], [15], [16], [25], [63], [70]) is a single fluid model with the phase change behaviour encoded within the EOS. Homogeneous and barotropic flow assumptions are commonly made while defining the EOS. For problems involving more than a single material undergoing phase change, SIM or DIM can be used to capture the multi-material behaviour.

- **Bubble dynamics model** is developed based on the theory of classical bubble dynamics initially proposed by Lord Rayleigh [19] and the subsequent modifications by Plesset [52], Gillmore [21] and others. Generally, cavitation models adopting the theory of bubble dynamics can be single fluid or two fluid depending on the approach accounting the bubble radius [35].

In this dissertation, DIM multi-material approach integrated with two phase model and phase change model will be implemented. The objectives of this work are

- To compare different models describing cavitation (two phase model and phase change model).

- To implement second order accurate and quasi-conservative cavitation model for simulating cavitation-induced phase change in multidimensional problems.

- To incorporate boundary conditions which can replicate the ultrasonic excitation of a water droplet and demonstrate the subsequent cavitation effect.

An outline of the literature surrounding the field is provided in Chapter 2. Chapter 3 details the governing equations of the system, while Chapter 4 describes the numerical methods implemented. Chapter 5 collates the validation results for all the tests performed. Chapter 6 concludes the dissertation with some comments on future outlook.

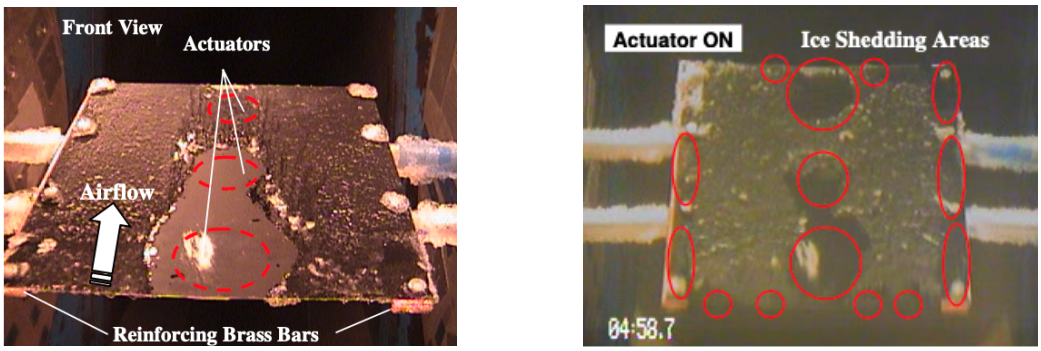

Fig. 1.1 Experiment performed by Palacios et.al [45] shown that ultrasonic vibration (28 – 32 kHz) prevented ice formation on top of the actuator locations at a fraction of the power required with electro-thermal systems.

Chapter 2

Literature Review

In this chapter, previous studies done which form the components of this work are reviewed. Multi-material models, cavitation models, droplet impact and ultrasonic anti-icing have been looked into. Each of these areas are under active research and only a representative sample of works is included.

2.1 Multi-material Diffuse Interface Model

For multi-material simulation, materials interaction which affect the individual material's quantities can be accounted as source terms in the evolution equations. In Baer and Nunziato [3] paper, the authors proposed a seven equations multiphase model for the purpose of deflagration-to-detonation modelling of granular explosives. The model is based on the continuum theory of mixtures, describing the compressibility of all phases and the compaction of granular materials. It facilitates the unequal phasic velocities and pressure, and source terms are included for drag and compaction behaviour to tackle velocity and pressure in-equilibrium. Although the model was developed for the application of reactive multiphase flow, the model's framework is applicable to other multiphase flow where non-equilibrium effects are significant, such as cavitation. However, the relaxation parameters in the source terms introduce new timescale to the system, which can lead to unstable simulations.

To tackle the stiff source terms in Baer and Nunziato model, Kapila et al. [27] proposed two reduction approaches: one building on velocity equilibrium assumption (six equations model) and the other on velocity and pressure equilibrium assumptions (five equations model). In the second approach, reductions are performed sequentially, starting with velocity followed by pressure. Pressure reduction alone will not work as this leads to equations of mixed hyperbolic-elliptic type which are not suitable for describing evolutionary problems ([7],

[12]). The equilibrium assumption can be made as different materials are being considered as true mixture at molecular scale. The six equations model evolves single momentum equation and both the energy equations, while the five equations model only evolves single momentum and energy equations. Furthermore, relaxation terms for equilibrating quantities are no longer needed with the new assumptions. For cavitation modelling using the six equations model, individual phasic pressures are evolved separately and the difference between them is used to calculate the degree of cavitation. On the other hand, the five equations model is used for multi-material simulation involving phase change by encoding the additional physics within the EOS governing the material or through the inclusion of additional source terms.

Building on the work of Kapila et al., Allaire et al. [1] introduced two algebraic closures (isobaric and isothermal) to the five equations model. From the studies, the isobaric approach is proven to be reliable in avoiding spurious pressure oscillation while computing interfaces between fluids. At every interface, a weighted average of the two sound speeds is used. Quasi-conservative numerical method is chosen to model the system of equations due to the non-conservative nature introduced by the volume fraction equation. Similar work has been done by Murrone et al. 2005 [41] to reduce the Baer and Nunziato system of equations to five equations model.

In summary, the five and six equations models proposed by Kapila et al. and Allaire et al. are chosen as the base model for modelling multi-material and multiphase. The main motivation for this selection is because while retaining the strength of Baer and Nunziato model in multi-material description, the models are simplified hence interfacial quantities and relaxation terms which could complicate the numerical method are avoided.

2.2 Cavitation Model

In this section, two main approaches for modelling cavitation (two phase model and phase change model) are reviewed.

2.2.1 Two Phase Model

The two phase model assumes individual cells are uniform and model each material with a separate set of equations. The exchange of mass, momentum and energy are treated explicitly as source terms in this model. However, quantities defining the exchange rate are difficult to obtain either experimentally or otherwise. Hence, many studies have been done to avoid

evolving the source terms by adopting relaxed equilibrium assumptions.

The first two phase model reviewed is the seven equations model proposed by Zein et al. [67] which includes the mass and heat transfer source terms to model transition and evaporation flow. In details, mass transfer is being modelled in terms of Gibbs free energy difference while heat transfer is being modelled in terms of temperature difference. The model is solved using Strang splitting and the source terms are successively integrated by the order of velocity relaxation, pressure relaxation, temperature relaxation and Gibbs free energy relaxation. This model is capable of dealing with cavitation, but requires complicated numerical method due to the source terms.

Saurel et al. [56] introduced a six equations hyperbolic model which adopts a pressure relaxation approach to maintain a positive volume fraction in the presence of shocks or strong expansion waves. Technically, this procedure is trying to converge the six equations model to five equations. Additionally, to tackle the non-conservative nature and correct the thermodynamic states presented by these equations, an additional equation accounting for the total mixture energy is introduced. The resulting model is capable of fulfilling the energy conservation on both sides of interfaces and guarantees correct shock transmission among them. Pelanti and Shyue [49] proposed replacing the two phasic internal energy equations in Saurel et al.'s model with two phasic total energy equations. This approach simplifies the design of the numerical scheme, as the extra equation for total energy is no longer needed to maintain the conservation of mixture energy.

Zhang 2020 [68] proposed a five equations model with heat and mass transfer source terms modelling phase change. The treatment of source terms are simplified into algebraic approach using relaxed equilibrium assumptions to avoid any expensive Newton iteration procedure. Furthermore, the author recommended replacing the Wood sound speed estimate with a monotonic mixture sound speed. This resolves the issue of non-monotonic behaviour of sound speed, making the non-conservative nature of five equations model less worrying.

In summary, the two phase model proposed by Saurel et al. stand out as the top choice for this dissertation, given the model was successfully implemented in the Boeing project. The other models discussed are essentially building on Saurel et al.'s model and should be considered for future work.

2.2.2 Phase Change Model

The phase change model can also be treated as a single fluid model, given the method treats the liquid and vapour mixture as a single fluid. In this method, a single set of PDEs is sufficient to model cavitation. During implementation, the phase change model can be integrated into the multi-material models discussed earlier for modelling multi-material with cavitation occurring. The main challenge of this model is to define an appropriate EOS for the liquid-vapour mixture to close the system. In defining the EOS, the mixture is usually assumed to be homogeneous and barotropic [57]. A fluid flow can be defined as barotropic when the fluid is homogeneous and two of the thermodynamic variables are constant, i.e. isentropic and isothermal conditions can lead to barotropic flow [28].

A couple of phase change models based on pressure cut-off were proposed by ([9], [70]). The cut-off model is technically a pure phase model, which simply set the pressure to a predefined cut-off pressure (normally the saturated pressure) when the local pressure drops below this [47]. In the cut-off region (where cavitation is occurring), the material is being considered as vapour and no phase change is considered. This method is easy to implement, but there are obvious physical violations of conservation law due to pressure cut-off [31]. Schmidt et al. [57] proposed a one fluid compressible cavitation model for the purpose of modelling high velocity and pressure flow in a nozzle. The mixture of liquid and vapour is assumed to be homogeneous and barotropic in this model. However, the model is only limited to small-size cavitation due to the restriction in sound speed calculation. An isentropic cavitation model based on Schmidt's model was proposed by Liu and this has been adopted by recent work such as Jin et al. [25] in simulating cavitation.

Barberon and Helluy [4] introduced a new method for simulating cavitation which involves updating the volume, mass and energy fractions after Godunov update with values obtained by a maximisation of the mixture entropy. The second law of thermodynamics is obeyed in this method. Faccanoni et al. [15] proposed a methodology to approximate the equilibrium EOS (thermodynamic equilibrium) when both phases are governed by a stiffened gas EOS and do not exist anywhere close to the critical point. After a Godunov update, the mass fraction, pressure and temperature are updated using the approximated equilibrium state values. In 2010, Faccanoni et al. [14] proposed an extension of this method to use a tabulated thermodynamics law which comes in handy for problems without an explicit expression of the equilibrium EOS.

Inspired by the work of Barberon and Helluy [4] and Faccanoni et al. [15], Wilkinson et al. [63] proposed a new approach based on the assumption of thermal equilibrium. The author extended the work to model multi-material using the Allaire et al.'s five equations model. Given the author has successfully adopted Adaptive Mesh Refinement (AMR), this model will be implemented in this dissertation with the plan of applying AMR in the future.

2.3 Ultrasonic De-icing

This section records the review done on previous numerical simulations and experiments that are relevant to the main simulation problem of this dissertation - cavitation of ultrasonically excited droplets.

Cimpeanu and Papageorgiou [8] performed simulations using the volume-of-fluid method to study the droplet impact onto solid surfaces in an aerodynamic context. As the primary target flight regimes of take-off and landing have relatively low velocities compared to flights cruising at higher altitudes, the in-compressible fluid flow model was used to describe the problem of interest. Zhang et al. [68] studied the dynamic behaviours and anti-icing characteristics of low speed droplets impacting an ultrasonically vibrating surface experimentally. Both the capillary wave and cavitation hypothesis made to explain the behaviour of droplet impinging an ultrasonically vibrating surface were validated through a series of experiments at different droplet speeds and vibration amplitudes. The experiment was repeated using supercooled water droplets, and it was found that the vibration prevented ice formation successfully.

2.4 Review Summary

Numerical simulations and experimental studies on de-icing mechanism by introducing shear stresses at the contact point between substrate and ice layer exist ([45], [46], [66]). However, anti-icing mechanism using ultrasonic transducers requires more thorough studies. In previous simulations performed with Boeing, the numerical method implemented lacks conservativeness and order of accuracy. The novelty of this work is to implement a quasi-conservative, second order accurate diffuse interface system modelling high speed liquid droplet impacting an ultrasonic excited surface for better understanding the subsequent cavitation behaviour. Furthermore, the implementation of a second order phase change model for simulating cavitation is a new addition to the Boeing project.

Chapter 3

Governing Equations

In this chapter the governing equations for the dynamics of a compressible material, along with the closure conditions in the form of Equations Of State (EOS) are discussed. Building on the basis of Euler equations, the multi-material models developed for systems with more than one material using diffuse interface methods are described in details. This chapter also encompasses the discussion on two different approaches for modelling cavitation (two phase model and phase change model). Furthermore, the equations introduced for simulating the effects of ultrasonic excitation are included in this chapter.

3.1 Fluid Equations of Motion

The fundamental equations for describing fluid dynamics are the Navier-Stokes equations. These equations factor in the effects of fluid viscosity and the resulting flux functions are dependent on the gradients of the state variables, leading to a non-hyperbolic system [30]. The next step of selecting the most appropriate system of equations can be done using the Reynolds number and Weber number with the characteristic linear dimension, L, being the droplet radius

$$Re = \frac{\rho u L}{\mu}, We = \frac{\rho u L}{\sigma}. \tag{3.1}$$

In this dissertation, liquid droplets travelling between $u = 100 - 200 m/s$ in the air are the main area of interest. Assuming a typical droplet size of $r = 100 \mu m$ with density of $1000 kg/m^3$ and viscosity $\mu = 0.001 Pas$, the corresponding Reynolds number is in the scale of 1×10^5. Hence, fluid viscosity can be assumed as negligible in all the test cases. Given this flow range and the corresponding Mach number > 0.3, fluid's compressibility needs to be considered for accurate modelling [2]. In addition to this physical requirement, the in-compressible formulation will suppress the sound waves effectively and damps out the

high frequency effects which is an important effect to be modelled in this project.

The relative importance of surface tension to the flow range being simulated in this dissertation can be checked using the Weber number. With the surface tension of water at $\sigma = 0.0729\text{kg/s}^2$, Weber number of $\sim 5 \times 10^5$ indicates that the surface tension will not have a dominant role in the material's evolution. In the absence of stress tensor and external force, the Navier-Stokes equation can be simplified to the Euler equations, which will form the basic equations describing the fluid dynamics in this dissertation.

3.1.1 Conservation Law for the Euler Equations

The Euler equations are a system of non-linear hyperbolic conservation laws governing the dynamics of a compressible material. Applying the fundamental laws of conservation of mass, Newton's Second Law and the conservation of energy, the Euler equations can be derived in the conserved variable form.

$$\frac{\partial \rho}{\partial t} + \nabla \cdot (\rho \mathbf{u}) = 0 \tag{3.2a}$$

$$\frac{\partial \rho \mathbf{u}}{\partial t} + \nabla \cdot (\rho \mathbf{u} \otimes \mathbf{u} + \mathbf{I} p) = 0 \tag{3.2b}$$

$$\frac{\partial \rho E}{\partial t} + \nabla \cdot [(\rho E + p)\mathbf{u}] = 0 \tag{3.2c}$$

Here ρ is the density, $\mathbf{u} = (u_x, u_y, u_z)^T$ the flow velocity, $E = e + \frac{1}{2}\mathbf{u} \cdot \mathbf{u}$ the total energy, e the specific internal energy and p the hydrodynamic pressure.

3.1.2 1-D Ideal Euler

Given the basis of numerical method used to solve the Euler system only considers equations, derivatives and Riemann problem in 1-D [38], the evolution equations need to be written in the following form

$$\frac{\partial \mathbf{U}}{\partial t} + \frac{\partial \mathbf{F}(\mathbf{U})}{\partial x} + \frac{\partial \mathbf{G}(\mathbf{U})}{\partial y} = 0. \tag{3.3}$$

Here $\mathbf{U}$ is the conserved variable, $\mathbf{F}(\mathbf{U})$ and $\mathbf{G}(\mathbf{U})$ are the flux functions in x-, y-directions respectively. The standard conservation form in Equations (3.2a) - (3.2c) can be written in 1-D as follows

$$\frac{\partial}{\partial t}\begin{pmatrix} \rho \\ \rho u_x \\ \rho E \end{pmatrix} + \frac{\partial}{\partial x}\begin{pmatrix} \rho u_x \\ \rho u_x^2 + p \\ (\rho E + p) u_x \end{pmatrix} = 0. \tag{3.4}$$

The fact that solving the Jacobian matrix gives three real, independent eigenvalues means that the system of Euler equations comprising three waves is hyperbolic (provided $c^2 = \left.\frac{\partial p}{\partial \rho}\right|_s > 0$). Additionally, the eigenvalues also represents the wave speeds of the 1-D system.

$$S_1 = u_x - c, \quad S_2 = u_x, \quad S_3 = u_x + c \tag{3.5}$$

3.1.3 2-D Ideal Euler

When considering a 2-D Euler system, evolution equations for both velocity components u_x and u_y are needed as velocity and momentum are vector quantities. As the pressure term only acts in the normal direction, it is only present in the x-component of ρu_x and y-component of ρu_y. The conservative form of Equations (3.2a) - (3.2c) can be written as follows

$$\frac{\partial}{\partial t}\begin{pmatrix} \rho \\ \rho u_x \\ \rho u_y \\ \rho E \end{pmatrix} + \frac{\partial}{\partial x}\begin{pmatrix} \rho u_x \\ \rho u_x^2 + p \\ \rho u_x u_y \\ (\rho E + p)u_x \end{pmatrix} + \frac{\partial}{\partial y}\begin{pmatrix} \rho u_y \\ \rho u_x u_y \\ \rho u_y^2 + p \\ (\rho E + p)u_y \end{pmatrix} = 0. \tag{3.6}$$

Here the total energy, E is a combination of internal energy and kinetic energy (KE). The KE which contains a contribution from both x- and y- velocity can be computed from

$$\mathrm{KE} = \frac{1}{2}\mathbf{u}\cdot\mathbf{u} = \frac{1}{2}(u_x^2 + u_y^2). \tag{3.7}$$

In 2-D, solving the primitive variable form gives four real but not distinct eigenvalues. This implies that the system is hyperbolic, but not strictly hyperbolic and the waves are not distinct to one another. However, the Jacobian matrix term is still diagonalisable, validating the hyperbolicity of the system [38].

3.1.4 2-D Cylindrical Euler

Up to this point, all the equations being described are in Cartesian coordinates. Cylindrical coordinates are sometimes more suitable to describe certain test cases. It is worth mentioning that conservation law is invariant under coordinate transformation [38].

For problems with cylindrical symmetry, the Euler equations system can be described as

$$\frac{\partial}{\partial t}\begin{pmatrix}\rho\\ \rho u_r\\ \rho u_z\\ \rho E\end{pmatrix}+\frac{\partial}{\partial r}\begin{pmatrix}\rho u_r\\ \rho u_r^2+p\\ \rho u_r u_z\\ (\rho E+p)u_r\end{pmatrix}+\frac{\partial}{\partial z}\begin{pmatrix}\rho u_z\\ \rho u_r u_z\\ \rho u_z^2+p\\ (\rho E+p)u_z\end{pmatrix}=-\begin{pmatrix}\frac{\rho u_r}{r}\\ \frac{\rho u_r^2}{r}\\ \frac{\rho u_r u_z}{r}\\ \frac{(\rho E+p)u_r}{r}\end{pmatrix}. \quad (3.8)$$

Here r represents the radial direction while z represents the axial direction. The main advantage to this system of equations is the numerical method implemented to the Cartesian coordinates are applicable here too. The coordinate effects will be applied through the source terms.

3.2 Equation of State

Given the Euler equations apply to a wide range of materials ranging from air to water, material specific behaviours need to be accounted for in the equations. The EOS plays an important role in fluid simulation as it is a continuum description of the materials' thermodynamic properties [38]. In multi-material, multiphase modelling, each fluid is compressible and requires the knowledge of an appropriate EOS depending on the material being accounted for.

3.2.1 Ideal Gas EOS

The ideal gas EOS is built on the assumption of gas comprises widely spaced, non-interacting point particles. The large distance between individual particles is due to the weaker intermolecular forces as compared to the particles' KE. Using the first law of thermodynamics and ideal gas law, the ideal gas EOS can be derived

$$\rho e(\rho,p)=\frac{p}{\gamma-1},\gamma=\frac{C_p}{C_v}. \quad (3.9)$$

This description is an incomplete EOS as not all the thermodynamic quantities (entropy, temperature) are specified. If necessary, thermodynamic potentials such as Helmholtz free energy and Gibbs free energy can be used to complete the EOS. As the ideal EOS is applicable to a wide range of gas and operating condition, it will be used to close any system of equations modelling gas in this dissertation.

3.2.2 Stiffened Gas EOS

In this dissertation, the stiffened gas EOS proposed by Menikoff and Plohr [36] is used to close a system of equations modelling water. This EOS was developed based on the recommendation of Harlow and Amsdem [22] on linearisation of the Mie-Grüneisen EOS when variations in density are small. The stiffened gas EOS emerged as the more suitable selection as compared to Van Der Waals EOS due to the limitation (negative sound speed) of the later EOS in modelling the mixture within the saturation dome [42]. The equation can be written in the following form which approximates the EOS near a reference state

$$\rho e(\rho, p) = \rho e_R(\rho) + \xi \left(p - p_R(\rho)\right), \tag{3.10}$$

where $p_R = -\gamma p_\infty$, $e_R = e_0$ and $\xi = \frac{1}{\gamma - 1}$. The reference energy e_R accounts for the contribution from the heat of formation of a material and is often irrelevant hence assumed to be negligible in this dissertation unless specified. The reference pressure p_∞ can be considered to represent the attraction between water molecules. Beyond ideal gas, most of the EOS parameters can be obtained from empirical fits to the measured behaviour given these parameters do not have a clear physical origin. In this dissertation, when stiffened gas EOS is used, parameters including γ, p_∞ and e_0 are taken from papers where the test cases are extracted from.

It is worth noting that the stiffened gas EOS reduces to a polytropic gas when $p_R = 0$. In the scenario of having a large p_R, the stiffened gas EOS models materials with a sound speed which is insensitive to changes in pressure (e.g. water) [36].

3.2.3 Speed of Sound

The speed of sound is generally defined as the derivative of pressure with respect to density at constant entropy

$$c = \sqrt{\left.\frac{\partial p}{\partial \rho}\right|_s}. \tag{3.11}$$

This forms the ideal case when the EOS describing the material is written in the form of $p = p(\rho, s)$. However, in most cases, entropy is not a natural quantity to use for describing materials. Instead, EOS in the form of $e = e(p, \rho) = e(p(\rho, s), \rho)$ is commonly used as this provides a relationship in terms of pressure and density. The derivative of this equation is presented as follows

$$\left.\frac{\partial e}{\partial \rho}\right|_s = \left.\frac{\partial e}{\partial p}\right|_\rho \left.\frac{\partial p}{\partial \rho}\right|_s + \left.\frac{\partial e}{\partial \rho}\right|_p. \tag{3.12}$$

Using the second law of thermodynamics, $T\ \mathrm{d}s = \mathrm{d}e + p\ \mathrm{d}v$ and the relationship $\mathrm{d}v = -\mathrm{d}\rho/\rho^2$, the first term on the left can be rewritten as $\left.\frac{\partial e}{\partial \rho}\right|_s = \frac{p}{\rho^2}$. The derivative above can be rearranged to fit into the general definition of sound speed to give

$$c^2 = \left.\frac{\partial p}{\partial \rho}\right|_s = \frac{p}{\rho^2 \frac{\partial e}{\partial p}|_\rho} - \frac{\frac{\partial e}{\partial \rho}|_p}{\frac{\partial e}{\partial p}|_\rho} = v^2 \frac{\frac{\partial e}{\partial v}|_p + p}{\frac{\partial e}{\partial p}|_v}. \tag{3.13}$$

The sound speed for systems described by stiffened gas EOS (3.10) takes the following form

$$c^2 = \frac{\gamma(p + p_\infty)}{\rho}. \tag{3.14}$$

3.3 Multi-material Diffuse Interface Model

This section describes the Baer and Nunziato [3] class of Diffuse Interface Methods (DIM) for modelling multi-material systems. In any of these methods, the volume fraction evolution equation is not conservative hence the system of equations.

3.3.1 Mixture Rules

Before discussing the models in details, an important convention for diffuse interface modelling needs to be clarified. Any quantities with an index k are per-occupied-region within a volume while any quantities without an index are per-entire-volume quantities. In this dissertation, index 1 represents material 1 while index 2 represents material 2.

In multi-material DIM, volume fraction (α_k) is defined as the volume of a constituent divided by the total volume, and they range between 0 and 1. For a defined volume containing a mixture of two materials,

$$\alpha_1 + \alpha_2 = 1. \tag{3.15}$$

Another important description of how materials are distributed within a volume is the mass fraction $Y_k = \frac{\alpha_k \rho_k}{\rho}$,

$$Y_1 + Y_2 = 1. \tag{3.16}$$

Using these quantities, mixture rules can be derived either based on the governing physics or sometimes from mathematically valid reasoning. Table 3.1 contains a list of mixture rules used in this dissertation.

Table 3.1 Global variables of the fluid mixture

Variable	Mixture rule
Density	$\alpha_1\rho_1 + \alpha_2\rho_2 = \rho$
Momentum	$\alpha_1(\rho u)_1 + \alpha_2(\rho u)_2 = \rho u$
Pressure	$\alpha_1 P_1 + \alpha_2 P_2 = P$
Internal energy	$\alpha_1\rho_1 e_1 + \alpha_2\rho_2 e_2 = \rho e$
Energy	$\alpha_1\rho_1 E_1 + \alpha_2\rho_2 E_2 = \rho E$
Specific enthalpy	$\alpha_1\rho_1 h_1 + \alpha_2\rho_2 h_2 = \rho h$

3.3.2 Seven Equations Model (Baer and Nunziato [3])

This model is built on the basis of evolving the three conserved variables $\rho_k, (\rho u)_k, \rho_k E_k$ for individual material and a volume fraction α_k equation which accounts for the mixture theory.

$$\frac{\partial \alpha_1}{\partial t} + u_1 \frac{\partial \alpha_1}{\partial x} = \mu\,(p_1 - p_2) \tag{3.17a}$$

$$\frac{\partial \alpha_1\rho_1}{\partial t} + \frac{\partial \alpha_1\rho_1 u_1}{\partial x} = 0 \tag{3.17b}$$

$$\frac{\partial \alpha_2\rho_2}{\partial t} + \frac{\partial \alpha_2\rho_2 u_2}{\partial x} = 0 \tag{3.17c}$$

$$\frac{\partial \alpha_1\rho_1 u_1}{\partial t} + \frac{\partial \alpha_1\left(\rho_1 u_1^2 + p_1\right)}{\partial x} = p_I' \frac{\partial \alpha_1}{\partial x} + \lambda\,(u_2 - u_1) \tag{3.17d}$$

$$\frac{\partial \alpha_2\rho_2 u_2}{\partial t} + \frac{\partial \alpha_2\left(\rho_2 u_2^2 + p_2\right)}{\partial x} = p_I' \frac{\partial \alpha_2}{\partial x} - \lambda\,(u_2 - u_1) \tag{3.17e}$$

$$\frac{\partial \alpha_1\rho_1 E_1}{\partial t} + \frac{\partial \alpha_1\left(\rho_1 E_1 + p_1\right)u_1}{\partial x} = p_I' u_I' \frac{\partial \alpha_1}{\partial x} - \mu p_I\,(p_1 - p_2) + \lambda u_I\,(u_2 - u_1) \tag{3.17f}$$

$$\frac{\partial \alpha_2\rho_2 E_2}{\partial t} + \frac{\partial \alpha_2\left(\rho_2 E_2 + p_2\right)u_2}{\partial x} = p_I' u_I' \frac{\partial \alpha_2}{\partial x} + \mu p_I\,(p_1 - p_2) - \lambda u_I\,(u_2 - u_1) \tag{3.17g}$$

The terms on the left side of the equations are the fluid equations described in Section 3.1 plus volume fraction. On the right side, the source terms introduced comprise the following quantities

- $p_I = \frac{Z_2 p_1 + Z_1 p_2}{Z_1 + Z_2}$ and $u_I = \frac{Z_1 u_1 + Z_2 u_2}{Z_1 + Z_2}$: Interfacial average quantities related to relaxation where $Z_k = \rho_k c_k$ represents acoustic impedance.
- p_I' and u_I': Interfacial average quantities related to drag effect.
- $\mu = \frac{2}{\Delta x (Z_1 + Z_2)}$ and $\lambda = \mu Z_1 Z_2$: Relaxation terms controlling the speed at which two materials in the same volume having different pressure or velocity equilibrate.

3.3.3 Six Equations Model (Kapila et al. [27])

The seven equations model described in the previous section can be simplified by applying some reasonable physical assumptions. For most diffuse interface models, the assumption of a true mixture at molecular scale is valid. Under this condition, velocity equilibrium is achieved at a rate faster than the hyperbolic time scales and instantaneous relaxation of velocity can be assumed.

The relaxation terms μ and λ are inversely related to the relaxation time scales. When the two materials have zero relevance to one another, $\mu = 0$ and $\lambda = 0$ implies there is no relaxation occurring. The assumption of instantaneous relaxation of velocity requires $\lambda \to \infty$ and the system is only true if $u_2 - u_1 = 0$. Using the mixture rule for density $\rho = \alpha_1 \rho_1 + \alpha_2 \rho_2$, the momentum equations (3.17d), (3.17e) can be merged into a single equation as presented below.

$$\frac{\partial \alpha_1}{\partial t} + u \frac{\partial \alpha_1}{\partial x} = \mu \left(p_1 - p_2 \right) \tag{3.18a}$$

$$\frac{\partial \alpha_1 \rho_1}{\partial t} + \frac{\partial \alpha_1 \rho_1 u}{\partial x} = 0 \tag{3.18b}$$

$$\frac{\partial \alpha_2 \rho_2}{\partial t} + \frac{\partial \alpha_2 \rho_2 u}{\partial x} = 0 \tag{3.18c}$$

$$\frac{\partial \rho u}{\partial t} + \frac{\partial \left(\rho u^2 + \alpha_1 p_1 + \alpha_2 p_2 \right)}{\partial x} = 0 \tag{3.18d}$$

$$\frac{\partial \alpha_1 \rho_1 E_1}{\partial t} + \frac{\partial \alpha_1 \left(\rho_1 E_1 + p_1 \right) u}{\partial x} = p_I' u_I' \frac{\partial \alpha_1}{\partial x} - \mu p_I \left(p_1 - p_2 \right) \tag{3.18e}$$

$$\frac{\partial \alpha_2 \rho_2 E_2}{\partial t} + \frac{\partial \alpha_2 \left(\rho_2 E_2 + p_2 \right) u}{\partial x} = p_I' u_I' \frac{\partial \alpha_2}{\partial x} - \mu p_I \left(p_1 - p_2 \right) \tag{3.18f}$$

3.3.4 Five Equations Model (Kapila et al. [27])

The other diffuse interface approach to model multi-material assumes velocity and pressure equilibrium to completely eliminate the requirement for source terms. The six equations model described in the previous section can be further simplified by adding the two energy equations together. One of the key advantages of this approach is the similarity of this method to those used for single phase fluid dynamics and facilitates the use of Adaptive Mesh Refinement (AMR).

$$\frac{\partial \alpha_1}{\partial t} + u\frac{\partial \alpha_1}{\partial x} = 0 \tag{3.19a}$$

$$\frac{\partial \alpha_1 \rho_1}{\partial t} + \frac{\partial \alpha_1 \rho_1 u}{\partial x} = 0 \tag{3.19b}$$

$$\frac{\partial \alpha_2 \rho_2}{\partial t} + \frac{\partial \alpha_2 \rho_2 u}{\partial x} = 0 \tag{3.19c}$$

$$\frac{\partial \rho u}{\partial t} + \frac{\partial \left(\rho u^2 + p\right)}{\partial x} = 0 \tag{3.19d}$$

$$\frac{\partial \rho E}{\partial t} + \frac{\partial (\rho E + p) u}{\partial x} = 0 \tag{3.19e}$$

For mixture of materials with differing compressibility, compaction needs to be taken into consideration as the assumption of uniform movement no longer stand. The volume fraction should change according to pressure difference, not just advection with velocity [38].

$$\frac{\partial \alpha_1}{\partial t} + u\frac{\partial \alpha_1}{\partial x} = K\nabla \cdot \mathbf{u} \tag{3.20}$$

$$K = \frac{\alpha_1 \alpha_2 \left(\rho_2 c_2^2 - \rho_1 c_1^2\right)}{\alpha_1 \rho_1 c_1^2 + \alpha_2 \rho_2 c_2^2} \tag{3.21}$$

Isobaric Closure

Allaire et al. [1] proposed the five equations multi-material model without the compaction source term. The authors have proven that the model is hyperbolic and material interfaces can be simulated without any pressure oscillations with an isobaric closure. The derivation of isobaric closure is briefly discussed here.

By manipulating the derivative of the total energy with isobaric assumption ($p_1 = p_2 = p$), the mixture sound speed can be derived to be

$$\xi c^2 = Y_1 \xi_1 c_1^2 + Y_2 \xi_2 c_2^2, \tag{3.22}$$

where $\xi_k = \left.\frac{\partial \rho_k e_k}{\partial p}\right|_{\rho_k}$, $\xi = \alpha_1 \xi_1 + \alpha_2 \xi_2$ and mass fraction $Y_k = \alpha_k \rho_k / \rho$. For general EOS, the process of obtaining the primitive variable pressure from conserved variables requires solving some sort of non-linear algebraic equation by iteration. Such method can be costly hence explicit expression of the pressure is used if available. For mixtures of two fluids governed by stiffened gas EOS (3.10), the coefficient introduced previously becomes

$$\xi_k = \left(\frac{\partial \rho_k e_k}{\partial p_k}\right)_{\rho_k} = \frac{1}{\gamma_k - 1}. \tag{3.23}$$

Using the mixture rule for internal energy and stiffened gas EOS (3.10), the definition of ρe yields

$$\rho e = \sum_k \alpha_k \rho_k e_k = \sum_k \alpha_k \left(\frac{p + \gamma_k p_{\infty k}}{\gamma_k - 1}\right) = p \sum_k \frac{\alpha_k}{\gamma_k - 1} + \sum_k \alpha_k \frac{\gamma_k p_{\infty k}}{\gamma_k - 1}. \tag{3.24}$$

By introducing averaged mixture coefficients, explicit EOS for a mixture can be derived as below and pressure can be computed analytically.

$$\xi = \frac{1}{\gamma - 1} = \sum_k \frac{\alpha_k}{\gamma_k - 1} \tag{3.25}$$

$$\frac{p_\infty \gamma}{\gamma - 1} = \sum_k \alpha_k \frac{p_{\infty k} \gamma_k}{\gamma_k - 1} \tag{3.26}$$

$$p(\alpha, \rho e) = (\gamma - 1)\rho e - \gamma p_\infty \tag{3.27}$$

3.4 Cavitation Model

In this dissertation, cavitation models proposed by Saurel et al. [56] and Wilkinson et al. [63] are implemented, and the cavitation behaviour modelled by the two are compared.

3.4.1 Two Phase Model (Saurel et al. [56])

In the six equations model, materials' pressure or internal energy are evolved separately and the difference between them is used to determine the degree of cavitation [39]. However, the formation of negative pressure in the system can lead to computational failure in the sound speed computation. Saurel et al.'s hyperbolic model enables cavitation modelling by allowing the pressure to enter tension with the pressure relaxation approach. In addition, the non-conservative nature of the system due to volume fraction and internal energies are

known to get the shock wave incorrectly placed. Hence, an additional evolution equation for total mixture energy is introduced to correct the thermodynamic state predicted.

$$\frac{\partial \alpha_1}{\partial t} + u\frac{\partial \alpha_1}{\partial x} = \mu\left(p_1 - p_2\right) \tag{3.28a}$$

$$\frac{\partial \alpha_1 \rho_1}{\partial t} + \frac{\partial \alpha_1 \rho_1 u}{\partial x} = 0 \tag{3.28b}$$

$$\frac{\partial \alpha_2 \rho_2}{\partial t} + \frac{\partial \alpha_2 \rho_2 u}{\partial x} = 0 \tag{3.28c}$$

$$\frac{\partial \rho u}{\partial t} + \frac{\partial \rho u^2 + (\alpha_1 p_1 + \alpha_2 p_2)}{\partial x} = 0 \tag{3.28d}$$

$$\frac{\partial \alpha_1 \rho_1 e_1}{\partial t} + \frac{\partial \alpha_1 \rho_1 e_1 u}{\partial x} + \alpha_1 p_1 \frac{\partial u}{\partial x} = -p_I \mu\left(p_1 - p_2\right) \tag{3.28e}$$

$$\frac{\partial \alpha_2 \rho_2 e_2}{\partial t} + \frac{\partial \alpha_2 \rho_2 e_2 u}{\partial x} + \alpha_2 p_2 \frac{\partial u}{\partial x} = p_I \mu\left(p_1 - p_2\right) \tag{3.28f}$$

$$\frac{\partial \rho\left(Y_1 e_1 + Y_2 e_2 + \frac{1}{2}u^2\right)}{\partial t} + \frac{\partial u\left(\rho\left(Y_1 e_1 + Y_2 e_2 + \frac{1}{2}u^2\right) + (\alpha_1 p_1 + \alpha_2 p_2)\right)}{\partial x} = 0 \tag{3.28g}$$

Mixture Sound Speed

The Wood sound speed ($\frac{1}{\rho c_{\text{eq}}^2} = \frac{\alpha_1}{\rho_1 c_1^2} + \frac{\alpha_2}{\rho_2 c_2^2}$) [64] used in Kapila et al.'s model was proven to be non-monotonic with volume fraction. This can cause inaccuracies in the wave's transmission across interfaces. In this model, frozen sound speed is used which takes the following form

$$c_f^2 = Y_1 c_1^2 + Y_2 c_2^2. \tag{3.29}$$

Relaxation Step

The interface condition under non-uniform pressure flow is full-filled in this step. In other words, this procedure is trying to converge the six equations multi-material model to five equations while phase change is being modelled. Firstly, the source terms in equations (3.28a - 3.28f) are solved as follows.

$$\frac{\partial \alpha_1}{\partial t} = \mu\left(p_1 - p_2\right) \tag{3.30a}$$

$$\frac{\partial \alpha_1 \rho_1 e_1}{\partial t} = -p_I \mu\left(p_1 - p_2\right) \tag{3.30b}$$

$$\frac{\partial \alpha_2 \rho_2 e_2}{\partial t} = p_I \mu\left(p_1 - p_2\right) \tag{3.30c}$$

The important assumption to be made here is that cavitation happens on a timescale faster than fluid evolution, i.e. $\mu \to \infty$. Given the pressures are being evolved separately, uniform pressure cannot be assumed without any further treatment to the system.

Combining equations (3.30a - 3.30b) gives

$$e_1 \frac{\partial \alpha_1 \rho_1}{\partial t} + \alpha_1 \rho_1 \frac{\partial e_1}{\partial t} = -p_I \frac{\partial \alpha_1}{\partial t}. \tag{3.31}$$

As $\alpha_1 \rho_1$ has no source term, the relationship can be written as

$$\frac{\partial e_1}{\partial t} = \frac{p_I}{\alpha_1 \rho_1} \frac{\partial}{\partial t} \left(\frac{\alpha_1 \rho_1}{\rho_1} \right). \tag{3.32}$$

Using the product rule, the equation can be written as

$$\frac{\partial e_1}{\partial t} = \frac{p_I}{\alpha_1 \rho_1} \left[\frac{1}{\rho_1} \frac{\partial \alpha_1 \rho_1}{\partial t} + \alpha_1 \rho_1 \frac{\partial}{\partial t} \left(\frac{1}{\rho_1} \right) \right] = -p_I \frac{\partial v_1}{\partial t}, \tag{3.33}$$

with the specific volume $v_1 = 1/\rho_1$. Similarly, for material 2, the equation for specific internal energy can be obtained as

$$\frac{\partial e_2}{\partial t} + p_I \frac{\partial v_2}{\partial t} = 0. \tag{3.34}$$

By integrating the two relationships with respect to time, the following equation can be obtained,

$$e_k - e_k^0 + \hat{p}_{I,k} \left(v_k - v_k^0 \right) = 0, \quad \text{with } \hat{p}_{I,k} = \frac{1}{v_k - v_k^0} \int_0^{\Delta t} p_I \frac{\partial v_k}{\partial t} \, \mathrm{d}t. \tag{3.35}$$

Due to the complexity of obtaining the integrated variable $\hat{p}_{I,k}$, Saurel et al. recommended setting $\hat{p}_{I,k} = p$, the relaxed pressure which is compatible with the entropy inequality [55]. The derivation for proving the entropy condition is included in Appendix A. Hence, the equation becomes

$$e_k \left(p_k, v_k \right) - e_k^0 \left(p_k^0, v_k^0 \right) + p \left(v_k - v_k^0 \right) = 0, \tag{3.36}$$

which involves three unknowns v_1, v_2 and p. Using the stiffened gas EOS, the equation can be written into the following form

$$v_k(p) = v_k^0 \frac{p_k^0 + \gamma_k p_{\infty,k} + (\gamma_k - 1) p}{\gamma_k p_{\infty,k} + \gamma_k p}. \tag{3.37}$$

Given that all the EOS parameters v_i^0, p_i^0 and $(\alpha\rho)_i$ are constants, the volume fraction can be rewritten into

$$(\alpha\rho)_k v_k(p) = \frac{a_k + b_k p}{c_k + \gamma_k p}. \tag{3.38}$$

Using the saturation constraint $\alpha_1 + \alpha_2 = (\alpha\rho)_1 v_1 + (\alpha\rho)_2 v_2 = 1$, the volume fraction sum can then be written in quadratic form

$$\frac{a_1 + b_1 p}{c_1 + \gamma_1 p} + \frac{a_2 + b_2 p}{c_2 + \gamma_2 p} - 1 = 0, \tag{3.39}$$

which the relaxed pressure, p is the negative root of this quadratic equation. Once the relaxed pressure is computed, volume fraction can be reset using the equation (3.37).

Reinitialisation Step

Using the new volume fraction, mixture pressure can be computed based on the conserved total energy. As the equation is using an EOS which is valid in pure fluids and based on total energy equation which obeys conservation law, it guarantees conservation and correct wave dynamics on either side of the interface.

$$p_{\text{mix}} = \frac{E - \frac{1}{2}\rho v^2 - \sum_k \frac{\alpha_k \gamma_k p_{\infty,k}}{\gamma_k - 1}}{\sum_k \frac{\alpha_k}{\gamma_k - 1}} \tag{3.40}$$

Once the mixture pressure is determined, the phasic internal energies are reinitialised with the EOS before moving onto the next step.

$$e_k = e_k\left(p_{\text{mix}}, \frac{(\alpha\rho)_k}{\alpha_k}\right) \tag{3.41}$$

3.4.2 Phase Change Model (Wilkinson et al. [63])

The five equations multi-material model can be extended to include additional multiphysics, multiphase by encoding details within the EOS for each material. The resulting model can then be used to model phase transition phenomena such as cavitation without any alteration of the conventional numerical algorithms. In Wilkinson et al.'s model, thermal equilibrium is assumed while defining the EOS for a material undergoing phase change. Thermal equilibrium happens when two objects are said to be having the same temperature and there is no heat transfer between them. The interaction through heat transfer and compaction of vapour and liquid phase are encoded entirely within the EOS. Thus, it is possible to model

cavitation accurately without having to integrate the source term in the volume fraction equation.

Thermodynamic Framework

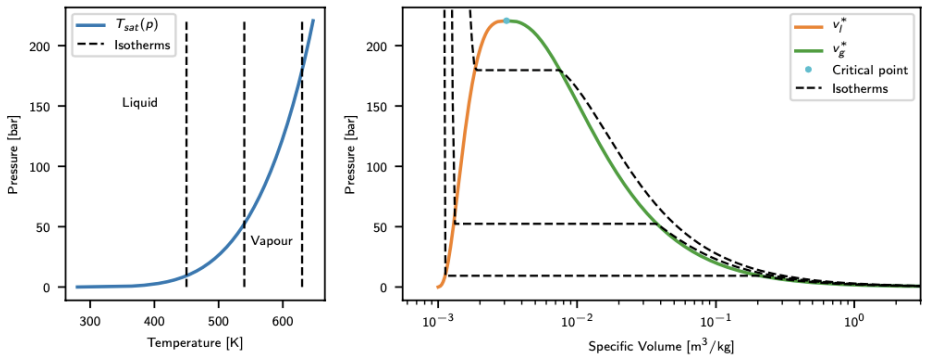

Fig. 3.1 Plots showing the coexistence line separating the liquid and vapour phase of water [63]

Phase transition of a material between liquid and gas lead to discontinuity in density as a function of temperature and pressure - a small change in temperature at boiling point can lead to drastic density changes. When the material reaches thermal equilibrium, the configuration having the least Gibbs free energy will manifest given it is energetically favourable. The coexistence line is the locus of states along which the two phases can coexist and have the same Gibbs free energies.

$$g_l\left(p, T_{\text{sat}}\left(p\right)\right) = g_g\left(p, T_{\text{sat}}\left(p\right)\right) \tag{3.42}$$

Given the volume is not constant across the critical line, the critical line is a 2-D area known as saturation dome within the p-v space. Within the saturation dome, a blend of liquid and vapour coexist in thermal equilibrium with one another. Along the left and right edges of the saturation dome, the specific volumes v_l^* and v_g^* can be computed from

$$\begin{aligned} v_l^*(p) &= v_l\left(p, T_{sat}(p)\right), \\ v_g^*(p) &= v_g\left(p, T_{sat}(p)\right). \end{aligned} \tag{3.43}$$

Within the saturation dome, the mass fraction can be defined as

$$\lambda(v,p) = \begin{cases} 1 \text{ if } v < v_l^*(p) \\ \dfrac{v - v_g^*(p)}{v_l^*(p) - v_g^*(p)} \text{ if } v_l^*(p) < v < v_g^*(p) \\ 0 \text{ if } v_g^*(p) < v. \end{cases} \tag{3.44}$$

Using the mass fraction, specific volume for the mixture can be calculated from

$$v = \lambda(v,p)v_l^* + (1-\lambda)v_g^*. \tag{3.45}$$

The EOS for a material undergoing phase transition can then be summarised as

$$e^{PT}(v,p) = \begin{cases} e_l(v,p) \text{ if } v < v_l^*(p) \\ \lambda e_l^*(p) + (1-\lambda)e_g^*(p) \text{ if } v_l^*(p) < v < v_g^*(p) \\ e_g(v,p) \text{ if } v_g^*(p) < v \end{cases} \tag{3.46}$$

where $e_l^*(p) = e_l\left(v_l^*(p), p\right)$ and $e_g^*(p) = e_g\left(v_g^*(p), p\right)$ are the specific internal energies for each phase.

The equation above adds little overhead to the computational power as for parts of the domain without cavitation, the equation simplifies to the underpinning model of stiffened gas EOS; for the domain where cavitation does occur, a non-linear relaxation with only one degree of freedom is needed [63].

One of the limitations here is to provide the correct behaviour near the critical point, where the discontinuity disappears. Hence, while pressure exceeds the pre-defined maximal pressure near the critical point, p_{max}, v_l^* and v_g^* are assumed to be independent of pressure to ensure energy is continuous over the whole p-v domain. At regions near the critical point, equation (3.43) is replaced with

$$\begin{aligned} v_l^* &= v_l\left(\hat{p}, T_{sat}(\hat{p})\right), \\ v_g^* &= v_g\left(\hat{p}, T_{sat}(\hat{p})\right), \\ \hat{p} &= \max\left(p_{\min}, \min\left(p, p_{\max}\right)\right). \end{aligned} \tag{3.47}$$

Equation of State

For this cavitation model, the stiffened gas EOS (3.10) with the reference energy term is used to account for the heat of formation of the two phases and thus the change in enthalpy associated with phase change. Furthermore, complete stiffened gas EOS is needed for this cavitation model and Gibbs free energy is used to specify the rest of the thermodynamic quantities. The stiffened gas EOS takes the following form

$$\rho e(\rho, p) = \rho e_R(\rho) + \xi \left(p - p_R(\rho)\right), \tag{3.48}$$

where $p_R = -\gamma p_\infty$, $e_R = e_0$ and $\xi = \frac{1}{\gamma - 1}$. Using the specific heat capacity at constant volume, the temperature can be defined as

$$T(v, p) = \frac{v\,(p + p_\infty)}{(\gamma - 1)c_v}. \tag{3.49}$$

By integrating the specific heat capacity, entropy can be defined as

$$s(p, T) = s_0 + c_v \ln\left(\frac{T^\gamma}{(p + p_\infty)^{\gamma - 1}}\right), \tag{3.50}$$

where s_0 is the integration constant and the Gibbs free energy can be calculated from

$$\begin{aligned} g(p, T) &= e + pv - Ts \\ &= e_0 + \gamma c_v T - T\left(s_0 + c_v \ln\left(\frac{T^\gamma}{(p + p_\infty)^{\gamma - 1}}\right)\right), \end{aligned} \tag{3.51}$$

where e_0 is another integration constant.

The approach of calculating $T_{\text{sat}}(p)$ by equating the Gibbs free energies requires a non-linear solver which is computational expensive. Hence, tabulation of the saturation temperature, $T_{\text{sat}}(p)$, is done using International Association for the Properties of Water and 265 Steam (IAPWS) data [61] and the required value is obtained via linear interpolation between two known data points (x_0, y_0) and (x_1, y_1).

$$y = y_0 + (x - x_0)\frac{y_1 - y_0}{x_1 - x_0} = \frac{y_0\,(x_1 - x) + y_1\,(x - x_0)}{x_1 - x_0} \tag{3.52}$$

While implementing this model, any algorithm requiring the EOS (variable conversion between primitive and conservative, sound speed calculation) should first determine whether

cavitation is occurring. For computing pressure, the energy at a density dependent threshold pressure corresponding to the edge of the saturation dome is evaluated. If there is cavitation, a bisection search algorithm is used to determine the corresponding pressure value which gives the input energy value. When there is no cavitation, the EOS governing the mixture reduces to the stiffened gas EOS describing either pure liquid or gas. The pseudocode for computing pressure and energy are included in Appendix B.

Material Sound Speed

When the material falls outside the saturation dome, the sound speed is defined by either the EOS for liquid or gas. Inside the saturation dome, both EOS need to be considered. The generic equation for the speed of sound is still applicable here with some new definitions.

$$c^2 = v^2 \frac{\left(\frac{\partial e}{\partial v}\right)_p + p}{\left(\frac{\partial e}{\partial p}\right)_v} \tag{3.53}$$

The derivative with respect to volume is straight forward as v_l^* and v_g^* are only dependent on pressure.

$$\left(\frac{\partial e}{\partial v}\right)_p = \frac{e_g^* - e_l^*}{v_g^* - v_l^*} \tag{3.54}$$

The derivative with respect to pressure is more complex and demonstrated as follows

$$\left(\frac{\partial e}{\partial p}\right)_v = \lambda \frac{\mathrm{d}e_l^*}{\mathrm{d}p} + (1-\lambda)\frac{\mathrm{d}e_g^*}{\mathrm{d}p} + \left(\frac{\partial \lambda}{\partial p}\right)_v \left(e_l^* - e_g^*\right), \tag{3.55}$$

$$\frac{\mathrm{d}e_l^*}{\mathrm{d}p} = \left(\frac{\partial e_l\left(v_l^*, p\right)}{\partial v}\right)_p \frac{\mathrm{d}v_l^*}{\mathrm{d}p} + \left(\frac{\partial e_l\left(v_l^*, p\right)}{\partial p}\right)_v, \tag{3.56a}$$

$$\left(\frac{\partial \lambda}{\partial p}\right)_v = \frac{1}{v_g^* - v_l^*}\left(\lambda \frac{\mathrm{d}v_l^*}{\mathrm{d}p} + (1-\lambda)\frac{\mathrm{d}v_g^*}{\mathrm{d}p}\right), \tag{3.56b}$$

$$\frac{\mathrm{d}v_l^*}{\mathrm{d}p} = \left(\frac{\partial v_l\left(p, T_{sat}(p)\right)}{\partial T}\right)_p \frac{\mathrm{d}T_{sat}(p)}{\mathrm{d}p} + \left(\frac{\partial v_l\left(p, T_{sat}(p)\right)}{\partial p}\right)_T. \tag{3.56c}$$

The required derivatives to solve the equations above can be derived from the stiffened gas EOS and presented as follows

$$\left(\frac{\partial v}{\partial p}\right)_T = -\frac{(\gamma-1)c_v T}{(p+p_\infty)^2}, \tag{3.57a}$$

$$\left(\frac{\partial v}{\partial T}\right)_p = \frac{(\gamma-1)c_v}{p+p_\infty}, \tag{3.57b}$$

$$\left(\frac{\partial e}{\partial p}\right)_v = \frac{v}{\gamma-1}, \tag{3.57c}$$

$$\left(\frac{\partial e}{\partial v}\right)_p = \frac{p+\gamma p_\infty}{\gamma-1}. \tag{3.57d}$$

It is worth noting that the sound speed is discontinuous at the boundary of the saturation dome. This is especially important near the liquid boundary given the change in sound speed is significant. The reason behind this dramatic change is that the pressure of water vapour can increase the compressibility of a mixture by large amount even in small quantities. In order to produce physical simulations, a minimum sound speed of 1.037m/s [63] is set to maintain the positivity of sound speed near discontinuity.

3.5 Ultrasonic Excitation Boundary Condition

For accurate simulation of the ultrasonic vibration effects, the behaviour of the transducer needs to be reproduced within the computational domain. Assuming the transducer's vibration is sufficiently small ($< 0.5\mu m$), the behaviour is not expected to be resolved using the numerical model. In fact, the vibration is being modelled as a time-varying velocity input into the domain above the location of the transducer [37].

The motion produced by the transducer is assumed to be following a periodic profile. Hence, these phenomena can be described as a solution to the wave equation,

$$\frac{\partial^2 l}{\partial t^2} = K^2\left(\frac{\partial^2 l}{\partial r^2} + \frac{1}{r}\frac{\partial l}{\partial r} + \frac{1}{r^2}\frac{\partial^2 l}{\partial \theta^2}\right), \tag{3.58}$$

where K is a fixed non-negative real coefficient and l is the displacement of the surface, with solution,

$$l(r,\theta,t) = A\sin\left(\frac{\omega a_{mn} t}{r_0}\right) J_m\left(\frac{a_{mn} r}{r_0}\right)(B*\cos(m\theta)+C*\sin(m\theta)). \tag{3.59}$$

Here, r_0 is the radius of the transducer, ω determines the vibration frequency, A is the oscillation's amplitude, B and C determine the importance of different angular components, m and n are the modal components of the oscillation. J_m is the mth order Bessel function of the first kind, a_{mn} is the nth zero of J_m.

In order to conduct the studies of anti-icing properties of this technology, the effects of ultrasonic vibrations can be quantified through a parameter study. To conduct this efficiently, cylindrically symmetric configuration is chosen, i.e. $m = 0$. For simplification purpose, the $n = 1$ mode is applied since this is most likely to have the largest influence on the system. The velocity profile obtained is as follows,

$$u = 2\pi\omega A\cos(2\pi\omega t)\left(\frac{1}{2}+\frac{1}{2}\cos(\frac{\pi r}{r_0})\right), \quad r < r_0. \tag{3.60}$$

Chapter 4

Numerical Method

In this chapter, the numerical approaches used to model the system of equations described in Chapter 3 are discussed. Riemann problem based hyperbolic solver is chosen to model the system on an Eulerian finite volume framework. A comprehensive explanation of the methods outlined below is presented by Toro [60] and reader is recommended to refer there for more details. The computer code used to implement the numerical methods is C++ programming language in an object-oriented format. The solver is developed using the framework of AMReX which is a software developed as part of the U.S. DOE Exascale Computing Project for massively parallel and block structured Adaptive Mesh Refinement (AMR) applications [69]. AMReX only provides the mesh management capabilities and coding of the solver from scratch was done as part of this dissertation.

4.1 Finite Volume Method

The finite volume method is chosen as it is conservative and capable of computing solutions containing discontinuities such as shock waves. With finite volume, the domain is being treated as volume and a discretised unit is represented by single volume with fixed width also known as cell. Data is being defined within a cell and function value is an integral average over the cell volume.

4.1.1 Conservative Update Formula

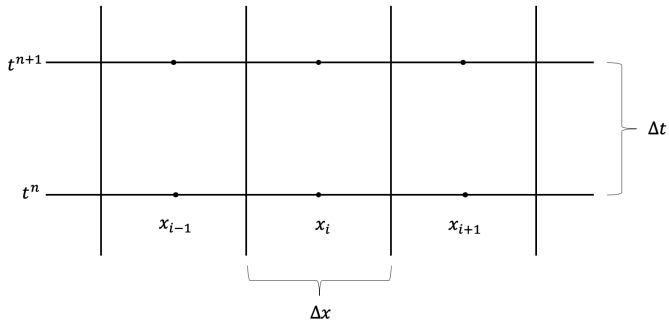

Fig. 4.1 Finite volume discretisation. The x-axis is discretised into cells x_i and the y-axis is split into steps t^n [38]

The conservation law states that the change in **U** over a time interval in a fixed domain can be computed from the amount of **U** that enters or leaves the domain in this interval.

$$\int_a^b \mathbf{U}(t_2,x) - \mathbf{U}(t_1,x)\,\mathrm{d}x = -\int_{t_1}^{t_2} \mathbf{F}(\mathbf{U}(t,b)) - \mathbf{F}(\mathbf{U}(t,a))\mathrm{d}t \tag{4.1}$$

Within a finite volume method, the quantity $\mathbf{U}_i^n$ is the volume integral average within a cell i at time n while the flux $\mathbf{F}_{i\pm1/2}^n$ is the material passing through cell boundaries and can be computed from the integral over a time interval.

$$\mathbf{U}_i^n = \frac{1}{\Delta x}\int_{x_{i-1/2}}^{x_{i+1/2}} \mathbf{U}(x,t^n)\,\mathrm{d}x \tag{4.2}$$

$$\mathbf{F}_{i\pm1/2}^n = \frac{1}{\Delta t}\int_{t^n}^{t^{n+1}} \mathbf{F}\left(\mathbf{U}\left(x_{i\pm1/2},t\right)\right)\mathrm{d}t \tag{4.3}$$

By rearranging Equation (4.1), the finite volume update formula can be written as below

$$\mathbf{U}_i^{n+1} = \mathbf{U}_i^n - \frac{\Delta t}{\Delta x}\left(\mathbf{F}_{i+1/2}^n - \mathbf{F}_{i-1/2}^n\right). \tag{4.4}$$

Space and Time Discretisation

Space discretisation length, Δx is governed by the choice of resolution and available computing resources. The time discretisation Δt is computed from the equation

$$\Delta t = \frac{C_{\mathrm{cfl}}\Delta x}{S_{\max}^n}, \tag{4.5}$$

where C_{cfl} is the CFL coefficient satisfying the condition

$$0 < C_{\text{cfl}} \leq 1.$$

The closer the coefficient is to 1, the more efficient the time marching scheme is as every time step brings certain numerical error which can lead to unphysical artificial diffusion over long timescale [60]. S^n_{max} is the largest wave speed present in the domain during time n. In hyperbolic PDEs, any change in variable in one location will travel out at finite wave speed [38]. Given the time step is constrained by the fastest wave, no wave is present in the solution of any Riemann problem travelling more than the distance of Δx at anytime and the capturing of all the material's motion is guaranteed. In this dissertation, the equation chosen for estimating S^n_{max} in single/multidimensional problems is presented as follows

$$S^n_{\text{max}} = \max_{i,j} \left\{ \left| \mathbf{u}^n_{i,j} \right| + c^n_{i,j} \right\}. \tag{4.6}$$

This method of computing the S^n_{max} can lead to an underestimation of the maximum wave speed as only values for particle velocities and sound speed are accounted for. Instabilities can be introduced when S^n_{max} are underestimated as excessively large time steps are used in the simulation. In this dissertation, $C_{\text{cfl}} < 1$ is used in all the simulations to account for the uncertainties in maximum wave speed. For multidimensional simulations, the C_{cfl} coefficient is further reduced and this will be explained in Section 4.1.5.

4.1.2 Godunov's Method

To compute the flux $\mathbf{F}^n_{i\pm 1/2}$ in Equation (4.4), two of the possible methods are using centred schemes or Riemann problem based schemes (Godunov's method). Godunov's method is widely used to solve hyperbolic partial differential equations with discontinuous solutions due to the ability to achieve high resolution at discontinuities and robustness of the scheme. Upwind scheme for prescribing Godunov flux use wave propagation information contained in the differential equations, which can be obtained by solving a local 1-D Riemann problem in the direction normal to cell interface [60]. Hence, the essential ingredients for adopting Godunov's method is the solution of a Riemann problem, whether it is an exact or approximated solution.

Riemann solvers can also be classified as complete or incomplete depending on whether all the characteristic fields present in the exact Riemann problem are included in the wave model. For solving system of equations governing multi-material, exact Riemann solvers

exist but it is recognised to be too computationally expensive. Approximate Riemann solver is used to model the system of equations described in Chapter 3 as it provides a good compromise between solution accuracy and computational cost when compared to centred schemes and exact Riemann solver.

The Riemann Problem

The Riemann problem is a type of Initial Value Problem (IVP) made up of a conservation equation and piece-wise constant initial data separated by a jump in discontinuity.

$$\frac{\partial \mathbf{U}}{\partial t} + \frac{\partial \mathbf{F}(\mathbf{U})}{\partial x} = 0, \quad \mathbf{U}(x,0) = \begin{cases} \mathbf{U}_L & x < x_0 \\ \mathbf{U}_R & x > x_0 \end{cases}$$

In this project, some test cases being considered can be treated as a global Riemann problem, but this is not always the case. The boundary between cells can be treated as a local Riemann problem by considering constant average values across the cell. There are many hyperbolic solvers developed on the basis of Riemann problem and reader is recommended to refer Toro's book [60] for more details. In this work, HLLC will be used as the numerical approach for solving the system of equations described in this dissertation.

4.1.3 Approximate Riemann Solver

The HLLC approximate Riemann solver is chosen as the solver is capable of dealing with arbitrary shocks, genuinely positive and consequently robust [56].

Background

Harten, Lax, and van Leer (HLL) [23] first proposed an approximate Riemann solver that will yield positive solution if used with an appropriate choice of wave speed bounds. This scheme assumes the solution is a wave configuration that consists of two waves separating three constant states. Wave speed estimates proposed by Davis and Einfeldt [10] enabled the approach to produce practical results of intercell fluxes. The HLL scheme, together with the new wave speed estimate, is known as the HLLE solver. The assumption of the two waves configuration in HLL and HLLE scheme can lead to inaccurate solutions as the solvers are too diffusive and unable to resolve contact discontinuities very well. Toro et al. presented HLLC ("C" stands for contact) to tackle the problem of intermediate wave by adopting a three waves model with two intermediate states in the Riemann problem solution. The third wave

is the contact discontinuity as the wave behaviour aligns with the assumption of intermediate left and right states having the same pressure and velocity [60].

HLL and HLLC Riemann Solver

Constructing a Riemann problem along the x-direction with piece-wise constant left and right initial states ($t = 0$) give

$$\mathbf{U}(x,0) = \begin{cases} \mathbf{U}_L, & \text{if } x < 0 \\ \mathbf{U}_R, & \text{if } x > 0 \end{cases} \tag{4.7}$$

Using the HLL approach, the approximated Riemann solution can be obtained as

$$\mathbf{U}_{HLL} = \begin{cases} \mathbf{U}_L, & \text{if } S_L > 0 \\ \mathbf{U}^*, & \text{if } S_L \leq 0 \leq S_R \\ \mathbf{U}_R, & \text{if } S_R < 0 \end{cases} \tag{4.8}$$

Here the S_L and S_R are the fastest wave speeds for the left and right states. The intermediate subsonic state U^* can be calculated using

$$\mathbf{U}^* = \frac{S_R\mathbf{U}_R - S_L\mathbf{U}_L - (\mathbf{F}_R - \mathbf{F}_L)}{S_R - S_L} \tag{4.9}$$

where $F_L = F(U_L)$ and $F_R = F(U_R)$. Note that for the intermediate flux $F_{HLL} \neq F(U_{HLL})$ and must be computed using

$$\mathbf{F}_{HLL} = \frac{S_R\mathbf{F}_L - S_L\mathbf{F}_R + S_L S_R\left(\mathbf{U}_R - \mathbf{U}_L\right)}{S_R - S_L}. \tag{4.10}$$

The HLLC solver is a three waves model with the addition of a contact wave onto the existing two waves in HLL. This results in two intermediate states U_L^* and U_R^*, separated by an interface travelling at speed S^*. The HLLC approximate Riemann solution is

$$\mathbf{U}_{HLLC}(x,t) = \begin{cases} \mathbf{U}_L, & \text{if} \quad \frac{x}{t} \leq S_L \\ \mathbf{U}_L^*, & \text{if} \quad S_L \leq \frac{x}{t} \leq S^* \\ \mathbf{U}_R^*, & \text{if} \quad S^* \leq \frac{x}{t} \leq S_R \\ \mathbf{U}_R, & \text{if} \quad \frac{x}{t} \geq S_R \end{cases} \tag{4.11}$$

where the U_L^* and U_R^* can be calculated using relationships derived from the Rankine-Hugoniot conditions

$$\mathbf{F}_L^* = \mathbf{F}_L + S_L\left(\mathbf{U}_L^* - \mathbf{U}_L\right), \tag{4.12}$$

$$\mathbf{F}_R^* = \mathbf{F}_R + S_R\left(\mathbf{U}_R^* - \mathbf{U}_R\right). \tag{4.13}$$

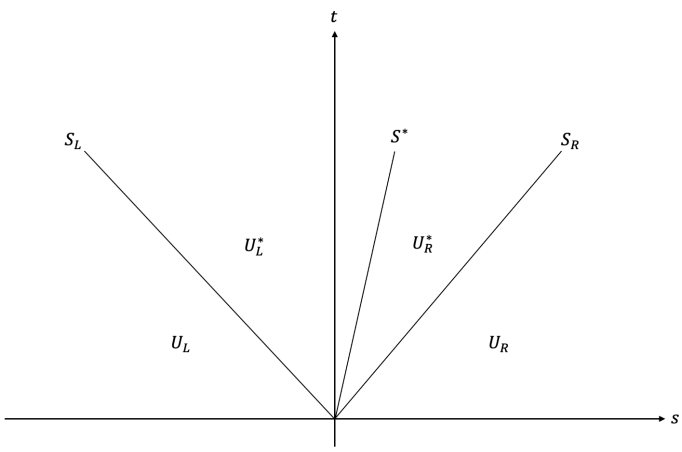

Fig. 4.2 HLLC approximate Riemann solver. Solution in the star regions consist of two constant states separated from each other by the intermediate wave speed [60]

Wave Speed Estimate

To use the approximate Riemann solvers, bound estimates for the two fastest wave speeds emerging from the solution of the Riemann problem needs to be provided. Using Davis [10] estimate for wave speed bound, the minimum and maximum wave speeds S_L and S_R can be computed from the fluid velocity u and speed of sound c as follows

$$S_L = \min\left(u_L - c_L, u_R - c_R\right), \quad S_R = \max\left(u_L + c_L, u_R + c_R\right). \tag{4.14}$$

Using the mixture density and mixture pressure, the intermediate wave speed, S^* can be calculated from

$$S^* = \frac{\left(\rho u^2 + p\right)_L - \left(\rho u^2 + p\right)_R - S_L(\rho u)_L + S_R(\rho u)_R}{(\rho u)_L - (\rho u)_R - S_L\rho_L + S_R\rho_R}. \tag{4.15}$$

4.1.4 Primitive Variable MUSCL Hancock Scheme

Due to Diffuse Interface Method (DIM)'s non-conservative nature, second order Total Variation Diminishing (TVD) upwind primitive variable scheme is used to extend the numerical simulation to second order accurate [60]. The TVD properties of the solver are maintained by applying the slope limiter within the Monotone Upstream-centred Schemes for Conservation Law (MUSCL) method.

Data reconstruction

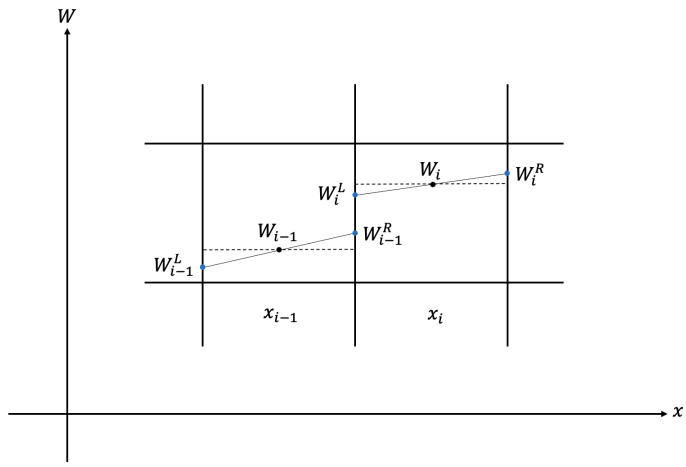

Fig. 4.3 Data reconstruction. The piecewise linear extrapolation stage in MUSCL-Hancock for any primitive variable W [38].

The MUSCL approach allows the construction of higher order schemes by modifying the piece-wise constant data. The first step for constructing a second order extension flux $\mathbf{F}_{i+0.5}$ is to replace the cell averaged values by reconstructed boundary values using derivative approximation.

$$\mathbf{\Delta}_i = \frac{1}{2}\mathbf{\Delta}_{i-1/2} + \frac{1}{2}\mathbf{\Delta}_{i+1/2} \tag{4.16}$$

$$\mathbf{\Delta}_{i-1/2} = \mathbf{W}_i^n - \mathbf{W}_{i-1}^n, \quad \mathbf{\Delta}_{i+1/2} = \mathbf{W}_{i+1}^n - \mathbf{W}_i^n \tag{4.17}$$

Given that derivatives do not exist at discontinuities, spurious oscillations can be generated in regions of strong gradients [60]. In order to construct a second order stable TVD scheme, the slopes Δ_i in the reconstruction steps are replaced with limited slopes $\bar{\Delta}_i = \phi_i \Delta_i$, according to some TVD constraints. The reconstruction is fully limited to piece-wise constant in cases of high change in slope while no limiting is applied in cases of smooth change in slope. MINMOD, SUPERBEE or VAN LEER-type slope limiter can be used to limit the slopes.

Initial definitions (r here represents the slope ratio):

$$r = \frac{\Delta_{i-1/2}}{\Delta_{i+1/2}} = \frac{W_i - W_{i-1}}{W_{i+1} - W_i}, \quad \xi_L(r) = \frac{2r}{1+r}, \quad \xi_R(r) = \frac{2}{1+r} \tag{4.18}$$

A MINMOD (MINBEE) type slope limiter is

$$\phi(r) = \begin{cases} 0 & r \leq 0 \\ r & 0 < r \leq 1 \\ 1 & r > 1 \end{cases} \tag{4.19}$$

A VAN-LEER type slope limiter is

$$\phi(r) = \begin{cases} 0 & r \leq 0 \\ \min\left(\xi_L(r), \xi_R(r)\right) & r > 0 \end{cases} \tag{4.20}$$

A SUPERBEE type slope limiter is

$$\phi(r) = \begin{cases} 0, & \text{if } r \leq 0 \\ 2r, & \text{if } 0 \leq r \leq \frac{1}{2} \\ 1, & \text{if } \frac{1}{2} \leq r \leq 1 \\ \min\{r, \xi_R(r), 2\} & \text{if } r \geq 1 \end{cases} \tag{4.21}$$

The extrapolated primitive variable vectors $\overline{\mathbf{W}}_i^L$ and $\overline{\mathbf{W}}_i^R$ for the left and right boundary of cell i are computed from

$$\begin{aligned} \overline{\mathbf{W}}_i^L &= \mathbf{W}_i^n - \frac{1}{2}\overline{\mathbf{\Delta}}_i = \mathbf{W}_i^n - \frac{1}{2}\phi(r)\mathbf{\Delta}_i, \\ \overline{\mathbf{W}}_i^R &= \mathbf{W}_i^n + \frac{1}{2}\overline{\mathbf{\Delta}}_i = \mathbf{W}_i^n + \frac{1}{2}\phi(r)\mathbf{\Delta}_i. \end{aligned} \tag{4.22}$$

Half Time Step Evolution

Within each cell, the boundary extrapolated values are evolved locally at half-time step as

$$\begin{aligned} \overline{\mathbf{W}}_i^{L,n+1/2} &= \overline{\mathbf{W}}_i^L + \frac{1}{2}\frac{\Delta t}{\Delta x} A\left(\mathbf{W}_i\right)\left[\overline{\mathbf{W}}_i^L - \overline{\mathbf{W}}_i^R\right], \\ \overline{\mathbf{W}}_i^{R,n+1/2} &= \overline{\mathbf{W}}_i^R + \frac{1}{2}\frac{\Delta t}{\Delta x} A\left(\mathbf{W}_i\right)\left[\overline{\mathbf{W}}_i^L - \overline{\mathbf{W}}_i^R\right] \end{aligned} \tag{4.23}$$

where $A\left(\mathbf{W}_i\right)$ is the matrix in primitive variable form $\frac{\partial W}{\partial t} + A(W)\frac{\partial W}{\partial x} = 0$. The evolved boundary values $\overline{\mathbf{W}}_i^{L,n+1/2}$ and $\overline{\mathbf{W}}_i^{R,n+1/2}$ are then treated as the initial values for the HLLC Riemann Solver to produce second order accurate numerical simulation. Once the intercell

fluxes are computed, Godunov's method is used to update the data.

$$\begin{aligned} F^*_{i-1/2} &= F^*_{i-1/2}\left(W^{n+1/2}_{i-1,R}, W^{n+1/2}_{i,L}\right) \\ F^*_{i+1/2} &= F^*_{i+1/2}\left(W^{n+1/2}_{i,R}, W^{n+1/2}_{i+1,L}\right) \end{aligned} \tag{4.24}$$

4.1.5 Multidimensional Simulation

To extend the system to 2-D, dimensional splitting was first tested with the C_{cfl} remain unchanged for the simulation. However, for the two phase cavitation model proposed by Saurel et al. [56], the simulation was unstable from the start and eventually crashed before the end time. Hence, dimensional un-split method is used in this dissertation with a reduced C_{cfl} coefficient.

$$\frac{\partial \mathbf{U}}{\partial t} + \frac{\partial \mathbf{F}}{\partial x} + \frac{\partial \mathbf{G}}{\partial y} = 0 \tag{4.25}$$

$$\mathbf{U}^{n+1}_{i,j} = \mathbf{U}^n_{i,j} - \frac{\Delta t}{\Delta x}\left(\mathbf{F}^n_{i+1/2,j} - \mathbf{F}^n_{i-1/2,j}\right) - \frac{\Delta t}{\Delta y}\left(\mathbf{G}^n_{i,j+1/2} - \mathbf{G}^n_{i,j-1/2}\right) \tag{4.26}$$

In the conservative update equation (4.26), $\mathbf{F}^n_{i\pm1/2,j}$ are the x-fluxes while $\mathbf{G}^n_{i,j\pm1/2}$ are the y-fluxes. Note that the x-fluxes are effectively 1-D (constant j-index), as are the y-fluxes (constant i-index). The same time step is required for both x- and y-updates. For the system to be stable for both updates, time step can be computed as

$$\Delta t = C_{\text{cfl}} \frac{\min(\Delta x, \Delta y)}{S^n_{\max}}, \tag{4.27}$$

where $S^n_{\max} = \max_{i,j}\left\{\left|\mathbf{u}^n_{i,j}\right| + c^n_{i,j}\right\}$. can be computed from the magnitude of the velocity vector and C_{cfl} is the CFL number.

In 2D, material moves diagonally on the grid. Technically, over a single time step, material from a cell $\left(x_i, y_j\right)$ should end up in the cell $\left(x_{i\pm1}, y_{j\pm1}\right)$. The numerical scheme used in this dissertation requires two time steps for material to move into the correct cell. Hence, the stable time step must be halved to ensure material can reach these offset cells, whilst not overlapping a single cell in regions where velocity is aligned to the grid.

$$C_{\text{cfl}} = \frac{1}{2} C_{\text{cfl,1D}} \tag{4.28}$$

4.1.6 Operator Splitting

In-homogeneous system of equations arise naturally in many problems of practical interest. For the multi-material DIM models, the system of equations can be separated into two parts: a conservative hyperbolic part for every spatial dimensions and non-conservative terms from the volume fraction, momentum and internal energy updates. In addition, source terms accounting for the geometric effect such as cylindrical geometry alter the homogeneity of the system of equations.

$$\mathbf{U}_t + \mathbf{F}(\mathbf{U})_x + \mathbf{G}(\mathbf{U})_y = \mathbf{S}_{\text{non-con.}} + \mathbf{S}_g \tag{4.29}$$

Adopting operator splitting, the conservative part of the equations can first be solved using the HLLC solver discussed in Section 4.1.3 as

$$\left.\begin{array}{ll} \text{PDE} : & \mathbf{U}_t + \mathbf{F}(\mathbf{U})_x + \mathbf{G}(\mathbf{U})_y = \mathbf{0}, \\ \text{IC} & : \mathbf{U}(x, t^n) = \mathbf{U}^n \end{array}\right\} \Longrightarrow \overline{\mathbf{U}}^{n+1}. \tag{4.30}$$

The source term is then solved using a first order update and solutions from the previous step as the initial condition

$$\left.\begin{array}{ll} \text{ODE} : & \frac{d}{dt}\mathbf{U} = \mathbf{S}(\mathbf{U}), \\ \text{IC} & : \overline{\mathbf{U}}^{n+1} \end{array}\right\} \Longrightarrow \mathbf{U}^{n+1}, \tag{4.31}$$

where $\mathbf{S}(\mathbf{U})$ represents the sum of $\mathbf{S}_{\text{non-con.}}$,$\mathbf{S}_g$. Both the source terms will be discussed in details as follows

- It is worth noting that the two phase model proposed by Saurel et al. [56] adds the non-conservative source terms within the hyperbolic step in a similar approach taken by Allaire et al. [1]. Additionally, the authors use the speed of contact discontinuity to update the non-conservative terms. This will be discussed in details in Section 4.2.2.

- For test cases with cylindrical symmetry, the simulation can be extended to 2-D revolutions by an appropriate choice of coordinates. The partial derivatives (divergence terms) are treated accordingly which result in extra source fluxes accounting for the coordinate transformation. For the two phase model proposed by Saurel et al. [56], the

source terms accounting for the cylindrical geometry are

$$\mathbf{U} = \begin{pmatrix} \alpha_1 \\ \alpha_1\rho_1 \\ \alpha_2\rho_2 \\ \alpha_1\rho_1 e_1 \\ \alpha_2\rho_2 e_2 \\ \rho u_r \\ \rho E \\ \rho u_z \end{pmatrix}, \quad \mathbf{S}_g = -\frac{1}{r}\begin{pmatrix} 0 \\ \alpha_1\rho_1 u_r \\ \alpha_2\rho_2 u_r \\ \alpha_1\rho_1 e_1 u_r \\ \alpha_2\rho_2 e_2 u_r \\ \rho u_r u_r \\ (\rho E + P)u_r \\ \rho u_r u_z \end{pmatrix}. \tag{4.32}$$

4.2 Two Phase Model (Saurel et al. [56])

The system of seven equations is evolved using the finite volume method with the fluxes being computed from the MUSCL Hancock HLLC Riemann solver. For the conservative part of the system, the variables are updated using the conventional Godunov scheme; for the non-conservative part, special treatment is required before the update. After the Godunov update, the pressure equilibrium assumption is relaxed, and the resulting relaxation terms are solved.

4.2.1 HLLC Riemann Solver

By applying the Rankine-Hugoniot relationship, the intermediate states bounded by the minimum and maximum wave speeds can be computed as follows

$$(\alpha_k\rho_k)_R^* = (\alpha_k\rho_k)_R \frac{S_R - u_R}{S_R - S^*}, \tag{4.33a}$$

$$(\alpha_k\rho_k)_L^* = (\alpha_k\rho_k)_L \frac{S_L - u_L}{S_L - S^*}, \tag{4.33b}$$

$$p^* = p_R + \rho_R u_R (u_R - S_R) - \rho_R^* S^* (S^* - S_R), \quad \text{with } \rho_R^* = \sum_k (\alpha_k\rho_k)_R^*, \tag{4.33c}$$

$$E_R^* = \frac{\rho_R E_R (u_R - S_R) + p_R u_R - p^* S^*}{\rho_R^* (S^* - S_R)}, \tag{4.33d}$$

$$E_L^* = \frac{\rho_L E_L (u_L - S_L) + p_L u_L - p^* S^*}{\rho_L^* (S^* - S_L)}, \quad \text{with } E = Y_1 e_1 + Y_2 e_2 + \frac{1}{2}u^2. \tag{4.33e}$$

In the absence of relaxation effects, the volume fraction remains unchanged along the fluid trajectories. The volume fraction jump can be obtained from

$$\alpha_{kR}^{*} = \alpha_{kR}, \quad \alpha_{kL}^{*} = \alpha_{kL}. \tag{4.34}$$

Given the volume fraction is uniform, the fluid density can be calculated from a simplified relationship

$$\rho_{kR}^{*} = \rho_{kR} \frac{u_R - S_R}{S_M - S_R}. \tag{4.35}$$

For computing the specific internal energies from the EOS $e_{kR}^{*} = e_{kR}^{*}\left(p_k^{*}, \rho_k^{*}\right)$, phasic pressures must first be determined. Using the EOS, the phasic pressures are constrained along their Hugoniot curves to be a function only of the corresponding fluid density

$$p_k^{*}\left(\rho_k^{*}\right) = \left(p_k + p_{\infty k}\right) \frac{\left(\gamma_k - 1\right)\rho_k - \left(\gamma_k + 1\right)\rho_k^{*}}{\left(\gamma_k - 1\right)\rho_k^{*} - \left(\gamma_k + 1\right)\rho_k} - p_{\infty k}. \tag{4.36}$$

4.2.2 Godunov Update

For the evolution equations having no relaxation terms, the conservative variables are updated using the conventional Godunov scheme

$$U_i^{n+1} = U_i^n - \frac{\Delta t}{\Delta x}\left(F\left(U_i^n, U_{i+1}^n\right) - F\left(U_{i-1}^n, U_i^n\right)\right), \tag{4.37}$$

where $U = \left((\alpha\rho)_1, (\alpha\rho)_2, \rho u, \rho E\right)^{\mathrm{T}}$ and $F = \left((\alpha\rho)_1 u, (\alpha\rho)_2 u, \rho u^2 + p, (\rho E + p)u\right)^{\mathrm{T}}$, $E = Y_1 e_1 + Y_2 e_2 + \frac{1}{2}u^2$ and $p = \alpha_1 p_1 + \alpha_2 p_2$.

To deal with the non-conservative part of the equations, the volume fraction equation is being rewritten into the form of "conservation plus source term".

$$\frac{\partial \alpha_1}{\partial t} + u\frac{\partial \alpha_1}{\partial x} = 0 \Rightarrow \frac{\partial \alpha_1}{\partial t} + \frac{\partial u\alpha_1}{\partial x} = \alpha_1 \frac{\partial u}{\partial x} \tag{4.38}$$

The flux term $F = u\alpha_1$ is computed using the standard HLLC approach and the source term is solved using a first order update. The Godunov update for volume fraction takes the following form

$$\alpha_{1,i}^{n+1} = \alpha_{1,i}^{n} - \frac{\Delta t}{\Delta x}\left(\left(u\alpha_1\right)_{i+1/2}^{*} - \left(u\alpha_1\right)_{i-1/2}^{*} - \alpha_{1,i}^{n}\left(S_{i+1/2}^{*} - S_{i-1/2}^{*}\right)\right), \tag{4.39}$$

where $\alpha_{1,i}^n$ is the volume fraction from time t^n and $S_{i\pm1/2}^*$ is the intermediate wave speed from HLLC solver.

For the non-conservative internal energy equations, accurate approximations in the presence of shocks is nearly impossible. Hence, the simplest approximation of constant product $(\alpha p)_{k,i}^n$ during the time step is used for updating these terms.

$$(\alpha\rho e)_{k,i}^{n+1} = (\alpha\rho e)_{k,i}^n - \frac{\Delta t}{\Delta x}\left((\alpha\rho eu)_{k,i+1/2}^* - (\alpha\rho eu)_{k,i-1/2}^* + (\alpha p)_{k,i}^n\left(S_{i+1/2}^* - S_{i-1/2}^*\right)\right) \tag{4.40}$$

The lack of accuracy in internal energies are not a major concern here as they are only used for estimating the phasic pressures at the end of the hyperbolic step. After every Godunov update, the pressure relaxation and reinitialisation step described in Section 3.4.1 and 3.4.1 respectively are implemented to apply thermodynamic consistent corrections.

4.2.3 Second Order Extension

The primitive variable MUSCL-Hancock scheme described in Section 4.1.4 is used to extend the cavitation model to second order accurate. Ignoring the source terms, the system of equations (3.28a) to (3.28g) can be rewritten into primitive variable form as below

$$\frac{\partial\alpha_1}{\partial t} + u\frac{\partial\alpha_1}{\partial x} = 0 \tag{4.41a}$$

$$\frac{\partial\rho_1}{\partial t} + u\frac{\partial\rho_1}{\partial x} + \rho_1\frac{\partial u}{\partial x} = 0 \tag{4.41b}$$

$$\frac{\partial\rho_2}{\partial t} + u\frac{\partial\rho_2}{\partial x} + \rho_2\frac{\partial u}{\partial x} = 0 \tag{4.41c}$$

$$\frac{\partial u}{\partial t} + u\frac{\partial u}{\partial x} + \frac{1}{\rho}\frac{\partial p}{\partial x} = 0 \quad \text{or} \quad \frac{\partial u}{\partial t} + u\frac{\partial u}{\partial x} + \frac{p_1 - p_2}{\rho}\frac{\partial\alpha_1}{\partial x} + \frac{\alpha_1}{\rho}\frac{\partial p_1}{\partial x} + \frac{(1-\alpha_1)}{\rho}\frac{\partial p_2}{\partial x} = 0 \tag{4.41d}$$

$$\frac{\partial p_1}{\partial t} + u\frac{\partial p_1}{\partial x} + \rho_1 c_1^2\frac{\partial u}{\partial x} = 0 \tag{4.41e}$$

$$\frac{\partial p_2}{\partial t} + u\frac{\partial p_2}{\partial x} + \rho_2 c_2^2\frac{\partial u}{\partial x} = 0 \tag{4.41f}$$

with $W = (\alpha_1, \rho_1, \rho_2, u, p_1, p_2)^t$ and $A(W) = \begin{pmatrix} u & 0 & 0 & 0 & 0 & 0 \\ 0 & u & 0 & \rho_1 & 0 & 0 \\ 0 & 0 & u & \rho_2 & 0 & 0 \\ \frac{p_1-p_2}{\rho} & 0 & 0 & u & \frac{\alpha_1}{\rho} & \frac{1-\alpha_1}{\rho} \\ 0 & 0 & 0 & \rho_1 c_1^2 & u & 0 \\ 0 & 0 & 0 & \rho_2 c_2^2 & 0 & u \end{pmatrix}$.

4.3 Phase Change Model (Wilkinson et al. [63])

As the phase change model proposed by Wilkinson et al. is integrated into Allaire et al.'s model, the numerical method described here is essentially solving the five equations multi-material model. The phase change physics are all encoded within the EOS described in Section 3.4.2. It can also be seen as a trimmed down version of the numerical method used for solving Saurel et al.'s two phase model as the evolution equations for specific internal energies are no longer required.

4.3.1 HLLC Riemann solver

The HLLC Riemann solver uses the same equations as (4.33a)-(4.35) for solving the intermediate states. For computing the wave speed bound required for approximate Riemann solver, special treatment on the speed of sound is needed for simulation involving material undergoing phase change and this can be computed according to Section 3.4.2.

4.3.2 Godunov Update

Apart from the volume fraction variable, the rest of the conservative variables are updated using the conventional Godunov scheme (4.37). The volume fraction can be updated in the same way as the two phase model (4.39).

4.3.3 Second Order Extension

The primitive variable MUSCL-Hancock scheme described in Section 4.1.4 is used to extend the cavitation model to second order accurate. Ignoring the source terms, the system of equations (3.19a) to (3.19e) can be rewritten into primitive variable form as follows

$$\frac{\partial \alpha_1}{\partial t} + u\frac{\partial \alpha_1}{\partial x} = 0 \tag{4.42a}$$

$$\frac{\partial \rho_1}{\partial t} + u\frac{\partial \rho_1}{\partial x} + \rho_1\frac{\partial u}{\partial x} = 0 \tag{4.42b}$$

$$\frac{\partial \rho_2}{\partial t} + u\frac{\partial \rho_2}{\partial x} + \rho_2\frac{\partial u}{\partial x} = 0 \tag{4.42c}$$

$$\frac{\partial u}{\partial t} + u\frac{\partial u}{\partial x} + \frac{1}{\rho}\frac{\partial p}{\partial x} = 0 \tag{4.42d}$$

$$\frac{\partial p}{\partial t} + u\frac{\partial p}{\partial x} + \rho c^2\frac{\partial u}{\partial x} = 0 \tag{4.42e}$$

with $W = (\alpha_1, \rho_1, \rho_2, u, p)^t$ and $A(W) = \begin{pmatrix} u & 0 & 0 & 0 & 0 \\ 0 & u & 0 & \rho_1 & 0 \\ 0 & 0 & u & \rho_2 & 0 \\ 0 & 0 & 0 & u & \frac{1}{\rho} \\ 0 & 0 & 0 & \rho c^2 & u \end{pmatrix}$.

Chapter 5

Validation Tests

In this chapter, several 1-D and 2-D test cases have been chosen to test the underlying equations, both with and without cavitation behaviour. The first few tests are the single material test cases proposed by Toro [60] to test the model's hydrodynamic properties. In addition, test cases involving multi-material such as water, air and helium have been used to check the model's handling of systems having more than one material. Furthermore, test cases involving phase change due to large pressure and velocity change are adopted to test the model's capability in modelling cavitation. Lastly, ultrasonic excitation is added to the boundary condition of the liquid droplet impacting wall test case to test the cavitation phenomena of the droplet.

5.1 Single-Material Test

These are the simplest test cases adopted from Toro's book [60] to validate the hydrodynamic behaviour of Allaire et al.'s five equations multi-material code. For all the test cases, air is initiated everywhere with $\gamma = 1.4$ and $p_\infty = 0$ hence the EOS used in these simulations is ideal gas EOS. MUSCL-Hancock HLLC Riemann solver with Van-Leer slope limiter is used to produce second order accurate simulations. The reader is encouraged to refer to Chapter 4 and 17 of Toro's book for more details of the test cases.

5.1.1 1-D Sod Test

The initial condition for the 1-D test problems are recorded in Table 5.1. The tests are simulated on several grid resolutions of $N = 200, 400$ across the simulation domain of $x \in \{0, 1\}$ with the initial discontinuity at $x = 0.5$. On the left side of simulation domain ($x < 0.5$), the materials are initiated with $\alpha_1 = 1 - 10^{-6}$; On the right side ($x > 0.5$), the materials are initiated with $\alpha_1 = 10^{-6}$. Transmissive boundary condition and $C_{cfl} = 0.7$ are applied to all the test cases. The plots for density, velocity, pressure and specific internal energy are produced for all the test cases. The exact solution for all the test cases are computed using the exact Riemann Solver and presented in Figure 5.1- 5.5.

Table 5.1 Initial data for Toro's test.

Test	W_1	**Value**	W_2	**Value**	Time
1	ρ_1	1.0	ρ_2	0.125	0.25
	u_1	0.0	u_2	0.0	
	p_1	1.0	p_2	0.1	
2	ρ_1	1.0	ρ_2	1.0	0.15
	u_1	-2.0	u_2	2.0	
	p_1	0.4	p_2	0.4	
3	ρ_1	1.0	ρ_2	1.0	0.012
	u_1	0.0	u_2	0.0	
	p_1	1000.0	p_2	0.01	
4	ρ_1	1.0	ρ_2	1.0	0.035
	u_1	0.0	u_2	0.0	
	p_1	0.01	p_2	100.0	
5	ρ_1	5.99924	ρ_2	5.99242	0.035
	u_1	19.5975	u_2	-6.19633	
	p_1	460.894	p_2	46.0950	

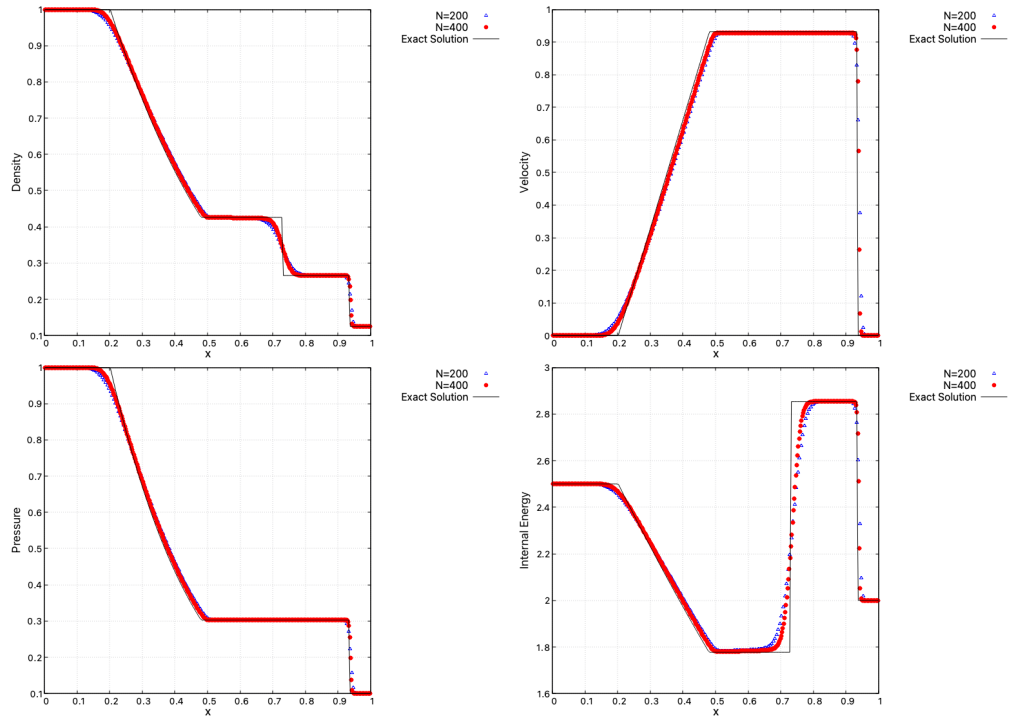

Fig. 5.1 *Toro's test 1* at t = 0.25s

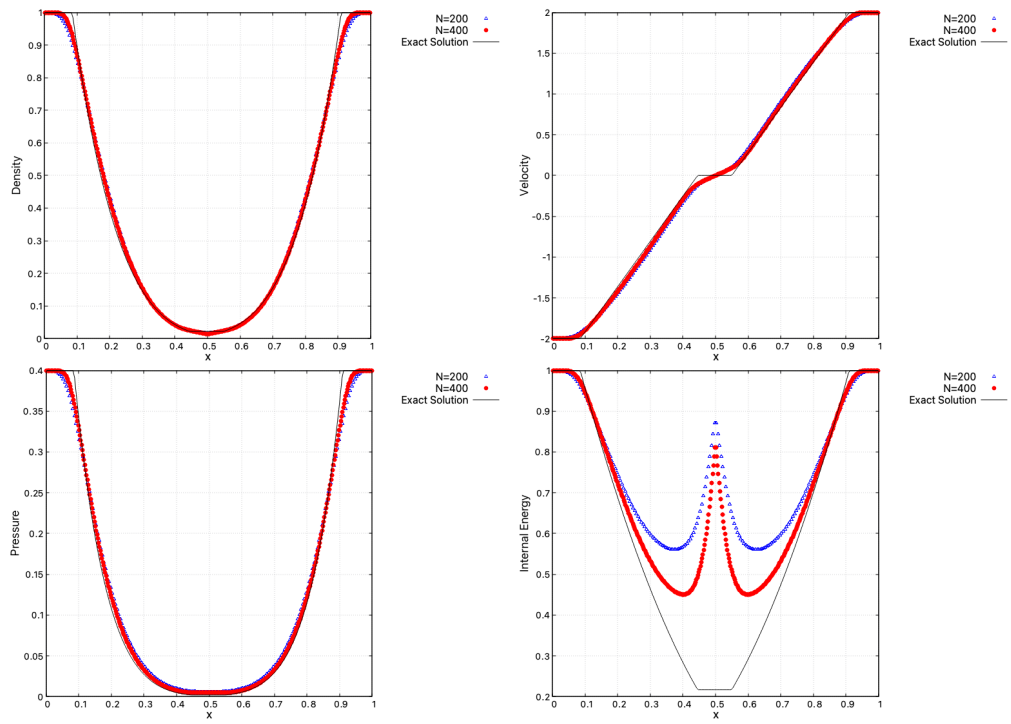

Fig. 5.2 *Toro's test 2* at t = 0.15s

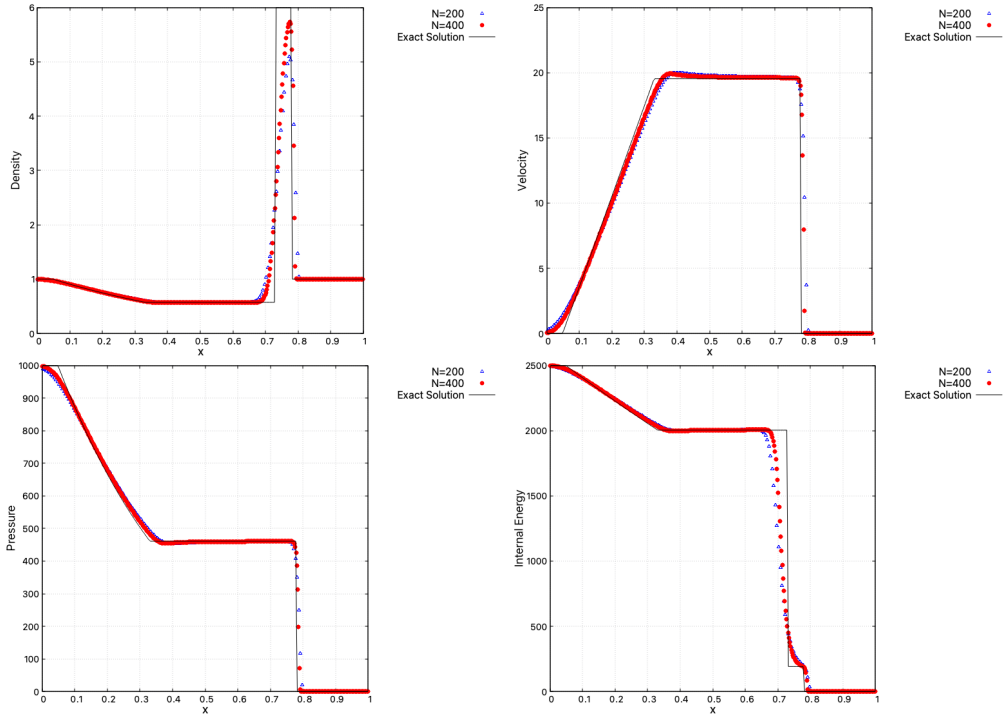

Fig. 5.3 *Toro's test 3* at t = 0.012s

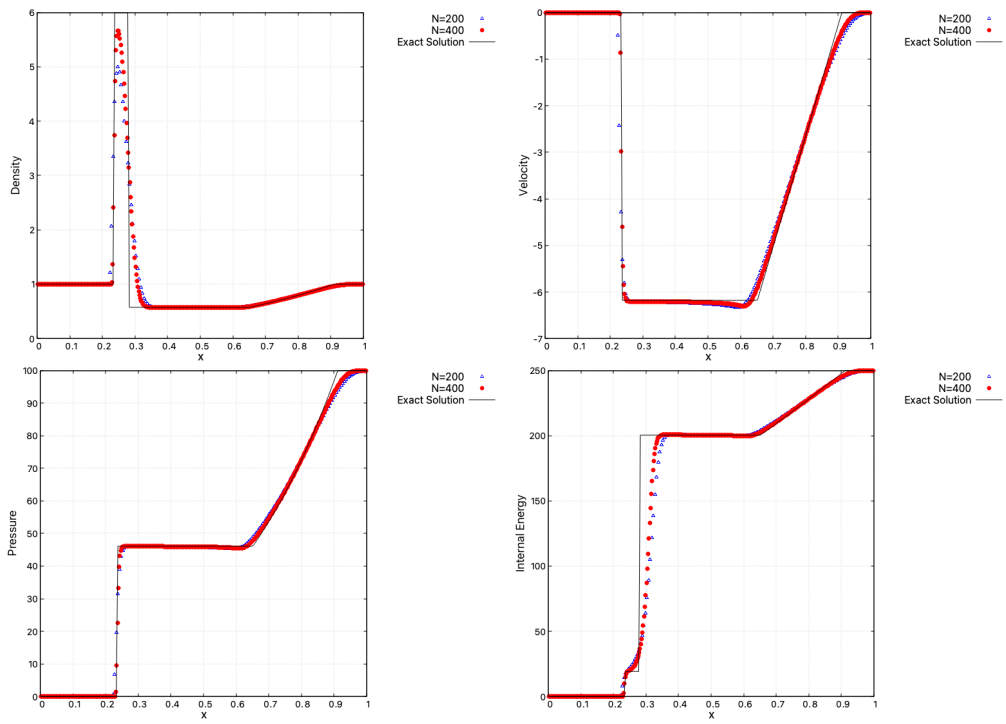

Fig. 5.4 *Toro's test 4* at t = 0.035s

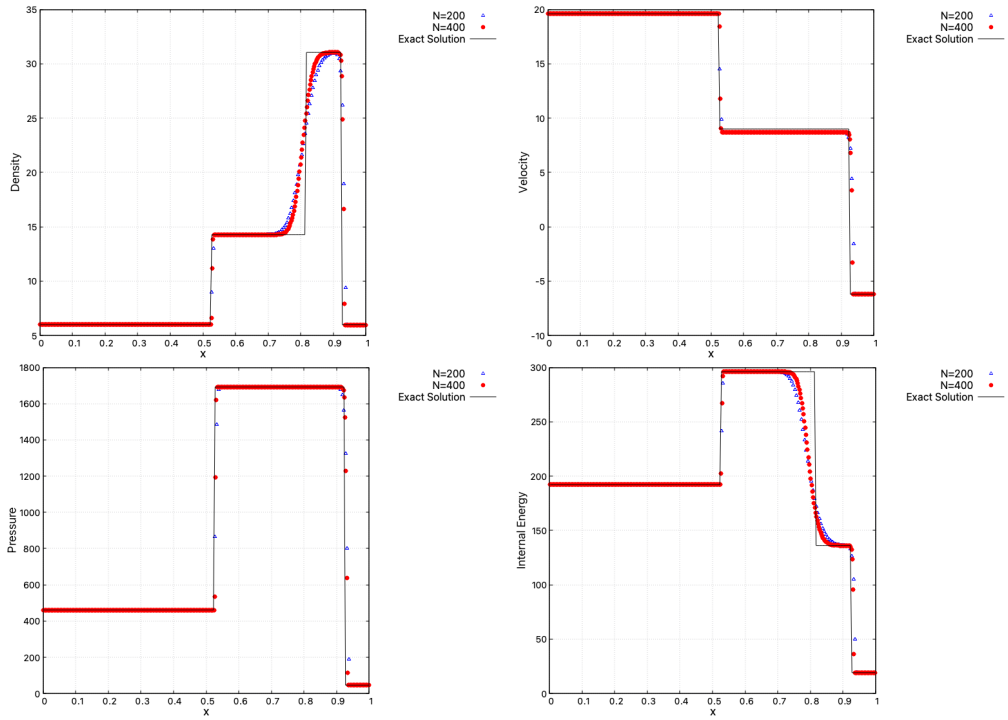

Fig. 5.5 *Toro's test 5* at t = 0.035s

5.1.2 2-D Cylindrical Explosion Test

For this test case, the 2-D multi-material equations are solved on a square domain of $x \in \{0,2\}, y \in \{0,2\}$. The initial condition is made up of a region inside a circle of radius $R = 0.4$ centred at $(1,1)$ and a region outside the circle. The materials are initiated with $\alpha_1 = 1 - 10^{-6}$ inside the circle and $\alpha_1 = 10^{-6}$ outside. Transmissive boundary condition is applied in this test case. $C_{cfl} = 0.3$ is used for this simulation and the mesh resolution is $N = 200 \times 200$ cells. 2-D plots are produced at the output time $t = 0.25$ and presented in Figure 5.6. The values of the initial condition are as follows

$$\begin{aligned} \rho_1 &= 1.0, & \rho_2 &= 0.125, \\ u_{x,1} &= 0.0, & u_{x,2} &= 0.0, \\ u_{y,1} &= 0.0, & u_{y,2} &= 0.0, \\ p_1 &= 1.0, & p_2 &= 0.1. \end{aligned} \tag{5.1}$$

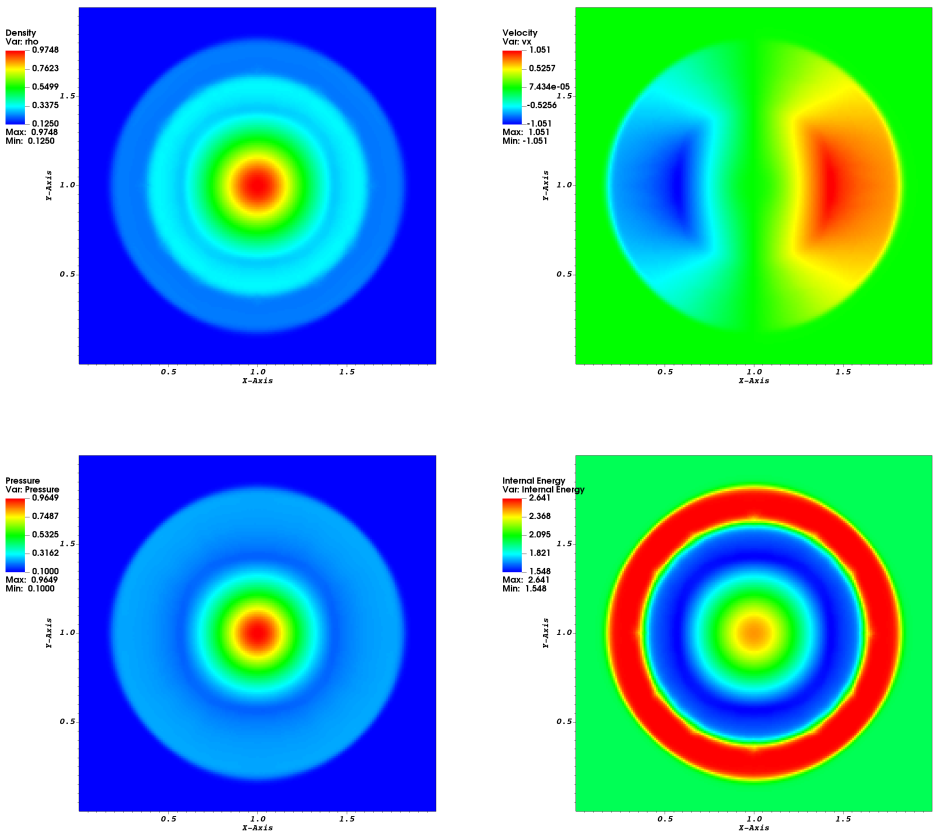

Fig. 5.6 *Cylindrical explosion test* at t = 0.25s

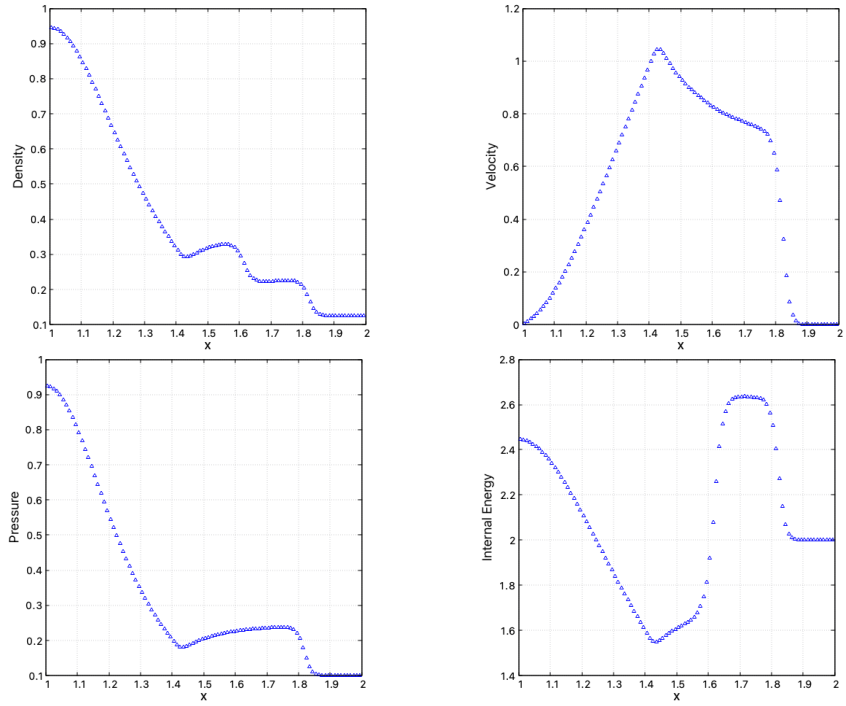

Fig. 5.7 *Cylindrical explosion test* 1-D slices from the midpoint in y-direction at t = 0.25s

The density plot shows the circular shock travelling outwards from the centre together with the contact surface and a circular rarefaction travelling towards the centre. As shown in the pressure plot, pressure is continuous across the contact surface. Comparing the 1-D plots with Figure 17.4 in Toro's book, the results here match all the characteristics shown in the exact solution. Note that for this dissertation, initial data within the quadrilateral cells cutting the initial discontinuity are not modified. This explains the small amplitude waves observed near the contact discontinuity formed at early times by the staircase configuration of initial data. This can be resolved by assigning modified area-weighted values to the appropriate cells at initial time and has been identified as a future improvement [60].

5.2 Multi-material Test

The five equations Allaire et al.'s model is tested with cases involving more than one material for its capability in performing multi-material simulations. The system of equations is solved using the MUSCL-Hancock HLLC Riemann solver with Van-Leer slope limiter.

5.2.1 Water-air Advection Test

A discontinuity of volume fraction at $x = 0.5m$ is introduced in a $1m$ length tube with water ($\alpha_1 = 1 - 10^{-6}$) in the left domain and air ($\alpha_1 = 10^{-6}$) in the right domain. The material in the tube is moving at a uniform velocity of $100m/s$ under a pressure of $1 \times 10^5 Pa$. The simulation is performed at $N = 1000$ cells with $C_{cfl} = 0.7$ and results are presented in Figure 5.8. The material properties and their respective stiffened gas EOS parameters are as follows

$$\begin{aligned} &\rho_1 = 1000\text{kgm}^{-3}, && \rho_2 = 10\text{kgm}^{-3}, \\ &\gamma_1 = 4.4, && \gamma_2 = 1.4, \\ &p_{\infty,1} = 6 \times 10^8 Pa, && p_{\infty,2} = 0. \end{aligned} \tag{5.2}$$

Given the flow is in mechanical equilibrium, pressure relaxation terms have no importance here. The maintenance of interface condition throughout the simulation proved the suitability of numerical approximation method adopted and the Godunov method of conservative and non-conservative equations.

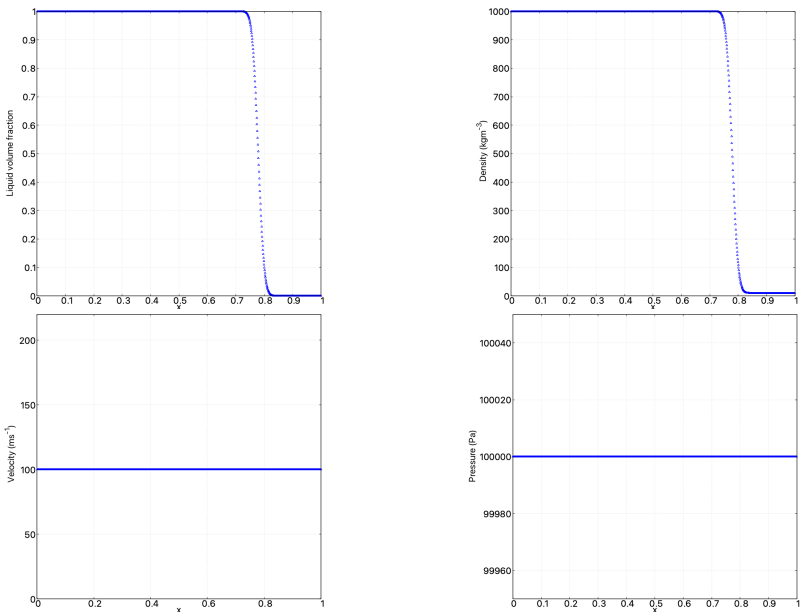

Fig. 5.8 *1D advection.* Plots showing advection of a volume fraction discontinuity in uniform pressure and velocity flow at time $t = 2.79ms$.

5.2.2 Helium Bubble Collapse Test

The second multi-material test case proposed by Layes and Le Métayer [29] involves a Mach 1.22 air shock collapsing a helium bubble. The initial set-up is presented in Figure 5.9 with the left domain filled with pre-shocked air and right domain with post shocked air. A helium bubble with radius $20mm$ is placed in the pre-shocked air centred at $x = 180mm, y = 0$. For this test case, air is being considered as material 1 regardless of pre- / post-shocked conditions and initiated everywhere ($\alpha_1 = 1 - 10^{-6}$) apart from the inner circle where helium is initiated as material 2 ($\alpha_1 = 10^{-6}$). The upper and lower boundary conditions are reflective solid wall boundaries; while the left and right boundaries are zero gradient for the flow variables. The simulation was performed on a resolution of $N = 1300 \times 350$ cells with $C_{cfl} = 0.3$. The non-dimensionalised initial conditions are

$$\begin{aligned} &(\rho_1 = 1, u_{x,1} = 0, u_{y,1} = 0, p_1 = 1, \gamma_1 = 1.4) \quad \text{pre-shocked air} \\ &(\rho_1 = 1.3764, u_{x,1} = -0.394, u_{y,1} = 0, p_1 = 1.5698, \gamma_1 = 1.4) \quad \text{post-shocked air} \\ &(\rho_2 = 0.138, u_{x,2} = 0, u_{y,2} = 0, p_2 = 1, \gamma_2 = 1.67) \quad \text{helium} \end{aligned} \tag{5.3}$$

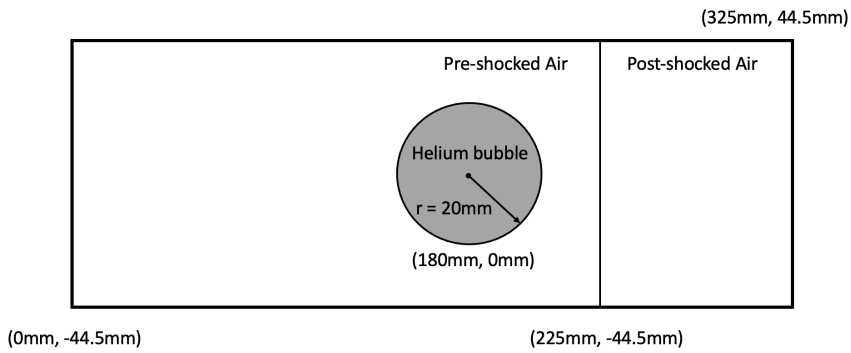

Fig. 5.9 Initial configuration of the helium bubble collapse test.

The direction of the shock wave propagation is from right to left of the domain. In this test case, the bubble is filled with helium which is lighter than air. Due to the difference in gas properties (density, acoustic impedance), vorticity generation is expected [29]. As shown in Figure 5.10, following the compression stage, a penetrating jet is developed along the axis of symmetry in the flow direction. This jet travels through the helium bubble and generates two consecutive vortexes. The vortexes remain attached to one another and not separated as shown in the experiment performed by Layes and Le Métayer [29] as the numerical methods adopted for performing the simulations differ.

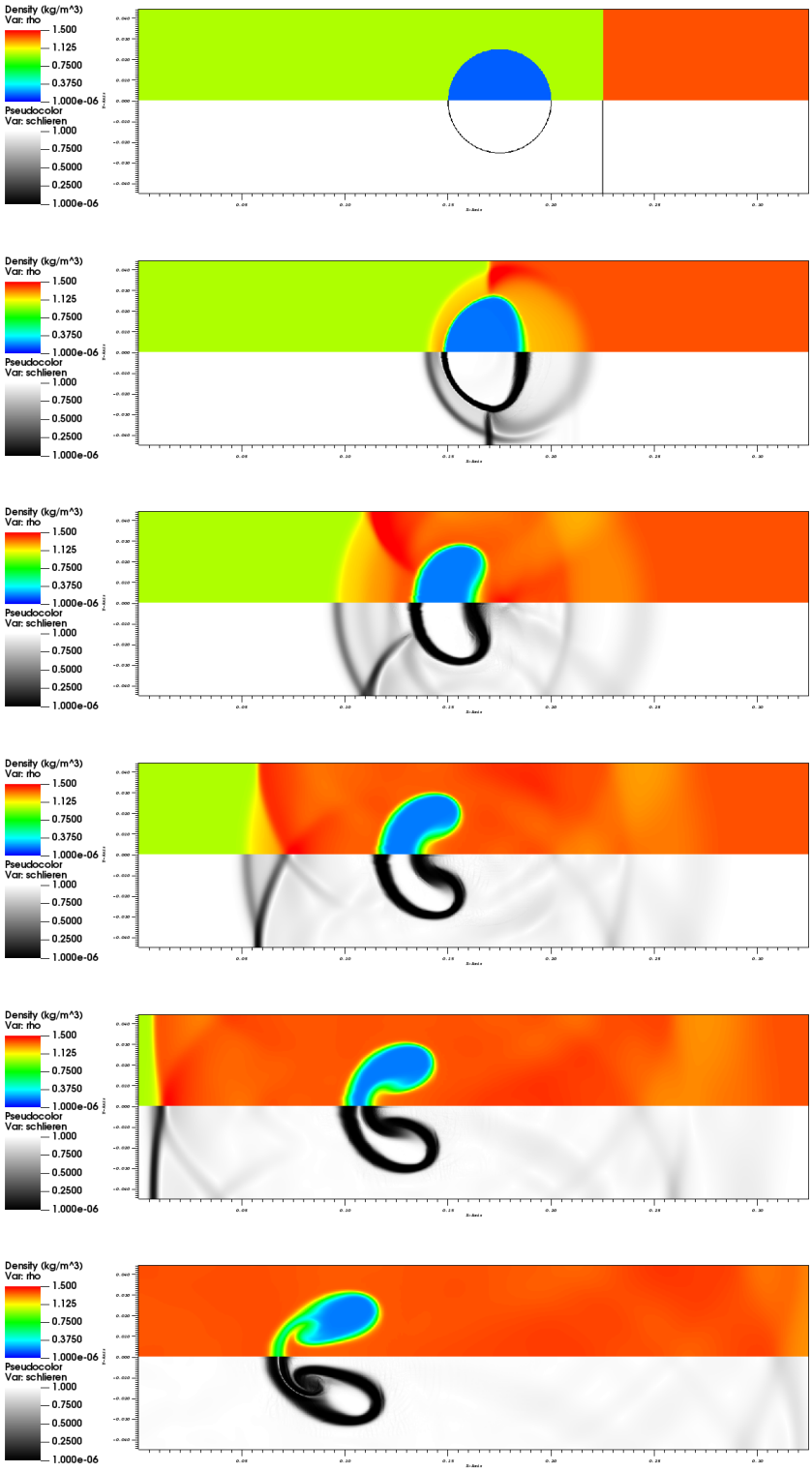

Fig. 5.10 *Helium bubble collapse.* The images show the mixture density plots on top and mock schlieren of the density at the bottom. The images are taken at time $t = 0.0s, 0.03s, 0.07s, 0.10s, 0.14s, 0.21s$.

5.3 Multiphase (Cavitation) Test

Several 1-D and 2-D cavitation test cases are extracted to validate the cavitation models (two phase model and phase change model) implemented. The MUSCL-Hancock HLLC Riemann solver with Van-Leer slope limiter is used to model these equations hence the simulations are second order accurate.

5.3.1 Two Rarefaction Induced Cavitation Test

The first test to illustrate the two phase model's capability in simulating cavitation is the one extracted from Dumbser et al. [13]. The initial settings consist of a 1m length tube filled with water ($\alpha_1 = 1 - 10^{-6}$) at atmospheric pressure and density $\rho_1 = 1000kg/m^3$. Initially, a small volume fraction of air ($\alpha_1 = 10^{-6}, \rho_2 = 1kg/m^3$) is present everywhere. At $x = 0.5m$, an initial velocity discontinuity is present with the left velocity $u_x = -100m/s$ and right velocity $u_x = 100m/s$. The simulation is performed using $N = 3000, 4000$ cells with $C_{cfl} = 0.7$ and results are presented as follows.

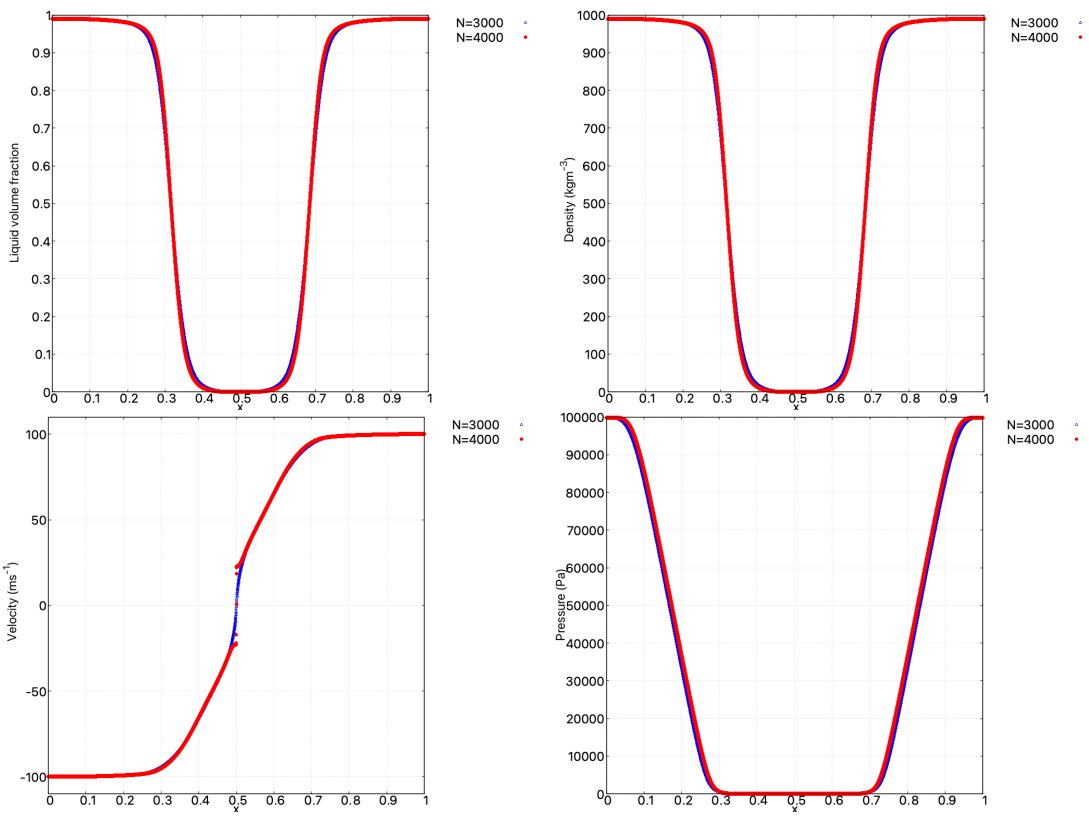

Fig. 5.11 *1D cavitation.* Plots showing expansion tube with cavitation pocket appearance at time $t = 1.85ms$.

The simulated results can be concluded to be in agreement with the one presented in Saurel et al.'s paper (Figure 5.14). The velocity discontinuity generated strong rarefaction waves propagating away from the centre of the tube. Given that phase transition is happening in this test case, the rarefaction waves are split into two: a fast rarefaction wave in the liquid and a slow wave. These phenomena are known as composite wave and described in details by Menikoff and Plohr [36]. The fast wave is responsible for the drastic pressure reduction in liquid while the slow wave is associated with small additional decrease in pressure and a dramatic reduction in density. As gas is initially present in the system, the gas volume fraction increases around the initial discontinuity and creates a cavitation pocket. This results in the dynamic appearance of two interfaces which were not present initially. The relaxation terms in the volume fraction and energy equations are responsible for this appearance. It is worth mentioning that high resolution simulation is required for this cavitation problem to accurately display the important but weak behaviours.

5.3.2 Cavitation Model Comparison

The 1-D cavitation test is repeated using the phase change model proposed by Wilkinson et al. [63] to compare the different approaches of modelling cavitation. For setting up the test case with phase change model, the test is initialised on a 1-D domain with water at Standard Temperature Pressure (STP) but with diverging flow velocity. In order to capture cavitation arising from an isentropic rarefaction of water at STP, the corresponding EOS parameters such as sound speed, pressure, enthalpy of vaporisation are selected from the IAPWS data. For the liquid EOS, the reference state corresponds to liquid water under STP; for the vapour EOS, the reference state is chosen at the vapour pressure corresponding to STP. The reference pressure is set to 1GPa for the liquid according to Le Métayer et al. [42] while the reference pressure for the vapour is chosen to be zero so the EOS reverts to ideal gas. The e_0 and s_0 for liquid are set using the enthalpy of vaporisation from IAPWS, $\Delta H = 2.442MJ$ and the condition of Gibbs energies must match on the saturation curve at $p = 3142Pa$. The parameters are summarised in Table 5.2.

The initial pressure and temperature are set to $1 \times 10^5 Pa$ and $298K$ across the whole domain. The left and right velocities from the discontinuity at $x = 1m$ are $-10m/s$ and $10m/s$ respectively. As the phase change model is integrated into Allaire et al.'s model, the domain is initiated with water with a small amount of gas ($\alpha_2 = 10^{-6}$) everywhere. The simulation is evolved for $5 \times 10^{-4}s$ at $C_{cfl} = 0.7$ over a $2m$ domain made up from $N = 5000, 10000$ cells to ensure most of the behaviours of interest are captured. Simulation results produced using the two models are presented in Figure 5.12 and these are comparable to the results produced by Saurel et al. [56] and Wilkinson et al. [63] in Figure 5.14.

Table 5.2 Table of reference states from IAPWS [61] and the resulting parameters for the equation of state for water

Reference state for water					
Phase	ρkg/m^3	p Pa	T K	c m/s	γ
Liquid	997.08	101000	298	1501.5	2.2479
vapour	0.02288	3142	298	426.52	1.3247
Phase	p_∞Pa	c_v J/(kgK)	e_0J/kg	s_0J/(kgK)	
Liquid	1e9	2696.9	-3.6884e6	34011	
Vapour	0	1419.1	0	0	

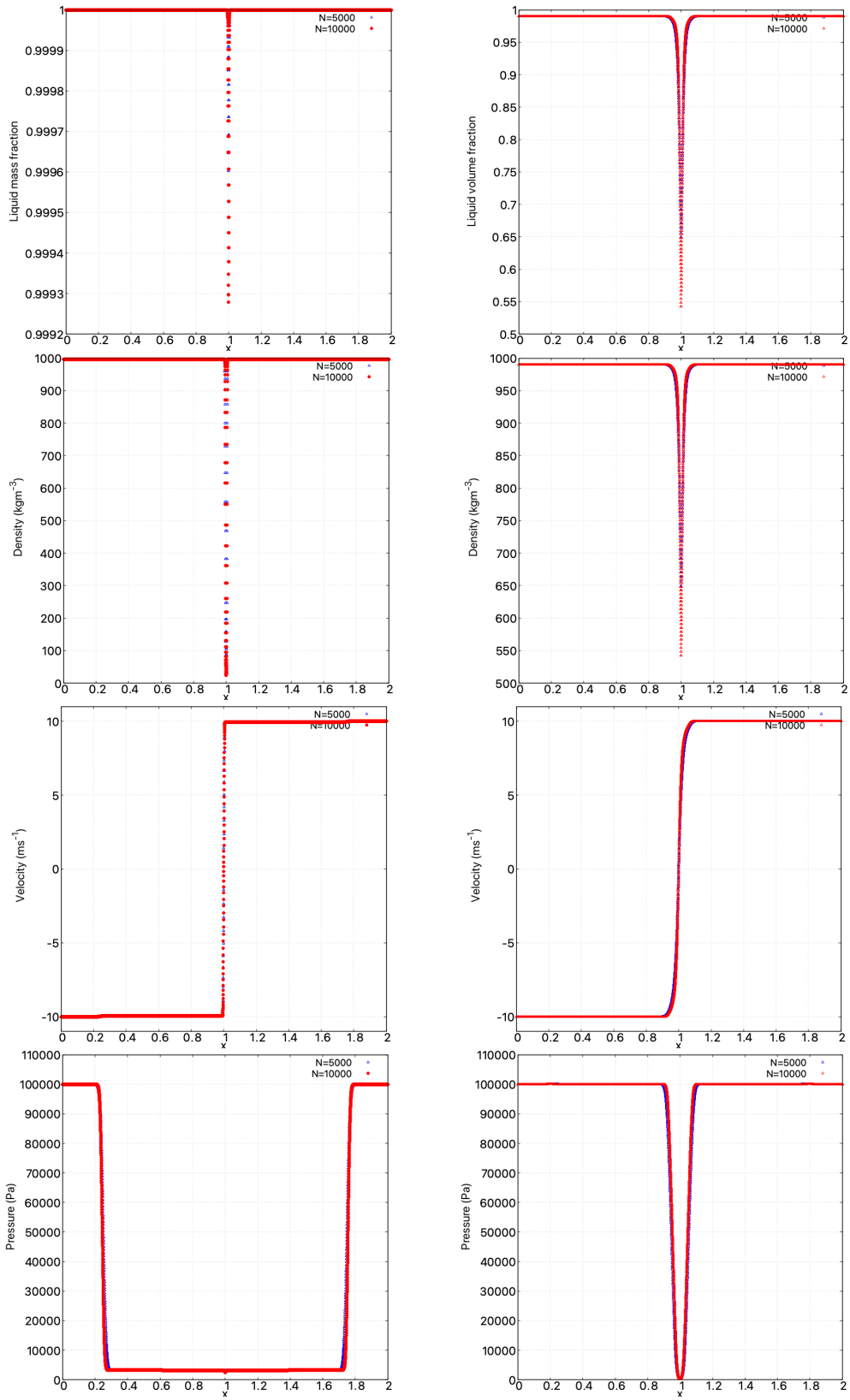

Fig. 5.12 *1D cavitation.* Plots showing expansion tube with cavitation pocket appearance using phase change model [left] and two phase model [right] at time $t = 0.5ms$.

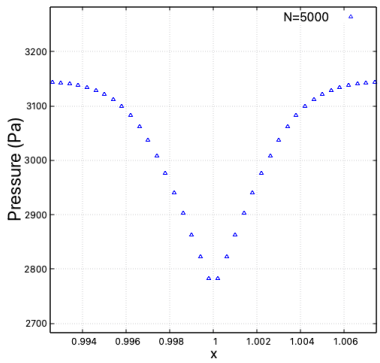

Fig. 5.13 *1D cavitation.* Extraction taken from pressure plot for phase change model

As the physics governing phase change behaviour is encoded within the water EOS, the five equations multi-material model integrated with the phase change model essentially simplifies to the conventional Euler equations modelling single material. Where cavitation occurs, the tabulated EOS for water using IAPWS is adopted; where cavitation do not occur, respective stiffened gas EOS for liquid or vapour water is selected. Figure 5.13 shows the middle part of the simulation domain which has a pressure lesser than the vapour pressure of $p = 3142Pa$. In these regions, cavitation is happening, and the material is being treated as a mixture of liquid and vapour water with certain quality. As seen in the plots on the left side of Figure 5.12, there is a sharp drop in liquid mass fraction and density at the same region as the pressure drop observed in Figure 5.13.

In contrast to the phase change model which assumes homogeneous and barotropic flow, the two phase model evolves the pressures for liquid and vapour water separately. The two phase model proposed by Saurel et al. [56] adopts a relaxation step after the hyperbolic Godunov update to enforce the six equations model converge to five equations, enabling the model to simulate cavitation. As shown in Appendix A, the relaxation step is proven to be obeying the second law of thermodynamic which states that the entropy of a closed system will always increase. Given the relaxation stage is applied to every cell within the simulation domain, cavitation behaviour is observed as long as there is a pressure drop regardless of the material's vapour pressure. The **two phase model will be used for the rest of this project** as the same EOS can be used to close the system evolving multi-material but differing EOS is needed for separate materials when the phase change model is adopted.

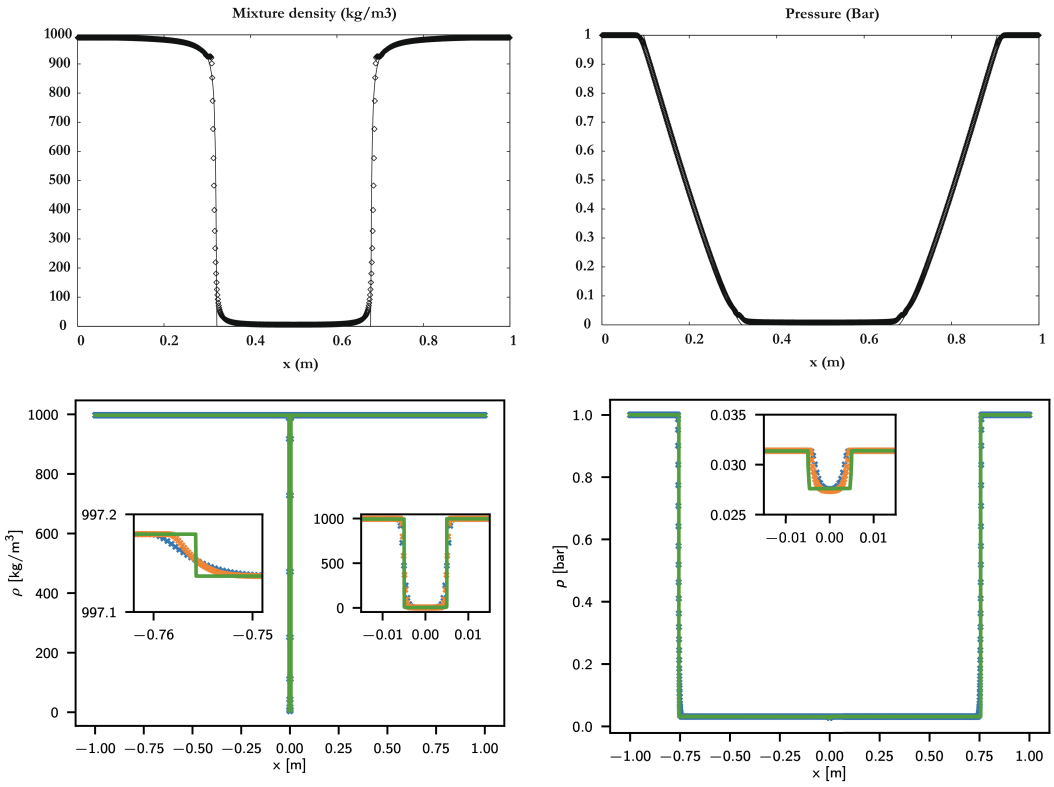

Fig. 5.14 *1D cavitation.* Top: Plots showing density and pressure results taken from Saurel et al. [56] with 100 m/s initial velocity. Bottom: Plots showing density and pressure results taken from Wilkinson et al. [63] papers with 10 m/s initial velocity.

5.3.3 Richtmyer-Meshkov Instability (RMI) Test

RMI arises when a shock wave interacts with any interface separating two fluids having different properties. The initial perturbation at the interface will be amplified by the refraction of the shock, causing more distortion and secondary instabilities such as Kelvin Helmholtz [6].

To test the multidimensional model's capability in illustrating cavitation, a 2-D test involving RMI is performed. The initial set up for this test is shown in Figure 5.15 where the left part of the domain is filled with nearly pure water ($\alpha_1 = 1 - 10^{-6}$) and the right part with nearly pure gas ($\alpha_1 = 10^{-6}$) separated by a curved interface. The interface is part of a full circle with $0.6m$ radius centred at $x = 1.2m, y = 0.5m$. The numerical domain for this test is $3m$ long and $1m$ high. Top, bottom and left boundaries are treated as solid walls while the right wall is set to be transmissive. The simulation is done on $N = 900 \times 400$ cells with $C_{cfl} = 0.3$ and results are shown in Figure 5.15. The material properties and their respective stiffened gas EOS parameters are as follows

$$\begin{aligned} &\rho_1 = 1000\text{kg/m}^3, && \rho_2 = 100\text{kg/m}^3, \\ &\gamma_1 = 4.4, && \gamma_2 = 1.8, \\ &p_{\infty,1} = 6 \times 10^8 Pa, && p_{\infty,2} = 0. \end{aligned} \tag{5.4}$$

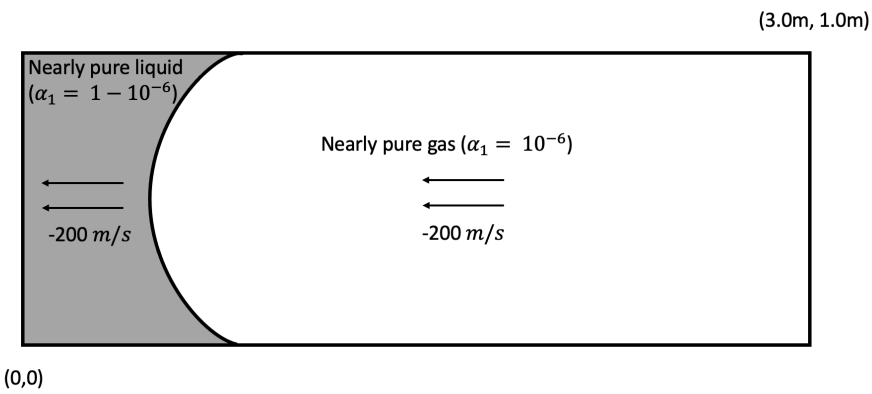

Fig. 5.15 Initial configuration of the Richtmyer-Meshkov instability test. Both liquid and gas are moving to the left at $-200m/s$.

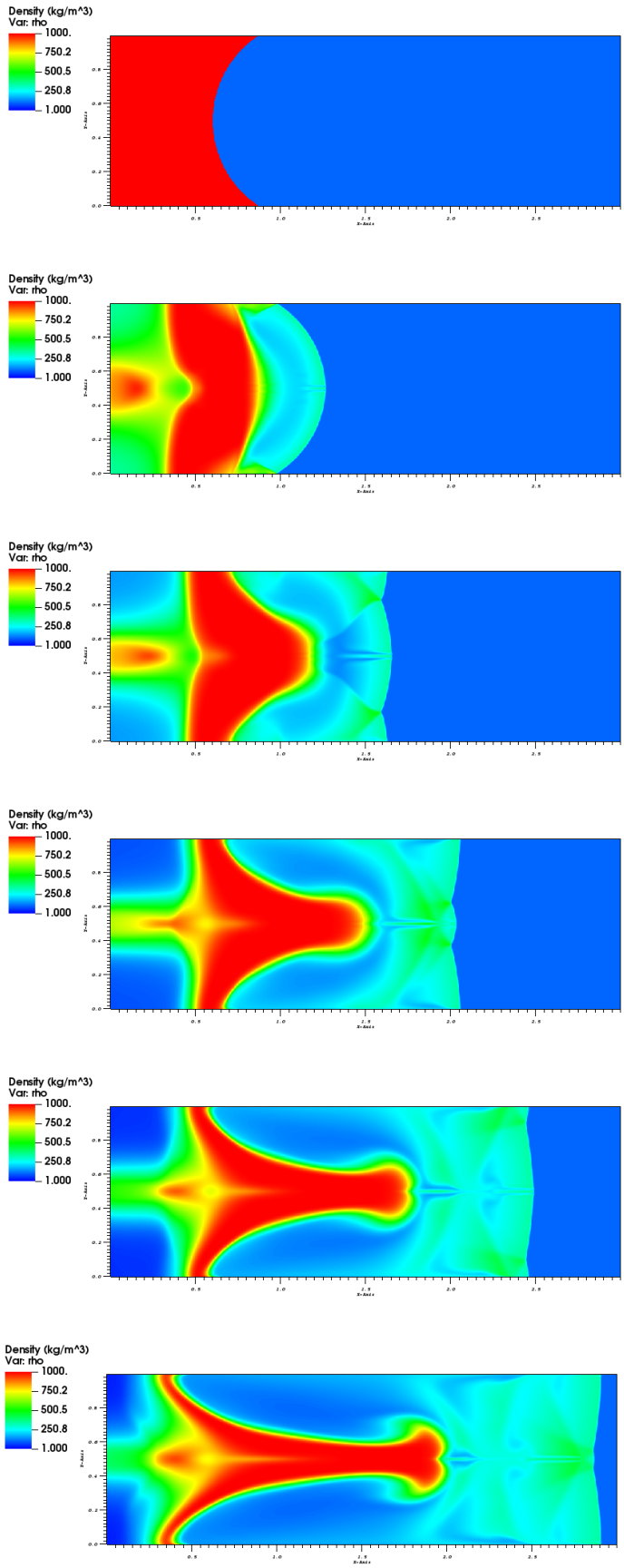

Fig. 5.16 *Water-gas Richtmyer-Meshkov instability.* Mixture density plots are shown at time t=0ms, 1.7ms, 3.1ms, 4.8ms, 6.7ms, 8.6ms.

As flow hits the left wall, a right moving shock propagates through the water-gas interface and the conventional RMI appears. As the jet elongates, new interfaces are formed dynamically near the solid wall as the expansion waves focus. Given the pressure is very low in these areas, cavitation occurs and various gas pockets are produced as illustrated at $t = 4.8ms, 6.7ms, 8.6ms$. These pockets modify the jet and spike shape with time, producing results which are comparable to the outcome of Saurel et al. [56] in Figure 5.17.

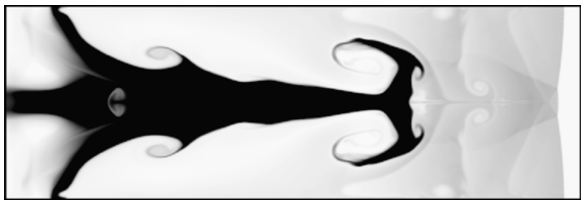

Fig. 5.17 Density plot taken from Saurel et al. [56] paper at $t = 8.6ms$.

5.3.4 Liquid Droplet Impacting a Wall Test

In this test case proposed by Niu [43], 2-D liquid droplet impingement on a wall is being analysed. This test case is performed given the similarity in settings compared to water droplet impacting a plane's body during in-flight condition. The initial set up consists of a single water droplet with radius $3.2mm$ moving horizontally through the atmosphere towards a solid wall that is $5.0mm$ apart from the centre of the water droplet. Water having density of $\rho_1 = 1000kg/m^3$ is initiated inside the circle ($\alpha_1 = 1 - 10^{-6}$) while the rest of the domain is initiated with air ($\rho_2 = 1kg/m^3, \alpha_1 = 10^{-6}$). The initial horizontal velocity of the liquid droplet is being set at $134m/s$ and the whole domain has the same pressure of $1.1 \times 10^5 Pa$. Slip boundary condition is applied to the wall by assuming negligible surface tension and viscosity effect. The simulation is carried out at $N = 400 \times 800$ cells with $C_{cfl} = 0.3$ and results are shown in Figure 5.19, 5.20.

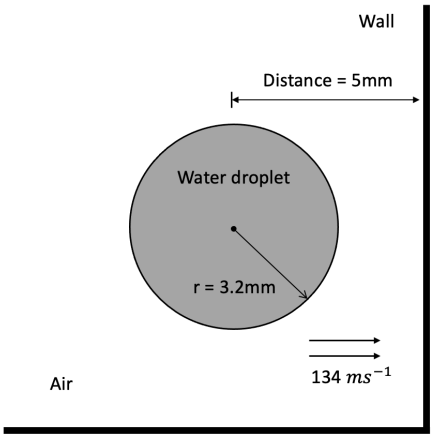

Fig. 5.18 Initial configuration of the liquid droplet impacting a wall test.

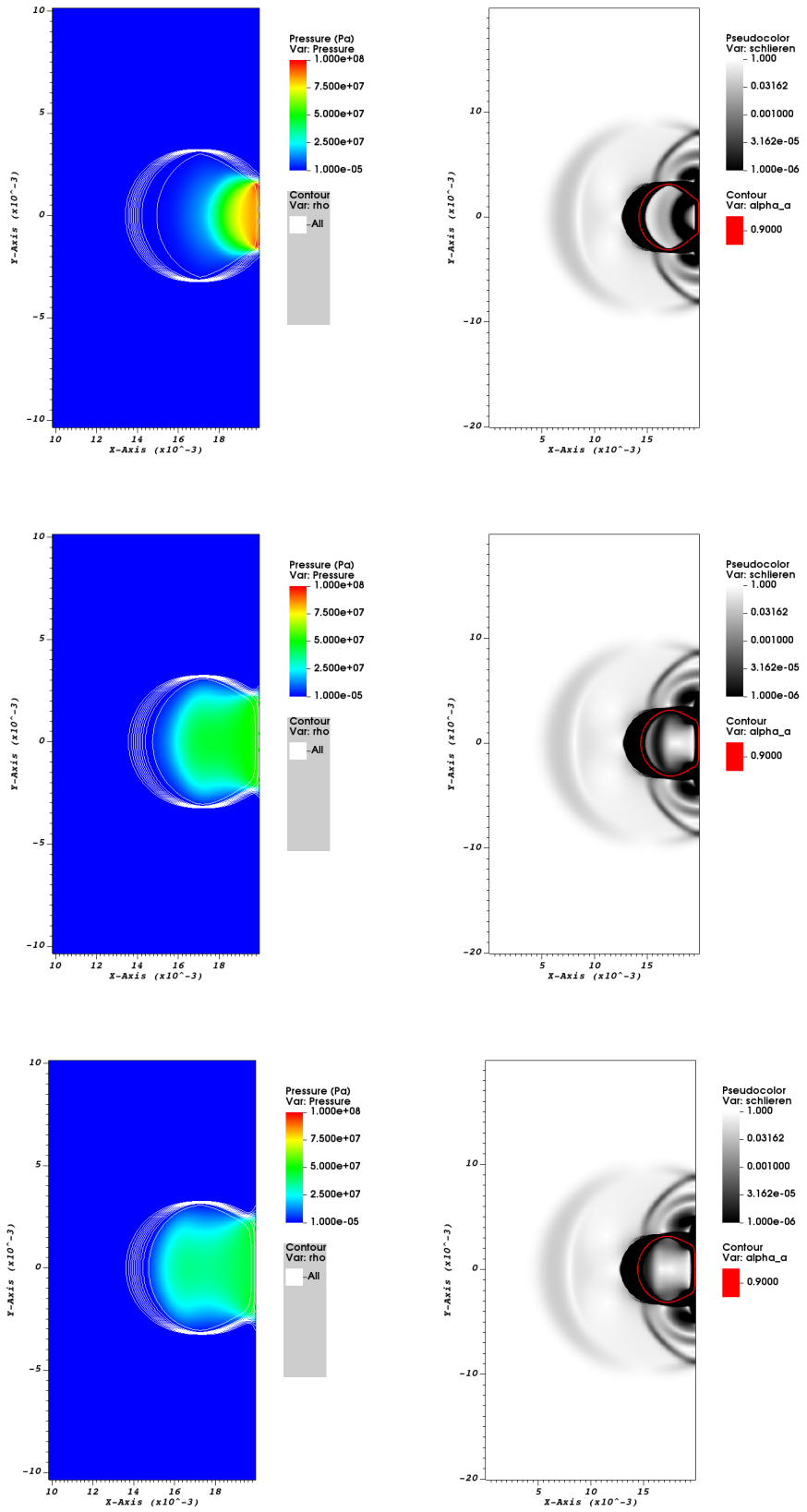

Fig. 5.19 *Liquid droplet impacting a wall.* The images show the pressure plots superimposed with density contours on the left and mock schlieren of the density on the right. The images are taken at time $t = 15.0\mu s, 16.3\mu s, 16.7\mu s$.

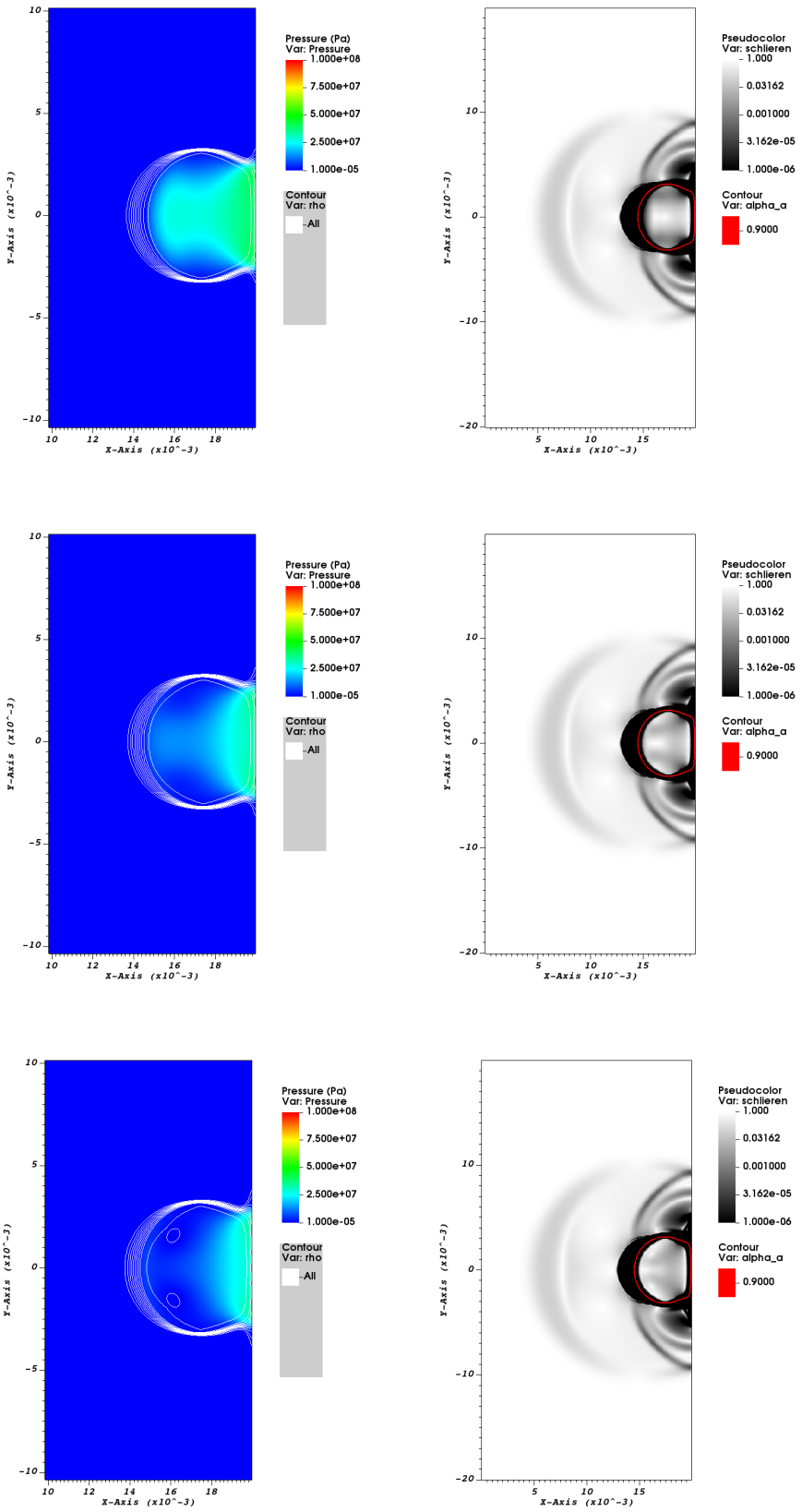

Fig. 5.20 *Liquid droplet impacting a wall.* The images show the pressure plots superimposed with density contours on the left and mock schlieren of the density on the right. The images are taken at time $t = 17.0\mu s, 17.5\mu s, 17.8\mu s$.

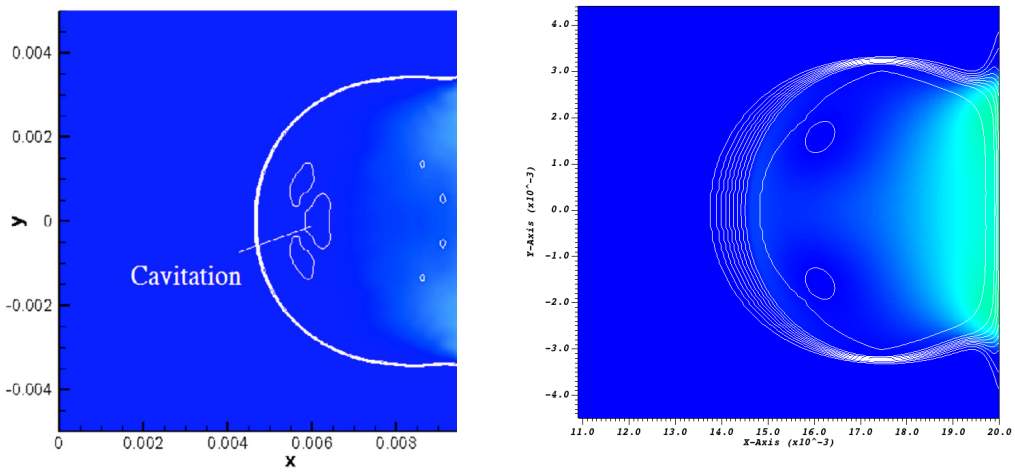

Fig. 5.21 *Liquid droplet impacting a wall.* Left: Pressure plot as $t = 14.4\mu s$ taken from Niu [43] paper. Right: Pressure plot as $t = 17.8\mu s$ produced using Saurel et al.'s model.

Immediately upon impact, creation of a strong shock wave attached to the contact edge of the droplet is observed. The liquid zone adjacent to the wall is highly compressed and separated from the bulk of the liquid by the shock envelope. Pressure difference at the contact region triggers the eruption of intense lateral jetting of high velocity. As observed at $t = 15.0\mu s$, the shock wave generated is reflected back to the bulk as an expansion wave. The wave propagating outwards reaches the upmost point where it is reflected downward, creating a low pressure area focusing at the droplet axis of symmetry. Due to the sudden drop in pressure, cavitation has been observed along the axis of symmetry at the plot taken at $t = 17.8\mu s$ [43]. Referring to Figure 5.21, this phenomenon is also observed in the test performed by Niu [43] at $t = 14.4\mu s$. It is worth mentioning that Niu adopted a different numerical solver (AUSMD type primitive variable Riemann solver) hence Figure 5.21 is not a like for like comparison to the results produced in this dissertation.

The test case is slightly modified and extended to 2-D revolutions using operator splitting discussed in Section 4.1.6 to better illustrate the physical behaviour happening within the droplet. A liquid droplet of size $100\mu m$ travelling initially at $200m/s$ downwards is simulated. As shown in Figure 5.22, similar pressure phenomena is observed after the droplet impacted the wall.

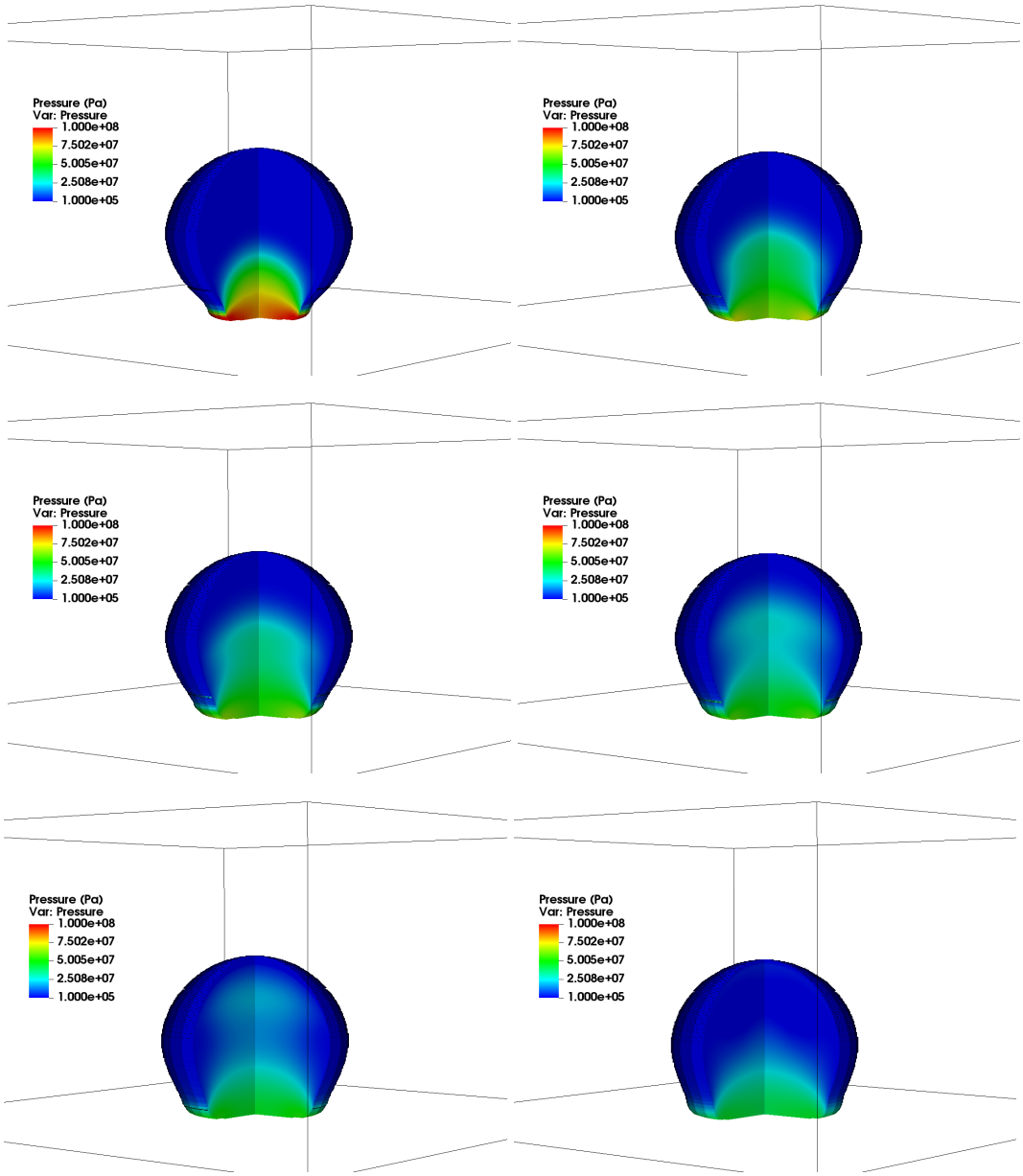

Fig. 5.22 *Liquid droplet impacting a wall.* The images show the 2-D revolutions of pressure plots of the droplet with initial velocity $200m/s$ impacting a wall. The images are taken at time $t = 0.29\mu s, 0.31\mu s, 0.32\mu s, 0.34\mu s, 0.35\mu s, 0.37\mu s$.

5.3.5 Ultrasonic Excitation Induced Cavitation Test

In this test case, ultrasonic vibration is introduced through the Boundary Condition (BC) of the bottom wall, replicating the effect of a transducer installed underneath the plane wing. The test is initialised with a water droplet positioned at $x = 0.65mm, y = 0$ surrounded by air over a simulation domain of $x \in \{0, 0.8mm\}, y \in \{-0.4mm, 0.4mm\}$. The impact of the $100\mu m$ radius droplet moving with initial velocity $100 - 200m/s$ towards a solid wall are examined.

The velocity profile in Equation (3.60) is introduced as an external Dirichlet BC. It is worth noting that the final BC applied is a combination of Dirichlet and reflective BCs. The transducer's radius is set to be $2mm$ to ensure the whole impacted area is covered.

For supercooled water droplets, freezing is typically made up of 3 stages: recalescence, complete freezing and cooling [18]. Of these, recalescence was found to be the happening at the shortest timescale as

$$t_{\text{nuc}} \propto \frac{r}{v_{\text{front}}} = \mathscr{O}\left(10^{-5}\right) \text{s to } \mathscr{O}\left(10^{-4}\right) \text{s} \tag{5.5}$$

for droplets with radii between $10 - 100\mu m$. The equation for computing the timescale is taken from the work of Prestipino [53] and v_{front} is an estimated value from the studies of recalescence images ([5], [26], [48], [59]) performed during the Boeing project [37]. This suggests that in order to prevent ice formation of the droplet, the anti-icing mechanism needs to be functioning at a similar timescale. In this dissertation, test cases with frequencies between $f = 5 - 6MHz$ and vibration amplitude of $A = 5\mu m$ are carried out and presented as follows. The simulations are carried out with cell resolution $N = 400 \times 400$ until a stop time of $t = 2\mu s$. For all the second order simulations, Van Leer is used as the slope limiter and $C_{cfl} < 0.05$ is needed to produce stable results.

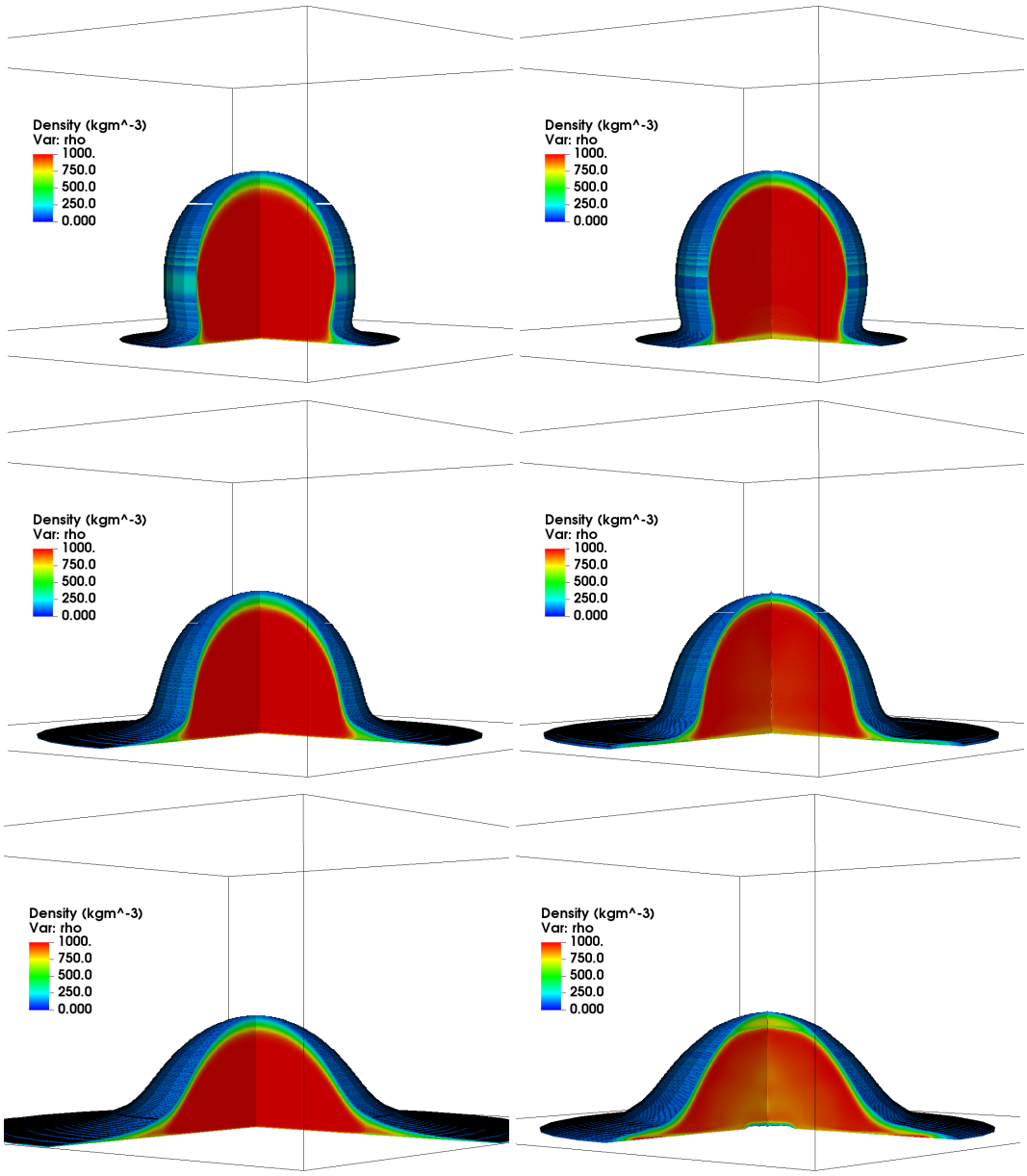

Fig. 5.23 *Liquid droplet impacting a wall with ultrasonic transducer underneath.* The images show the 2-D revolutions density plots. On the left, the plots are showing a droplet with initial velocity $200m/s$ impacting a wall while on the right, plots of the same droplet impacting a wall with an ultrasonic transducer installed underneath $(f = 5MHz, A = 5\mu m)$ are shown.The images are taken at time $t = 0.40\mu s, 0.55\mu s, 0.73\mu s$.

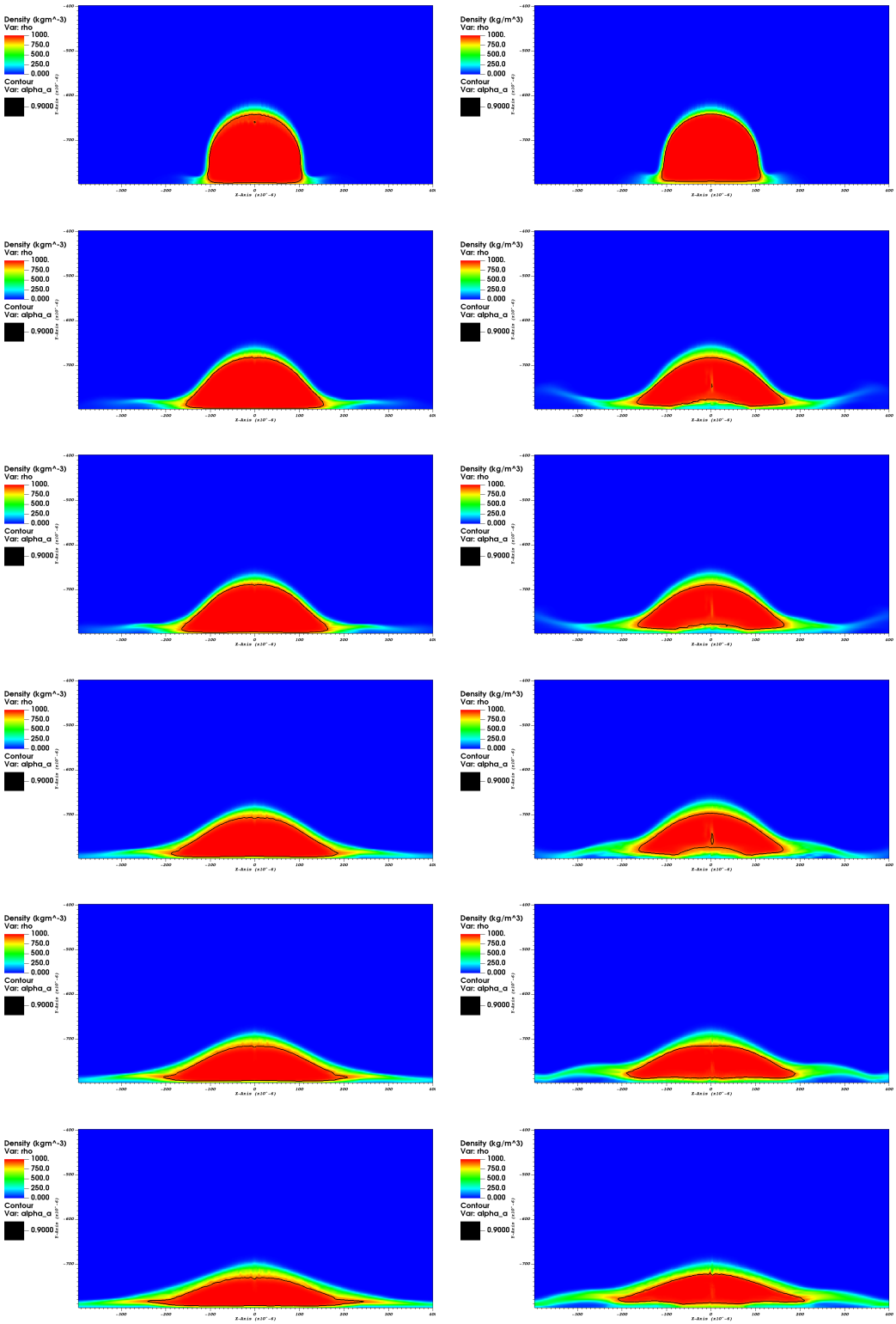

Fig. 5.24 *Liquid droplet impacting a wall with ultrasonic transducer underneath.* The images show the density plots superimposed with liquid volume fraction contours. On the left, the plots are showing a droplet with initial velocity $200m/s$ impacting a wall. On the right, plots of the same droplet impacting a wall with an ultrasonic transducer installed underneath $(f = 6MHz, A = 5\mu m)$ are shown. The images are taken at time $t = 0.43\mu s, 0.70\mu s, 0.76\mu s, 0.90\mu s, 1.0\mu s, 1.19\mu s$.

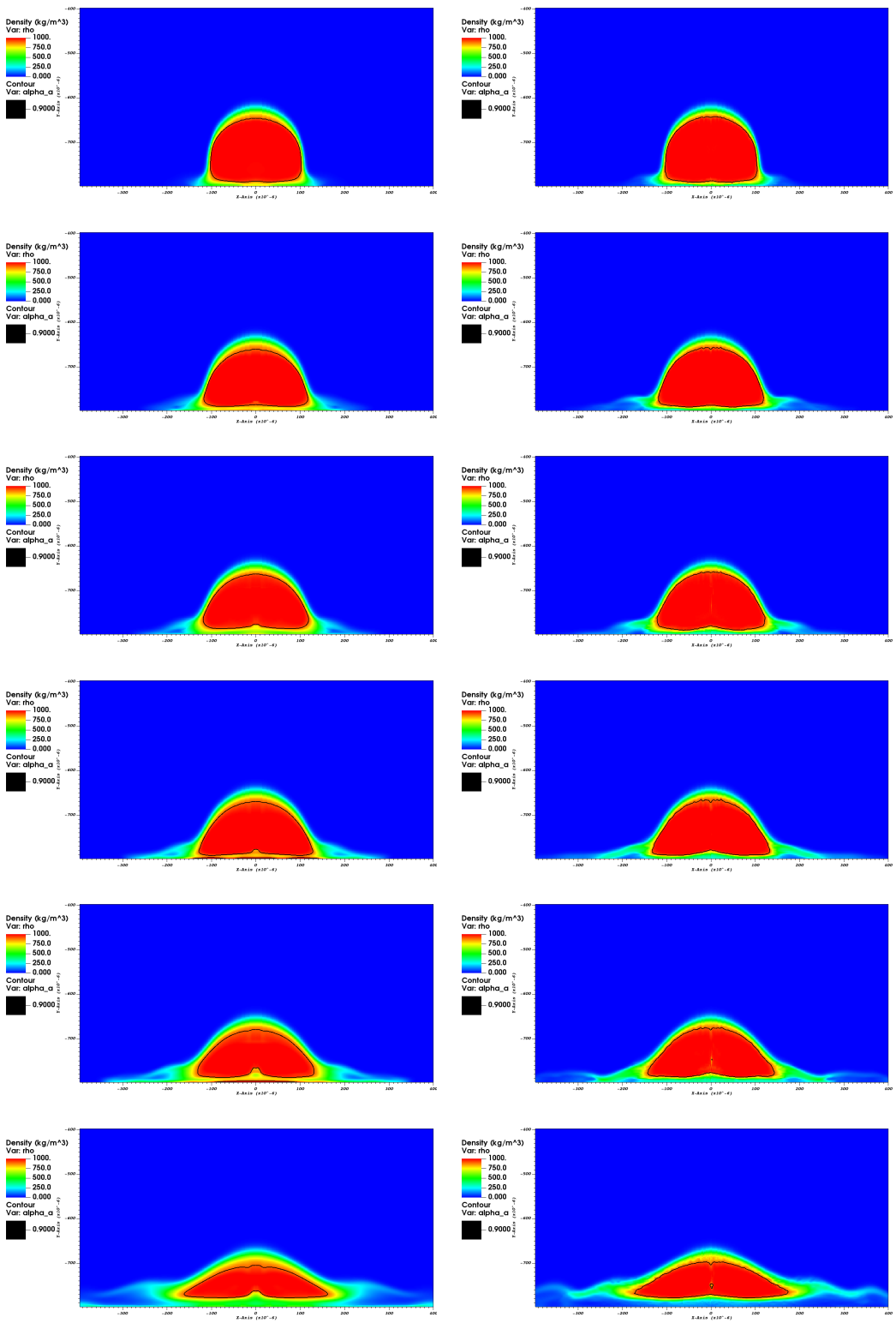

Fig. 5.25 *Liquid droplet impacting a wall with ultrasonic transducer underneath.* The images show the density plots superimposed with liquid volume fraction contours. On the left, first order accurate plots are showing the droplet with initial velocity $100m/s$ impacting a wall with an ultrasonic transducer installed underneath $(f = 6MHz, A = 5\mu m)$. On the right, second order accurate plots are shown. The images are taken at time $t = 0.81\mu s, 0.98\mu s, 1.06\mu s, 1.14\mu s, 1.32\mu s, 1.82\mu s$.

When the liquid droplet impacted a normal surface at high speed, the droplet deposited on the surface as shown in the left plots of Figure 5.23. As observed in the right plots of Figure 5.23, when the transducers underneath the substrate is working, cavitation is induced between the droplet and substrate, resulting in a layer of water vapour. The oscillatory vibrations introduced by the transducers resulted in large expansion waves being passed into the water droplet when the transducer is moving "into the wall". These waves resulted in a low pressure region at the droplet-substrate interface which then leads to cavitation. The effect of ultrasonic vibration can also be seen in Figure 5.24 as cavitation behaviour is observed at the interface on the right plots. It is worth noting the difference in cavitation behaviour observed in the 2-D and 2-D revolutions as the vibration frequencies used differ (At the same simulation time, more cavitation at higher frequency).

The same test is repeated but with liquid droplet initial velocity being set at $100m/s$. Cavitation behaviour at the interface is successfully demonstrated in Figure 5.25 and this proves the validity of our model for velocity range between $100-200m/s$. First order and second order results are produced for comparison purpose here. As expected, the first order results are more stable and diffusive while the second order results are better at displaying details of the behaviours. The reason behind stability issue in the second order simulations is not known and being considered as future work.

Chapter 6

Conclusion

In this dissertation we implemented a second order multi-material, multiphase model capable of simulating systems containing more than single material and phase change behaviour. The model is proven to be robust from a series of test cases involving different materials under a wide range of operating conditions. Additionally, the theory surrounding ultrasonic excitation induced cavitation within the water droplet is validated for the initial droplet velocity range of $100-200m/s$.

For comparison purpose, both the cavitation models (two phase model and phase change model) discussed in this dissertation are coded and tested using the 1-D cavitation test. As the two phase model assumes the interfaces between the two phases as numerically diffused zones, cavitation behaviours displayed in the simulation results are more diffusive. On the other hand, the phase change model is capable of producing simulations with sharper features as the liquid-vapour interfaces are not numerically smeared. The sharp features are also shown in the work of ([4], [25], [63]) which adopt the phase change model. However, the phase change model requires complete EOS to close the system of equations hence introducing extra computational load to the simulation. In contrast, incomplete EOS can be used in two phase model and complex root finding algorithm can be avoided here. However, the extra computational cost is not a concern for materials being described using stiffened gas EOS but more of a concern for materials with complex EOS such as Mie-Gruneisen EOS and Jones-Wilkins-Lee (JWL) EOS.

The test results for the case of liquid droplet impacting a wall with ultrasonic transducers installed underneath validated the hypothesis made in the Boeing project. The model used here is second order accurate and quasi-conservative, which is something new to the Boeing project. Induced cavitation by lowering the pressure at the droplet-substrate interface is the

reason behind why the supercooled droplet is not freezing. The range of frequencies predicted have successfully introduced cavitation before the liquid droplet stay on the substrate long enough to freeze. The next stage for the project is for Boeing to run some practical experiments to validate the simulation results produced. Once the results are validated, more numerical tests and experiments can be performed with varying parameters including vibration frequencies, number of transducers and transducers configuration. These parameters are essential to determine the energy requirement for this anti-icing technology which can then form the basis for comparison with current anti-icing technologies' energy consumption.

Moving forward, more development work should be done on the phase change model, so the studies on ultrasonic excited droplets can be extended to include another cavitation model. The difference in efficiency between the two cavitation models is a subject of interest given the phase change model only evolves a single set of PDEs but requires complicated algorithm in defining the EOS while the two phase model evolves a separate set of PDEs for liquid and vapour. Besides that, AMR is difficult to implement for Saurel et al.'s model due to the non-conservative behaviour and presence of source terms, but we are hoping to adopt this technique in the future with Wilkinson et al.'s model as demonstrated by the authors. Furthermore, higher order simulations can be attained using the WENO scheme [33]. In addition, the simulation can be extended to 3-D using the similar approach of developing 2-D simulations from 1-D so further studies can be done on different configurations (e.g. droplet impacting the side of the transducer). Another piece of identified future work is to incorporate the cavitation model with an elastoplastic model to take into account waves propagating through the aircraft skin prior reaching the droplet.

References

[1] Allaire, G., Clerc, S., and Kokh, S. (2002). A five-equation model for the simulation of interfaces between compressible fluids. *Journal of Computational Physics*, 181:577–616.

[2] Anderson, J. (2017). Fundamentals of aerodynamics.

[3] Baer, M. R. and Nunziato, J. W. (1986). A two-phase mixture theory for the deflagration-to-detonation transition (ddt) in reactive granular materials.

[4] Barberon, T. and Helluy, P. (2006). Finite volume simulation of cavitating flows.

[5] Bauerecker, S., Ulbig, P., Buch, V., Vrbka, L., and Jungwirth, P. (2008). Monitoring ice nucleation in pure and salty water via high-speed imaging and computer simulations. *Journal of Physical Chemistry C*, 112:7631–7636.

[6] Brouillette, M. (2002). The richtmyer-meshkov instability. *Annual review of fluid mechanics*, 34:445.

[7] Bruce Stewart, H. and Wendroff, B. (1984). Two-phase flow: Models and methods. *Journal of Computational Physics*, 56(3):363–409.

[8] Cimpeanu, R. and Papageorgiou, D. T. (2018). Three-dimensional high speed drop impact onto solid surfaces at arbitrary angles. *International Journal of Multiphase Flow*, 107:192–207.

[9] Daramizadeh, A. and Ansari, M. R. (2015). Numerical simulation of underwater explosion near air-water free surface using a five-equation reduced model. *Ocean Engineering*, 110:25–35.

[10] Davis, S. F. (1988). Simplified second-order godunov-type methods. *SIAM Journal on Scientific and Statistical Computing*, 9(3):445–473.

[11] Dervieux, A. and Thomasset, F. (1980). A finite element method for the simulation of a rayleigh-taylor instability.

[12] Drew, D. A. and Passman, S. L. (1998). Theory of multicomponent fluids.

[13] Dumbser, M., Iben, U., and Munz, C. D. (2013). Efficient implementation of high order unstructured weno schemes for cavitating flows. *Computers and Fluids*, 86:141–168.

[14] Faccanoni, G., Allaire, G., and Kokh, S. (2009). Mathematical problems in mechanics approximation of liquid-vapor phase transition for compressible fluids with tabulated eos.

[15] Faccanoni, G., Kokh, S., and Allaire, G. (2008). Numerical simulation with finite volume of dynamic liquid-vapor phase transition.

[16] Faccanoni, G., Kokh, S., and Allaire, G. (2012). Modelling and simulation of liquid-vapor phase transition in compressible flows based on thermodynamical equilibrium. *ESAIM: Mathematical Modelling and Numerical Analysis*, 46:1029–1054.

[17] Fedkiw, R. P., Aslam, T., Merriman, B., and Osher, S. (1999). A non-oscillatory eulerian approach to interfaces in multimaterial flows (the ghost fluid method).

[18] Feuillebois, F., Lasek, A., Creismeas, P., Pigeonneau, F., and Szaniawski, A. (1995). Freezing of a subcooled liquid droplet. *Journal of Colloid and Interface Science*, 169(1):90–102.

[19] F.R.S., L. R. O. (1917). Viii. on the pressure developed in a liquid during the collapse of a spherical cavity. *The London, Edinburgh, and Dublin Philosophical Magazine and Journal of Science*, 34(200):94–98.

[20] Gent, R. W., Dart, N. P., and Cansdale, J. T. (2000). Aircraft icing. *Philosophical Transactions of the Royal Society A: Mathematical, Physical and Engineering Sciences*, 358:2873–2911.

[21] Gilmore, F. R. (1952). The growth or collapse of a spherical bubble in a viscous compressible liquid.

[22] Harlow, F. I. and ivisden, A. A. A. (1971). A numerical fluid dynamics calculation method for all flow speeds.

[23] Harten, A., Lax, P. D., and Leer, B. v. (1983). On upstream differencing and godunov-type schemes for hyperbolic conservation laws. *SIAM Review*, 25(1):35–61.

[24] Hu, X. Y. and Khoo, B. C. (2009). An interface interaction method for compressible multifluids.

[25] Jin, Z., Yin, C., Chen, Y., Cui, Y. D., Khoo, B. C., Jiao, S., and Hua, H. (2021). Study on the cavitation effects induced by the interaction between underwater blast and various boundaries. *Ocean Engineering*, 222.

[26] Jung, S., Tiwari, M. K., Doan, N. V., and Poulikakos, D. (2012). Mechanism of supercooled droplet freezing on surfaces. *Nature Communications*, 3.

[27] Kapila, A. K., Menikoff, R., Bdzil, J. B., Son, S. F., and Stewart, D. S. (2001). Two-phase modeling of deflagration-to-detonation transition in granular materials: Reduced equations. *Physics of Fluids*, 13:3002–3024.

[28] Kundu, P. K., Cohen, I. M., and Dowling, D. R., editors (2012). *Chapter 5 - Vorticity Dynamics*. Academic Press, Boston, fifth edition edition.

[29] Layes, G. and Métayer, O. L. (2007). Quantitative numerical and experimental studies of the shock accelerated heterogeneous bubbles motion. *Physics of Fluids*, 19.

[30] Leveque, R. J. (1992). *Numerical Methods for Conservation Laws*. Birkhäuser.

[31] Liu, T. G., Khoo, B. C., and Xie, W. F. (2004). Isentropic one-fluid modelling of unsteady cavitating flow. *Journal of Computational Physics*, 201:80–108.

[32] Liu, T. G., Khoo, B. C., and Yeo, K. S. (2003). Ghost fluid method for strong shock impacting on material interface. *Journal of Computational Physics*, 190:651–681.

[33] Liu, X.-D., Osher, S., and Chan, T. (1994). Weighted essentially non-oscillatory schemes. *Journal of Computational Physics*, 115(1):200–212.

[34] Lombard, B. and Donat, R. (2005). The explicit simplified interface method for compressible multicomponent flows.

[35] Mauro, A. and Paolucci, V. S. (2012). Two-phase cavitation modelling fully compressible formulation daniele liuzzi.

[36] Menikoff, R. and Plohr, B. J. (1988). The riemann problem for fluid flow of real materials.

[37] Millmore, S. (2016). Ultra-sonic anti-icing models.

[38] Millmore, S. (2021a). Lecture notes in computational continuum modelling.

[39] Millmore, S. (2021b). Lecture notes in computational multiphysics.

[40] Mulder, W., Osher+, S., and Sethian, J. A. (1992). Computing interface motion in compressible gas dynamics.

[41] Murrone, A. and Guillard, H. (2005). A five equation reduced model for compressible two phase flow problems. *Journal of Computational Physics*, 202:664–698.

[42] Métayer, O. L., Massoni, J., and Saurel, R. (2004). Élaboration des lois d'état d'un liquide et de sa vapeur pour les modèles d'écoulements diphasiques. *International Journal of Thermal Sciences*, 43:265–276.

[43] Niu, Y. Y. (2016). Computations of two-fluid models based on a simple and robust hybrid primitive variable riemann solver with ausmd. *Journal of Computational Physics*, 308:389–410.

[44] Osher, S. and Fedkiw, R. P. (2001). Level set methods: An overview and some recent results. *Journal of Computational Physics*, 169:463–502.

[45] Palacios, J., Palacios, J. L., Rose, J. L., and Morrow, P. (2008). Investigation of an ultrasonic ice protection system for helicopter rotor blades.

[46] Palacios, J., Smith, E., Rose, J., and Royer, R. (2011). Ultrasonic de-icing of wind-tunnel impact icing. *Journal of Aircraft*, 48:1020–1027.

[47] Park, J. (2008). *A Coupled Runge Kutta Discontinuous Galerkin-Direct Ghost Fluid (RKDG-DGF) Method to Near-field Early-time Underwater Explosion (UNDEX) Simulations*. PhD thesis.

[48] Pasieka, J., Nanua, R., Coulombe, S., and Servio, P. (2014). The crystallization of sub-cooled water: Measuring the front velocity and mushy zone composition via thermal imaging. *International Journal of Heat and Mass Transfer*, 77:940–945.

[49] Pelanti, M. and Shyue, K. M. (2014). A mixture-energy-consistent six-equation two-phase numerical model for fluids with interfaces, cavitation and evaporation waves. *Journal of Computational Physics*, 259:331–357.

[50] Pelanti, M. and Shyue, K. M. (2019). A numerical model for multiphase liquid–vapor–gas flows with interfaces and cavitation. *International Journal of Multiphase Flow*, 113:208–230.

[51] Petitpas, F., Franquet, E., Saurel, R., and Metayer, O. L. (2007). A relaxation-projection method for compressible flows. part ii: Artificial heat exchanges for multiphase shocks. *Journal of Computational Physics*, 225:2214–2248.

[52] Plesset, M. S. and Prosperetti, A. (1977). Bubble dynamics and cavitation. *Annual Review of Fluid Mechanics*, 9(1):145–185.

[53] Prestipino, S. (2013). A maximum-entropy approach to the adiabatic freezing of a supercooled liquid. *Journal of Chemical Physics*, 138.

[54] Purvis, R. and Smith, F. T. (2005). Droplet impact on water layers: Post-impact analysis and computations. volume 363, pages 1209–1221. Royal Society.

[55] Saurel, R., Franquet, E., Daniel, E., and Metayer, O. L. (2007). A relaxation-projection method for compressible flows. part i: The numerical equation of state for the euler equations. *Journal of Computational Physics*, 223:822–845.

[56] Saurel, R., Petitpas, F., and Berry, R. A. (2008). Simple and efficient relaxation methods for interfaces separating compressible fluids, cavitating flows and shocks in multiphase mixtures. *Journal of Computational Physics*, 228:1678–1712.

[57] Schmidt, D. P., Rutland, C. J., and Corradini, M. L. (1999). A fully compressible, two-dimensional model of small, high-speed, cavitating nozzles. *Atomization and Sprays*, 9:255–276.

[58] Sethian, J. A. (2001). Evolution, implementation, and application of level set and fast marching methods for advancing fronts. *Journal of Computational Physics*, 169:503–555.

[59] Tavakoli, F., Davis, S. H., and Kavehpour, H. P. (2015). Freezing of supercooled water drops on cold solid substrates: initiation and mechanism. *Journal of Coatings Technology and Research*, 12:869–875.

[60] Toro, E. F. (2006). *Riemann solvers and numerical methods for fluid dynamics : a practical introduction*. Springer.

[61] Wagner, W. and Pruß, A. (2002). The iapws formulation 1995 for the thermodynamic properties of ordinary water substance for general and scientific use. *Journal of Physical and Chemical Reference Data*, 31:387–535.

[62] Wang, C. W., Liu, T. G., and Khoo, B. C. (2006). A real ghost fluid method for the simulation of multimedium compressible flow. *SIAM Journal on Scientific Computing*, 28:278–302.

[63] Wilkinson, S. D., Barton, P. T., and Nikiforakis, N. (in preparation). A thermal equilibrium approach to modelling multiple solid-fluid interactions with phase transitions, with application to cavitation.

[64] Wood, A. B. (1930). *A Textbook of Sound*. G. Bell and Sons Ltd.

[65] Xu, L., Feng, C., and Liu, T. (2016). Practical techniques in ghost fluid method for compressible multi-medium flows. *Communications in Computational Physics*, 20:619–659.

[66] Yin, C., Zhang, Z., Wang, Z., and Guo, H. (2016). Numerical simulation and experimental validation of ultrasonic de-icing system for wind turbine blade. *Applied Acoustics*, 114:19–26.

[67] Zein, A., Hantke, M., and Warnecke, G. (2010). Modeling phase transition for compressible two-phase flows applied to metastable liquids. *Journal of Computational Physics*, 229:2964–2998.

[68] Zhang, J. (2020). A simple and effective five-equation two-phase numerical model for liquid-vapor phase transition in cavitating flows. *International Journal of Multiphase Flow*, 132.

[69] Zhang, W., Almgren, A., Beckner, V., Bell, J., Blaschke, J., Chan, C., Day, M., Friesen, B., Gott, K., Graves, D., Katz, M., Myers, A., Nguyen, T., Nonaka, A., Rosso, M., Williams, S., and Zingale, M. (2019). Amrex: a framework for block-structured adaptive mesh refinement. *Journal of Open Source Software*, 4:1370.

[70] Zhang, Z. F., Wang, C., Wang, L. K., Zhang, A. M., and Silberschmidt, V. V. (2018). Underwater explosion of cylindrical charge near plates: Analysis of pressure characteristics and cavitation effects. *International Journal of Impact Engineering*, 121:91–105.

Appendix A

Pressure Relaxation Entropy Proof

This section shows the mathematical proof validating the pressure relaxation step within the two phase model proposed by Saurel et al. [56] actually obeys the second law of thermodynamics. The mathematical proof is extracted from Saurel et al. 2007 paper [55] on *A relaxation-projection method for compressible flows. Part I: The numerical equation of state for the Euler equations*. In this paper, the author proposed a relaxation-projection method for computing the cell pressure. The relaxation system is developed to connect the various non-equilibrium states inside the Lagrangian cell and determine the equilibrium pressure within the cell as the asymptotic solution of the relaxation system. The vector of conservative variables will be solved on a Lagrangian mesh and projected onto the Eulerian grid after.

Considering a Lagrangian cell containing two fluids carrying different properties being separated by an interface, the relaxation system can be derived from the seven equations Baer-Nunziato model and defined as follows.

$$\frac{\partial \alpha_k}{\partial t} = \frac{\delta}{Z_k}\left(p_k - p_I\right) \tag{A.1a}$$

$$\frac{\partial \alpha_k \rho_k}{\partial t} = 0 \tag{A.1b}$$

$$\frac{\partial \alpha_k \rho_k u_k}{\partial t} = \delta Z_k \left(u_I - u_k\right) \tag{A.1c}$$

$$\frac{\partial \alpha_k \rho_k E_k}{\partial t} = \delta \left(u_I Z_k \left(u_I - u_k\right) - \frac{p_I}{Z_k}\left(p_k - p_I\right)\right) \tag{A.1d}$$

with $\delta = \frac{2}{\Delta x}$, $Z_k = (\rho c)_k$, $u_I = \frac{Z_1 u_1 + Z_2 u_2}{Z_1 + Z_2}$ and $p_I = \frac{\frac{p_1}{Z_1} + \frac{p_2}{Z_2}}{\frac{1}{Z_1} + \frac{1}{Z_2}}$.

The energy equation can be written into this form

$$\frac{\partial \alpha_k \rho_k E_k}{\partial t} = -p_I \frac{\partial \alpha_k}{\partial t} + u_I \frac{\partial \alpha_k \rho_k u_k}{\partial t}. \tag{A.2}$$

Combining the energy with mass and momentum equations gives

$$\frac{\partial e_k}{\partial t} + (u_k - u_I) \frac{\partial u_k}{\partial t} + p_I \frac{\partial v_k}{\partial t} = 0. \tag{A.3}$$

Integration of the equation between the two states can be done as

$$\int_0^{+\infty} \frac{\mathrm{d}e_k(t)}{\mathrm{d}t} \mathrm{d}t + \int_0^{+\infty} (u_k(t) - u_I(t)) \frac{\mathrm{d}u_k(t)}{\mathrm{d}t} \mathrm{d}t + \int_0^{+\infty} p_I(t) \frac{\mathrm{d}v_k(t)}{\mathrm{d}t} \mathrm{d}t = 0, \tag{A.4}$$

which results in the following equation

$$e_k^* - e_k^0 + \hat{p}_{I,k} \left(v_k^* - v_k^0 \right) = \frac{1}{2} \left(u^* - u_k^0 \right) \left(2\hat{u}_{I,k} - \left(u^* + u_k^0 \right) \right), \tag{A.5}$$

where $\hat{p}_{I,k} = \frac{1}{v_k^* - v_k^0} \int_0^{+\infty} p_I \frac{\mathrm{d}v_k}{\mathrm{d}t} \mathrm{d}t$ and $\hat{u}_{I,k} = \frac{1}{u^* - u_k^0} \int_0^{+\infty} u_I \frac{\mathrm{d}u_k}{\mathrm{d}t} \mathrm{d}t$ are the averages during the relaxation process of interface pressure and velocity respectively. The pressure and velocity at relaxed state are denoted by p^* and u^* respectively. Assuming the evolution of all the variables are infinitesimal, the equation can be written as

$$\Delta e_k + (u_k - \hat{u}_I) \Delta u_k + \hat{p}_I \Delta v_k = 0. \tag{A.6}$$

By using Gibbs identity, the entropy variation can be written as

$$T_k \Delta s_k = (p_k - \hat{p}_I) \Delta v_k + (\hat{u}_I - u_k) \Delta u_k. \tag{A.7}$$

To analyse the sign of the entropy variation, Δv_k in Equation A.7 has to be expressed in a different form which aligns with the thermodynamics path

$$\left. \frac{\partial e_k}{\partial p_k} \right|_{v_k} \Delta p_k + \left(\hat{p}_I + \left. \frac{\partial e_k}{\partial v_k} \right|_{p_k} \right) \Delta v_k = (\hat{u}_I - u_k) \Delta u_k. \tag{A.8}$$

Using the relationships $\frac{\partial e_k}{\partial c_k}|_{p_k} = c_k^2/(v_k \Gamma_k) - p_k$ and $\frac{\partial e_k}{\partial p_k}|_{v_k} = v_k/\Gamma_k$, the following equation can be obtained

$$\Delta v_k = \frac{(\hat{u}_I - u_k) \Delta u_k - \frac{v_k}{\Gamma_k} \Delta p_k}{\left(\hat{p}_I - p_k + \frac{c_k^2}{v_k \Gamma_k} \right)}, \tag{A.9}$$

where Γ_k is the Grüneisen coefficient. By inserting this result into Equation A.7, we obtain

$$T_k \Delta s_k = \frac{v_k}{\Gamma_k} \frac{\frac{c_k^2}{v_k^2} (\hat{u}_I - u_k) \Delta u_k - (p_k - \hat{p}_I) \Delta p_k}{\left(\hat{p}_I - p_k + \frac{c_k^2}{v_k \Gamma_k}\right)}. \tag{A.10}$$

The definition of polytropic coefficient $\left(\gamma_k = \frac{\rho_k c_k^2}{p_k}\right)$ can be used to rewrite the equation into

$$T_k \Delta s_k = \frac{\gamma_k}{\Gamma_k} \frac{Z_k^2 (\hat{u}_I - u_k) \Delta u_k - (p_k - \hat{p}_I) \Delta p_k}{\left(\hat{Z}_{I,k}^2 + Z_k^2 \left(\frac{\gamma_k}{\Gamma_k} - 1\right)\right)} \tag{A.11}$$

with $Z_k = \rho_k c_k$ and $\hat{c}_{I,k}^2 = \gamma_k \hat{p}_I v_k$. Integration of this equation between state '0' and '*' leads to

$$T_k^0 \left(s_k^* - s_k^0\right) = \frac{1}{2} \frac{\gamma_k}{\Gamma_k} \frac{Z_k^{0^2} \left(u^* - u_k^0\right) \left(2\hat{u}_I - \left(u^* + u_k^0\right)\right) + \left(p^* - p_k^0\right) \left(2\hat{p}_I - \left(p^* + p_k^0\right)\right)}{\left(\hat{Z}_{I,k}^2 + Z_k^{0^2} \left(\frac{\gamma_k}{T_k} - 1\right)\right)}. \tag{A.12}$$

This relation can then be used to evaluate the entropy inequality. It can be deduced that under the conditions of $\hat{p}_I = p^*$ and $\hat{u}_I = u^*$, the relation $\left(s_k^* - s_k^0\right) > 0$ is obeyed, hence concluding the relaxation step is obeying the second law of thermodynamics.

Appendix B

Pseudocode for Phase Change Model

Algorithm 1 Variable conversion of pressure to energy

$getEos$ ←This is a function performing interpolation on tabulated EOS data.
$getMixtureEnergy$ ←This is a function for computing the total mixture energy using mass fraction and specific internal energies for both liquid and vapour phases.
$getEnergy$ ←This is a function for computing the total energy using either the specific internal energy for liquid or vapour state of the material.

P_{min} ← Minimum pressure on material's saturation dome
P_{max} ← Maximum pressure on material's saturation dome
v ← Specific volume (1/density)
vl^* ← Specific volume corresponding to the saturated liquid state
vg^* ← Specific volume corresponding to the saturated vapour state
$liquid/vapourconst$ ← Material specific constants including gamma, reference pressure and reference energy

if $P_{min} < Pressure < P_{max}$ **then**
  $vl^* \leftarrow getEos(pressure)$
  $vg^* \leftarrow getEos(pressure)$
  if $vl^* < v < vg^*$ **then**
    $Energy \leftarrow getMixtureEnergy(massfraction, vl^*, vg^*)$
  else
    $Energy \leftarrow getEnergy(v, pressure, liquidconst, vapourconst)$
  end if
else
  $Energy \leftarrow getEnergy(v, pressure, liquidconst, vapourconst)$
end if

Algorithm 2 Variable conversion of energy to pressure

$getEos$ ←This is a function performing interpolation on tabulated EOS data.
$getIE$ ←This is a function for computing the specific internal energy using the stiffened gas equation of state.
$bisectionsearch$ ←This is a function for computing the pressure which gives the equivalent specific internal energy computed from total energy.
$getPressure$ ←This is a function for computing the pressure using either the pressure for liquid or vapour state of the material.

P_{min} ← Minimum pressure on material's saturation dome
P_{max} ← Maximum pressure on material's saturation dome
v ← Specific volume (1/density)
v_c ← Specific volume corresponding to the critical point of material
vl^*_{min} ← Specific volume corresponding to the saturated liquid state at triple point
vg^*_{max} ← Specific volume corresponding to the saturated vapour state at triple point
$IEreal$ ← Specific internal energy computed from the total energy variable
$IEsaturated$ ← Specific internal energy computed using the saturated pressure
$liquid/vapourconst$ ← Material specific constants including gamma, reference pressure and reference energy.

if $vl^*_{min} < v < vg^*_{max}$ **then**
  if $v < v_c$ **then**
    $Psaturated \leftarrow getEos(v)$
    $IEsaturated \leftarrow getIE(liquidconst, Psaturated)$
  else if $v > v_c$ **then**
    $Psaturated \leftarrow getEos(v)$
    $IEsaturated \leftarrow getIE(vapourconst, Psaturated)$
  end if
▷ The above is to compute the maximum specific internal energy which still falls within the saturation dome for v.

  if $IEreal <= IEsaturated$ **then**
    $Pressure \leftarrow bisectionsearch(IEreal, massfraction, P_{max}, P_{min})$
  else if $IEreal > IEsaturated$ **then**
    $Pressure \leftarrow getPressure(v, energy, liquidconst, vapourconst)$
  end if
▷ The above is valid as specific internal energy increases linearly with pressure at constant v within the saturation dome.

else
  $Pressure \leftarrow getPressure(v, energy, liquidconst, vapourconst)$
end if